The Vela Supercluster - does it provide the missing link to explain the local flow fields?

Ahmed Elagali

August 2015

A project submitted in partial fulfilment of the requirements for the degree M.Sc. in the Department of Astronomy, as part of the National Astrophysics and Space Science Programme
UNIVERSITY OF CAPE TOWN

Supervisors: Prof. R.C. Kraan-Korteweg and Dr. M.E. Cluver

Abstract

As part of a larger effort to uncover the structures hidden behind the Milky Way, we analyse 5,190 spectroscopic redshifts for galaxies in the Hydra/Antlia and Vela regions ($245^\circ \leq l \leq 295^\circ, |b| \leq 10^\circ$). These galaxies are based on deep optical galaxy source catalogues in the Zone of Avoidance in the Hydra/Antlia region (Kraan-Korteweg 2000a), the Vela region (von Maltitz 2012), and the near infrared 2MASS Extended Source Catalogue(XSC) (Jarrett et al. 2000a, Skrutskie et al. 2006). The observed redshifts were mainly obtained from the 2dF+AAOmega spectrograph at the Anglo-Australian Telescope (80% of the redshifts); the remaining data are from other telescopes as well as from the literature. This analysis is suggestive of the existence of a massive supercluster in this region, hereafter called the Vela Supercluster (VSC). The prospective VSC is at a mean redshift of $cz \sim 18,000\,\mathrm{km\ s^{-1}}$, and extends approximately about $87 \times 87\,\mathrm{Mpc}$ on-sky. We use a nearest neighbour algorithm to identify the galaxy clusters and groups within the potential VSC, determine their velocity dispersions and the corresponding virial masses. Although the VSC is sparsely sampled, we find 13 galaxy clusters and 22 galaxy groups contained within it. The richness and the masses of these galaxy clusters/groups are comparable with the galaxy clusters/groups found within the Shapley Supercluster by Proust et al. (2006). Taking account of the sparse sampling, the VSC seems comparable to the Shapley Supercluster (SSC). Given the fact that the SSC contributes about 9% of the Local Group motion (Muñoz & Loeb 2008), if not more see (Kocevski & Ebeling 2006). The proximity of a further supercluster (VSC) in its vicinity, might have serious implications on the bulk flows studies. Consequently, the existence of this supercluster is likely key in resolving the long-enduring bulk flow controversies and the misalignment of flows with the dipole determined via the Cosmic Microwave Background (CMB) observations.

Dedication

I would like to dedicate the work in this thesis to my mother and my siblings.

Acknowledgements

First and foremost I offer my sincerest gratitude to my supervisors Prof. R.C. Kraan-Korteweg and Dr. M.E. Cluver for their support, careful guidance, considered advices, and for their very insightful comments on my thesis. Renee & Michelle **Thanks** for being such wonderful supervisors, I am truly grateful for you both. One simply could not wish for a better or friendlier supervisors.

I would like to thank Prof. Thomas H. Jarrett for giving me access to his software and for providing me with the WISE data. Many Thanks to Dr. Maciej Bilicki for deriving the photometric redshifts for the galaxies in our source catalogues, and to Dr. Christina Magoulas who was so supportive, and helpful. Thank you Christina for answering my many questions on the peculiar velocities and the bulk flows. A special thanks to my colleague Khaled Said for being very awesome friend and for teaching me how to use the IRSF telescope.

Many thanks to my friends and colleagues at UCT Department of Astronomy for the warm and friendly environment. Last but not least, a special thanks to my mother and my siblings for supporting me throughout all my studies at the University. Mother thank you for being such a great mother and for your continuous encouragement through Skype, without you I wouldn't make it so far!

This work is financially supported by the National Astrophysics and Space Science Programme (NASSP) and the National Research Foundation (NRF). This dissertation makes use of data from the Two Micron All Sky Survey (2MASS). The 2MASS is a joint project between the University of Massachusetts and the Infrared Processing and Analysis Center/California Institute of Technology. The 2MASS is funded by the National Aeronautics and Space Administration and the National Science Foundation.

Plagiarism Declaration

I, Ahmed Elagali, know the meaning of plagiarism and declare that all of the work in the document, save for that which is properly acknowledged, is my own.

Contents

List of Figures

List of Tables

Chapter 1

Introduction

One of the major foundations of the current cosmological paradigm is the Copernican Principle. This principle, simply, states that the Earth is not at a central, or at a special location in the Universe (Bondi 1962). On cosmological scales this principle is generalized to state the isotropy and the homogeneity of our Universe on large scales. A long-standing question that follows from this principle is the source of the apparent motion of the Local Group of galaxies (LG) relative to the Cosmic Microwave Background (CMB) with $v_{LG} = 627 \pm 22\,\mathrm{km\ s^{-1}}$ (Kogut et al. 1993). The gravitational instability paradigm links this motion to the gravitation force induced by large-scale structures in the local Universe (Scoccimarro et al. 2001, Verde et al. 2002, Lin et al. 1996). For a given galaxy, the deviation in velocity from the smooth Hubble flow is known as the peculiar velocity of that galaxy. At low redshifts, the peculiar velocity is interpreted as the difference between the recessional velocity due to the Hubble Flow, cz, and the distance, d, estimated using a redshift-independent distance indicator,

$$v_p = cz - H_0 d. \tag{1.1}$$

In the case of linear perturbations, i.e. small density fluctuations compared to the mean density of the Universe, the gravitational instability theory relates the peculiar velocity field of a galaxy $\mathbf{v}$ at distance $\mathbf{r}$ to the density field as,

$$\mathbf{v}(\mathbf{r}) = \frac{\Omega_m^{0.55}}{4\pi} \int d^3\mathbf{r}' \delta_m(\mathbf{r}') \frac{\mathbf{r}' - \mathbf{r}}{|\mathbf{r}' - \mathbf{r}|^3}, \tag{1.2}$$

where $\delta_m(\mathbf{r}) = \frac{\rho(\mathbf{r}) - \overline{\rho}}{\overline{\rho}}$ is the density contrast, $\overline{\rho}$ is the average density of the Universe, and Ω_m is the matter density parameter (Peebles 1993). This equation implies that the peculiar velocity of a galaxy is generated by the matter distribution on different scales, from the local neighbourhood of the galaxy (5 Mpc) to very large scales ($\gtrsim 100\,\mathrm{Mpc}$) (Watkins et al. 2009). Consequently, the peculiar velocities are direct tracers of the underlying mass distribution in the Universe.

The peculiar velocity of whole volumes is studied using samples of peculiar velocity tracers such as galaxies, clusters, and type Ia supernovae (Rubin et al. 1976, Melnick & Moles 1987, Dressler 1984, Faber et al. 1988, Aaronson et al. 1989, Pellegrini & da Costa 1990, Mould et al. 1991, Mathewson et al. 1992, Baffa et al. 1993, Lauer & Postman 1994a, Giovanelli et al. 1996, Hudson et al. 1997, Giovanelli et al. 1998, Hudson 1999, Dale et al. 1999, Haugbølle et al. 2007, Springob et al. 2007, Feindt et al. 2013, Springob et al. 2014). One very important determination of the peculiar velocity field is the bulk flow, which in a perfectly observed data set reflects the CMB dipole. The importance of the bulk flow comes from its relation to the amplitude fluctuations on large-scale structures and its use in testing the cosmological models (Clutton-Brock & Peebles 1981, Vittorio et al. 1986, Strauss et al. 1995). Studies of the peculiar velocities and bulk flows find inconsistent results and not all concur with the current cosmological paradigm, ΛCDM. For instance, bulk flows are found for very large scales $\sim 100\,\mathrm{Mpc}$ by Scaramella et al. (1989), Lauer & Postman (1994b), Hudson et al. (1999), Willick (1999), Watkins et al. (2009), Feldman et al. (2010), Lavaux et al. (2013), Macaulay et al. (2012), Watkins & Feldman (2015). Others do find coincidence between the bulk flow measured and that expected from the ΛCDM (Branchini et al. 1996, Müller et al. 1998, Courteau et al. 2000, Colless et al. 2001b, Nusser et al. 2011, Turnbull et al. 2012, Rathaus et al. 2013, Ma & Scott 2013).

In 1994, Lauer & Postman (1994b) studied the Abell clusters (Abell 1958, Abell et al. 1989) on scales larger than 100 Mpc and claimed that the cluster frame contained within a volume of $\sim 150\,\mathrm{Mpc}$ is moving with velocity $689 \pm 178\,\mathrm{km\ s^{-1}}$ toward $l = 343°, b = 52°$. On the contrary, Lynden-Bell et al. (1988) studied the bulk flow of 400 elliptical galaxies and claimed that these nearer galaxies are infalling toward a Great Attractor (GA) at about 43 Mpc in the direction $l = 307°, b = 9°$. Two decades later, Kocevski & Ebeling (2006) analysed the dipole anisotropy in a large compiled X-ray cluster sample, consisting of the REFLEX catalogue in the southern hemisphere, the eBCS sample in the north, and the CIZA survey in the Galactic plane. They found that the contribution of the GA is only 44% of the LG motion, and that the more distant Shapley Supercluster ($\sim 200\,\mathrm{Mpc}$) contributes 30%. Other bulk flow studies indicate that there are structures hidden by the dust of the Milky Way and their contribution to the LG motion is unaccounted for (Hudson et al. 2004, Watkins et al. 2009, Turnbull et al. 2012). For instance, Watkins et al. (2009) combined data from 9 different surveys. Their data includes the *SFI++* survey (Springob et al. 2007), the *EFAR* survey (Colless et al. 2001a), the *SBF* survey (Tonry et al. 2001), the *SC* survey (Giovanelli et al. 1998), the *ENEAR* survey (da Costa et al. 2000), the *SMAC* survey (Hudson 1999), the *LP* survey (Postman & Lauer 1995), the Clusters survey (Willick 1999) as well as SNIa data from (Tonry et al. 2003). Watkins & collaborators found that the bulk flow within a Gaussian window of radius 50 Mpc is $407 \pm 81\,\mathrm{km\ s^{-1}}$ toward $l = 287° \pm 9°$, $b = 8° \pm 6°$. These results suggest that there might be further unrecognised mass overdensities hidden at low Galactic latitudes.

The purpose of this thesis is to study an excess of galaxies discovered in the Zone of Avoidance (ZoA) in the Hydra/Antlia and Vela regions ($245° \lesssim l \lesssim 295°, |b| \lesssim 10°$) at $cz \sim 18,000\,\mathrm{km\ s^{-1}}$. This overdensity seems to extend over a large area of the sky, straddling the Galactic Plane. It might well be a further supercluster in the nearby Universe. Considering the location and the distance of this overdensity, it might also provide the missing evidence for the residual bulk flow results. To visualize its location on the sky, we present Fig. 1.1. This figure is an Aitoff projection of galaxies within $0.055 < z < 0.070$ based on the 2MASS Photometric Redshift catalogue (courtesy T Jarrett). Three superclusters are marked as well as the location of the Hydra/Antlia and Vela prospective overdensity in this figure. The Shapley Supercluster (SSC) which is the nearest supercluster to the LG (Proust et al. 2006), the Horologium Supercluster (HSC) (Fleenor et al. 2005), and the Corona Borealis Supercluster (Pearson et al. 2014). If it is confirmed that this potential overdensity forms a further supercluster, it will have significant implications on the LG motion and the bulk flow studies. Especially, if we put into perspective the close proximity of this structure to the SSC. The latter is considered one of the major contributors to the bulk flow motion, and the recent residual bulk flow measurements (Springob et al. 2014, Tully et al. 2014).

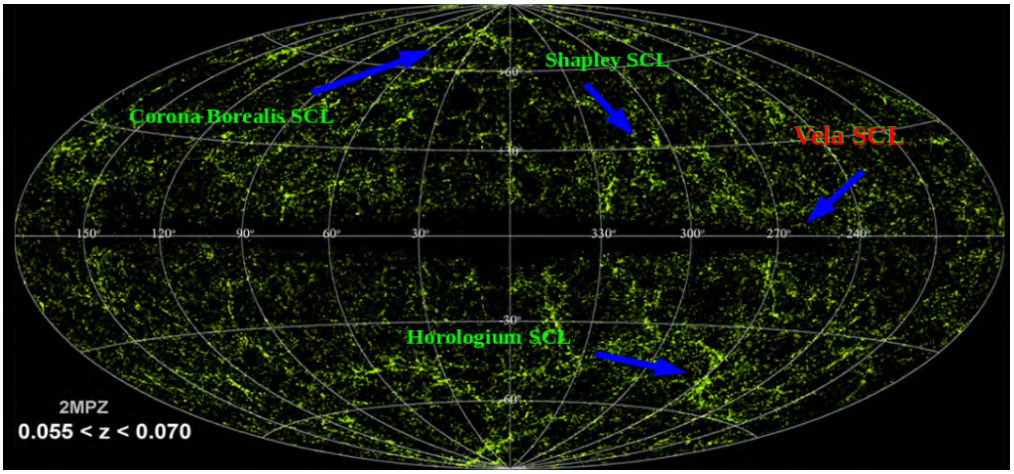

Figure 1.1: Aitoff projection for galaxies within $0.055 < z < 0.070$ in the 2MASS Photometric Redshift catalogue (Jarrett priv. comm.). The main three superclusters in this shell are marked, including the location of the new potential Vela Supercluster.

The first indication for this overdensity was deduced from 6dF Galaxy Survey observations of galaxies detected in a deep optical galaxy survey by Kraan-Korteweg (2000a). Two adjacent 6dF fields in the Vela region were observed, covering the region ($l \simeq 265° - 275°, b \simeq 5° - 10°$). The velocity histogram for the observed galaxies, a total of 373 galaxies, is shown in Fig. 1.2. There is a prominent peak at $cz \sim 18,000\,\mathrm{km\ s^{-1}}$ in the galaxy velocity distribution, in contrast to the expectations for a homogeneous velocity distribution (red curve), this is the sign for the excess galaxy density in that area. The red curve in the Fig. 1.2

is the galaxy velocity distribution of the same regions derived by using the citetJones2009 empirical function for the 6dFGS and adjusted to the total number of galaxies detected in the two ZoA fields, while the green curve is the the galaxy velocity distribution using the previous function for the same region but excluding the overdensity; figure from von Maltitz (2012). This becomes very explicit when we put into consideration the extent of the two observed fields. At the redshift of the peak ($cz \sim 18,000\,\mathrm{km\ s^{-1}}$), the twelve degrees translates to 50 Mpc, assuming a value of $H_0 = 75\,\mathrm{km\ s^{-1}\ Mpc^{-1}}$. Finding such a salient peak within this huge area is a strong evidence for the existence of an overdensity.

In 2014, the Hydra/Antlia and Vela region was then observed in great detail using the 2dF+AAOmega Spectrograph on the Anglo Australian Telescope, Australia. Six nights of observations were allocated and 25 fields were observed in that region. Unlike the 6dF observations the 25 observed fields were disseminated over a large area ($295° > l > 245°, |b| \lesssim 10°$) because the true extent of this overdensity was unknown. Observations were also made with the Southern African Large Telescope (SALT) for some of the highest galaxy density peaks in this survey area. Other redshift data for this region are the result of earlier unpublished and complementary work by Kraan-Korteweg and collaborators. These are from the Optopus multiobject spectrograph facility on the ESO 3.6 m telescope at La silla, and the South African Astronomical Observatory (SAAO) using the 1.9m telescope by Kosma von Maltitz (von Maltitz 2012). The combined data set, including data from the extragalactic database HYPERLEDA*, is being used for a detailed analysis of this massive overdensity in the Vela and Hydra/Antlia region.

Thesis Structure:
This thesis is structured as follows: In the remainder of this chapter, I present an overview of the ZoA and the multi-wavelength galaxy searches conducted to unveil galaxy structures hidden by the Milky Way. A very short summary of the properties of superclusters, with an emphasis on the SSC is also presented. Chapter 2 describes the merged optical and near-infrared ZoA catalogues that lie at the basis of the 2dF+AAOmega spectroscopic follow-up observing runs as well as the different sources of galaxy redshifts data available in our survey area. In Chapter 3, I discuss the velocity distribution of the galaxies in the direction of the proposed Vela overdensity and the large-scale structures of this overdensity in velocity wedge diagrams. The methods used to identify the galaxy clusters/groups in the direction of Hydra/Antlia and Vela overdensity is shown in Chapter 4. The velocity distribution of the galaxies in the direction of the Vela overdensity as well as the many number of galaxy clusters/groups found within this overdensity suggest that this overdensity is likely a supercluster. We call this overdensity the Vela Supercluster (VSC). Further, chapter 5 presents a comparison between the SSC and the prospective VSC using both the available spectroscopic redshifts and photometric redshifts estimated using the Artificial Neural Network (ANN_z) method. Chapter 6 summarizes the follow up observations for 11 potential galaxy clusters

*leda.univ-lyon1.fr/

found within the proposed VSC using the Infrared Survey Facility (IRSF) telescope at the SAAO. This chapter also describes deeper galaxy search results using the Wide-field Infrared Survey Explorer (WISE) for three clusters found within the VSC. Chapter 7 summarizes the results and conclusions inferred in this dissertation. Where necessary in this thesis, we assume a flat cold dark matter (ΛCDM) model with $(\Omega_0, \Omega_b, \sigma_8) = (0.27, 0.046, 0.8)$ and $H_0 = 75\,\mathrm{km\ s^{-1}\ Mpc^{-1}}$.

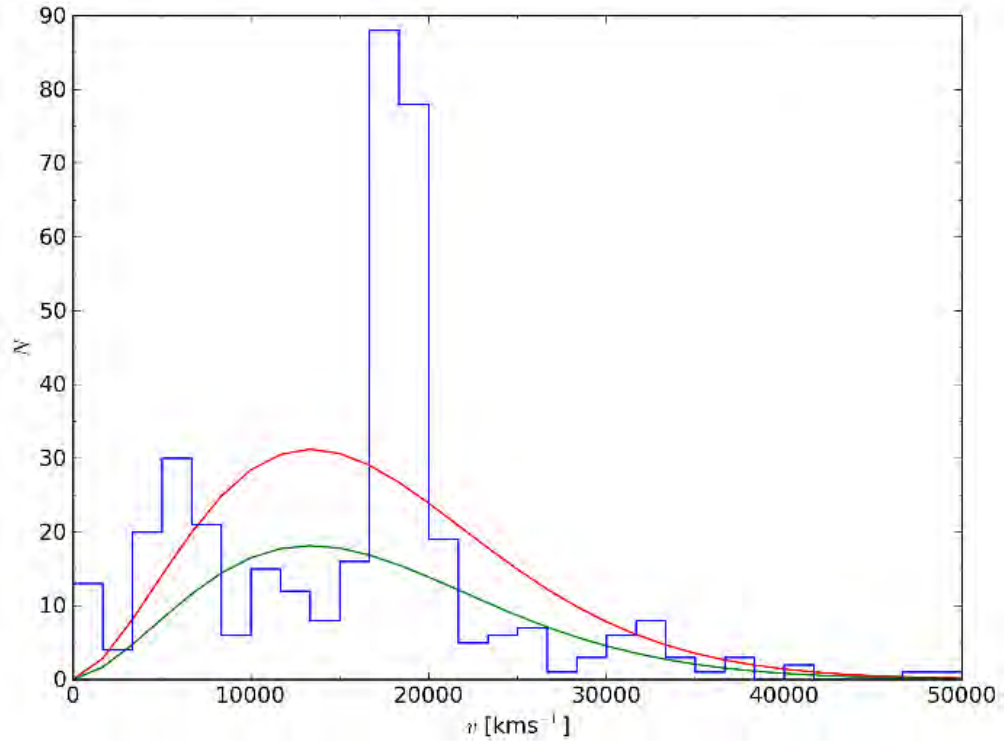

Figure 1.2: The velocity histogram of ZoA galaxies in 2 contiguous 6dF Vela fields. The red curve is the expected galaxy velocity distribution for the 6dF fields from Jones et al. (2009) empirical function for the 6dFGS, the green curve is the the galaxy velocity distribution for the same region but excluding the overdensity. This figure is adopted from von Maltitz (2012).

1.1 The Zone of Avoidance

Proctor (1887) was the first astronomer to recognize the presence of the ZoA. He deduced this fact from mapping the nebulae in Sir John Herschel's Catalogue (Herschel 1864). Proctor noted that fewer nebulae lie at low Galactic latitudes and dubbed that parts of the sky "The Zone of Few Nebulae". Subsequent to this, Charlier (1922) used a more inclusive catalogue by Dreyer (1888) and consolidated Proctor findings. During that era, there was no explanation for the lack of nebulae at low Galactic latitudes ($|b| \lesssim 10°$), the so called ZoA.

The recognition that the ZoA is caused by dust in the Milky Way was established in the 1930s. Hubble (1929) concluded that most of the Nebulae were extragalactic objects, and Trumpler (1930) discovered that the dust of the Milky Way obscures starlight. Shapley (1961) referred to the ZoA as the region with "isopleth of five galaxies or less per square degree from the Lick and Harvard surveys", in comparison to regions unobscured by the dust of the Milky Way, which have on average 54 galaxies or more per square degree (Shane & Wirtanen 1967).

The lack of galaxy detection at low Galactic latitudes is not only due to obscuration of light by the Milky Way dust but also due to the increment of the star density around the Galactic Bulge and the Galactic plane. The next subsections present a brief description about the Galactic extinction, stellar density, and how both hamper the detection of galaxies at different wavelength.

1.1.1 Galactic Extinction

Galactic dust extinction, or Galactic extinction, refers to the obscuration of light from light emitting sources by the dust of the Milky Way. The extinction occurs because dust either absorbs the incoming light and re-emits it at a different longer wavelength or scatters it in a different direction. These two processes are wavelength dependent: shorter wavelength is more affected than longer wavelength. Consequently, the optical wavelength is more affected by the dust than the infrared and radio wavelengths are. For instance, the extinction of the near infrared wavelengths in the JHK_s band compared to the optical B-band are $21\%, 13\%$, and 9%, respectively (Cardelli et al. 1989).

Cardelli et al. (1989) derived an average extinction law for the optical and the near infrared wavelengths that is applicable in the diffuse and the dense regions of the interstellar medium,

$$R_V = \frac{A(V)}{E(B-V)}, \tag{1.3}$$

where R_V is a parameter that varies from 2.6 to 5.5 according to different mediums, with a mean of ~ 3.1 in the diffuse ISM. Further, the extinction values in the optical B-band and the near infrared JHK_s bands are given by

$$A_B = 4.107\ E(B-V), \tag{1.4a}$$
$$A_J = 0.863\ E(B-V), \tag{1.4b}$$
$$A_H = 0.570\ E(B-V), \tag{1.4c}$$
$$A_{K_S} = 0.368\ E(B-V). \tag{1.4d}$$

1.1.2 Stellar Density

The increment in star density around the Galactic Bulge and Galactic plane also affects the detection of the galaxies. The stellar population increases the background noise which complicates the detection of fainter galaxies. Even more, stellar density poses difficulties in galaxy photometry, especially when fainter foreground stars are superimposed on the galaxy image (Jarrett et al. 2000a).

Figure 1.3 shows the stellar density metric taken from the 2MASS Extended Source Catalogue (Jarrett et al. 2000a)*. A logarithmic scale $\log(N_{(K_s<14^m.0)} deg^{-2})$ is used to represent this map, where N_{K_s} is the number of stars brighter than $14^m.0$ in the K_s-band. Table 1.1 explains the grey shades associated with different stellar densities shown in Fig. 1.3. As mentioned previously, the Galactic Bulge and Galactic Equator (coded white, black, dark gray) are the regions with the highest stellar densities. As a consequence detecting galaxies in these areas is very challenging, and impossible for $\log(N_{(K_s<14^m.0)} deg^{-2}) > 4.5$.

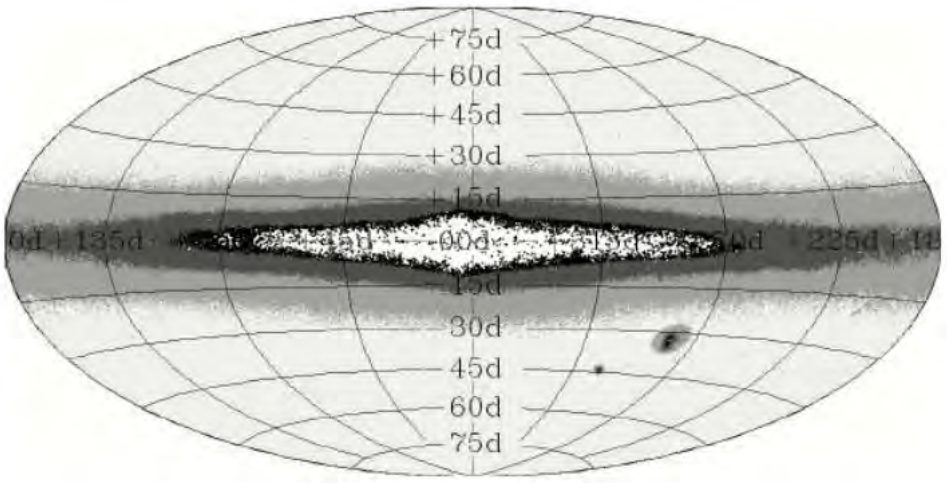

Figure 1.3: Aitoff projection of the stellar density in Galactic coordinates, as determined in the 2MASX (Jarrett et al. 2000a).

Table 1.1: The gray-scale code for different stellar densities, as in Jarrett et al. (2000a) .

$\log(N_{(K_s<14^m.0)} deg^{-2})$ range	$\lvert b\rvert$ range	colour code
$0.0 - 3.2$	$\sim 25° - 90°$	light gray
$3.2 - 3.6$	$\sim 10° - 25°$	gray
$3.6 - 4.0$	$\sim 5° - 10°$	dark gray
$4.0 - 4.5$	$\sim 0° - 5°$	black
> 4.5	$\sim 0° - 5°$	white

*http://www.ipac.caltech.edu/2mass/releases/allsky/doc/sec4_5c.html

1.2 Multi-wavelength Galaxy Searches in ZoA

Owing to the dust extinction and the increase in stellar density toward low Galactic latitudes, it is of advantage to conduct multi-wavelength surveys to search for galaxies in the ZoA. This is of importance because not all wavebands experience the same degree of hindrance by the ZoA. For instance, the near infrared wavebands are less affected by dust extinction than the optical wavebands. The next subsections give a brief description about the optical, infrared, as well as the X-ray galaxy surveys, as those are of relevance to this Master project. For a more rigorous review see Kraan-Korteweg (2000b), Kraan-Korteweg & Lahav (2000), Kraan-Korteweg (2005).

1.2.1 Optical Surveys

The first optical whole-sky catalogue was formed by compiling different optical catalogues that were homogenized and together cover the whole-sky. These are the Uppsala General Catalogue (Nilson 1973), the ESO Uppsala General Catalogue (Lauberts 1982), and the Morphological Catalogue of Galaxies (Vorontsov-Vel'Yaminov & Arkhipova 1963). The compiled catalogue is complete for galaxies larger than $D = 1.3'$ (Hudson & Lynden-Bell 1991), up to extinction levels of $A_B = 1^m.0$ which on average is loosely aligned with $|b| \lesssim 10°$(see Kraan-Korteweg & Lahav (2000) and references therein). Figure 1.4 displays the whole-sky catalogue plotted in Galactic coordinates. The red contour defines the extinction contour levels of $A_B = 1^m.0$ as determined from the Schlegel et al. (1998) dust extinction maps. The galaxies are coded according to their sizes, where the large circles are galaxies with $D \geq 3.0'$, the smaller circles are galaxies with $2.0' \leq D < 3.0'$, whereas the smallest circles are galaxies with $1.3' \leq D < 2.0'$. Fig. 1.4 is taken from Kraan-Korteweg & Lahav (2000).

Various dedicated deep optical surveys were conducted with the specific aim to reduce the ZoA. Tens of thousands of galaxies were discovered (see Kraan-Korteweg & Lahav (2000) for more details about these optical surveys). The new galaxy catalogues are complete to extinction-corrected radii of $D \geq 1.3'$ and up to extinction levels of $A_B \lesssim 3^m.0$, resulting in a reduced ZoA delimited by $|b| \lesssim 5°$ rather than $|b| \lesssim 10°$. Figure 1.5 presents the all-sky galaxy distribution from this catalogue. The red contour defines the region with extinction levels of $A_B = 3^m.0$, and the galaxy sizes are coded similarly to that in the previous figure. Figure 1.5 is taken from Kraan-Korteweg & Lahav (2000).

Given the location of the potential VSC, my thesis will make extensive use of data from the ZoA deep optical galaxy catalogue in the Hydra/Antlia survey region ($266° \lesssim l \lesssim 296°, -10° \lesssim b \lesssim 8°$); see Kraan-Korteweg (2000a), and the Vela region ($245° \lesssim l \lesssim 280°, |b| < 10°$); see von Maltitz (2012). The galaxies ($N = 3271, N = 3922$, respectively) in these two catalogues are complete to a diameter of $D \gtrsim 12''$, a B-band magnitude limit $B_J \lesssim 18^m.5$, and mostly lie at extinction levels of $A_B \lesssim 3^m.0$.

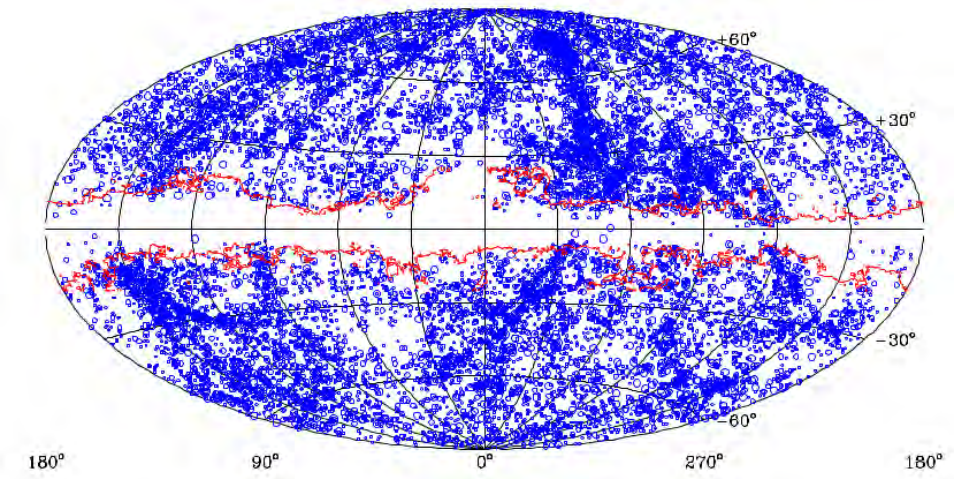

Figure 1.4: Aitoff projection of the whole-sky optical galaxy catalogue plotted in Galactic coordinates. The galaxies plotted are coded according to their sizes, where the large circles are galaxies with $D \geq 3.0'$, the smaller circles are galaxies with $2.0' \leq D < 3.0'$, and the smallest circles are galaxies with $1.3' \leq D < 2.0'$. The red contour marks extinction levels of $A_B = 1^m.0$ as determined from Schlegel et al. (1998) dust extinction map. Reproduced from Kraan-Korteweg & Lahav (2000).

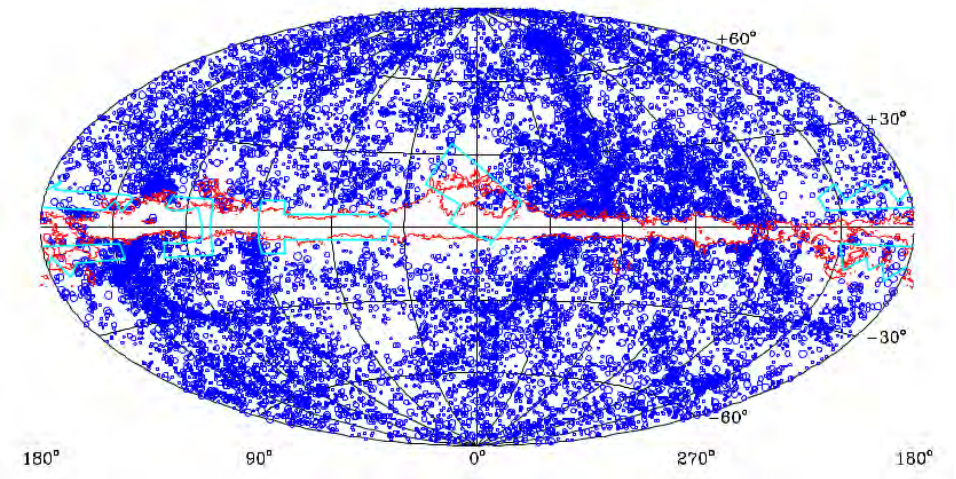

Figure 1.5: Aitoff projection of the whole-sky optical galaxy catalogue plotted in Galactic coordinates, and complete to extinction corrected radii of $D \geq 1.3'$. The diameter codes are similar to that of Fig. 1.4. The red contour marks regions with $A_B = 3^m.0$ as determined from Schlegel et al. (1998) dust extinction map, reproduced from Kraan-Korteweg & Lahav (2000).

1.2.2 Infrared Surveys

Despite the fact that the infrared wavelength is less hampered by the dust of the Milky Way, galaxies behind the Galactic Bulge are difficult to identify. Because of the high stellar population around the Galactic Bulge, which leads to a different ZoA. One of the most inclusive near-infrared surveys is the 2 Micron All Sky Survey (2MASS, Skrutskie et al. (2006)).

The 2MASS covers 99.998% of the sky in the $J(1.2\ \mu m)$, $H(1.65\ \mu m)$, and the $K_s(2.16\ \mu m)$ bands. The 2MASS observations took place between June 1997 and February 2001. A total of 471 million point sources (in the Point Source Catalogue (PSC)), and 1.6 million extended Sources (in the Extended Source Catalogue (XSC)) were identified (Jarrett et al. 2000b). Figure 1.6 shows the extended sources distribution from the 2MASS Extended Source Catalogue (XSC) and the point sources from the Point Source Catalog (PSC). The galaxies in Fig. 1.6 are colour coded according to their different photometric redshifts. Blue are galaxies with $z < 0.01$, green are galaxies in the redshift range $0.01 < z < 0.04$, and red are galaxies in the redshift range $0.04 < z < 0.1$. This figure is reproduced from Jarrett et al. (2000b). Comparing Fig. 1.6 with the all-sky deep optical survey, Fig. 1.5, it is noticeable that the 2MASS survey has a reduced ZoA, that is nearly non-existent in the Galactic anti-centre. In fact, the deep optical surveys hardly find galaxies above extinction levels of $A_B \gtrsim 3^m.0$, while the 2MASS can uncover galaxies up to extinction levels of $A_B = 10^m.0$, if the stellar density is low (Kraan-Korteweg & Jarrett 2005).

A new window to explore galaxies has recently become available through systematic mid-infrared surveys. One of the most inclusive mid-infrared surveys is the Wide-field Infrared Survey Explorer (WISE). WISE was launched in 2009 to survey the whole-sky in four mid-infrared bands: $W1$-band 3.4μm , $W2$-band 4.6μm, $W3$-band 12μm , and $W4$-band 22μm (Wright et al. 2010). Generally, the mid-infrared radiation is produced by dust surrounding massive stars. This heated dust reprocesses the radiation from the massive stars, e.g. ultra-violet radiation, and re-emits it as mid-infrared radiation. In this thesis, I will use WISE to further study areas in the Vela and the Hydra/Antlia overdensities. This will reflect on the final assessment of the entire extent and mass of this overdensity, in further studies. I will also prepare new targets for follow-up observations to obtain more redshifts and get better coverage of the velocities and the properties of the prospective clusters.

1.2.3 X-ray Surveys

The X-ray wavelength band experiences minimal dust obscuration by the ZoA. In fact, the hard X-ray emission of the order of keV is transparent to the Milky Way dust. However, the soft X-ray emission is obscured by the high column density of the Galactic hydrogen

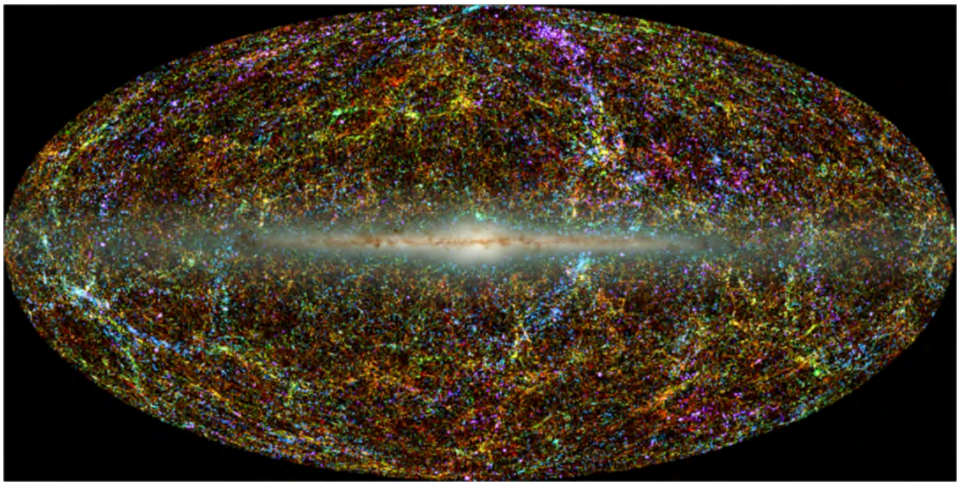

Figure 1.6: Aitoff projection of the extended sources in the 2MASS Extended Source Catalogue (XSC), and the point sources from the Point Source Catalog (PSC). The blue are galaxies with ($z < 0.01$), the green in the redshift range ($0.01 < z < 0.04$), and the red in the redshift range ($0.04 < z < 0.1$). Reproduced from Jarrett et al. (2000b).

gas at low Galactic latitudes. Since massive clusters are strong X-ray sources, X-ray observations are efficient in terms of identifying galaxy clusters in the ZoA. Moreover, the X-ray luminosity of a cluster is correlated with its mass $L_X \propto M^2$, where M is the mass of the cluster (Kraan-Korteweg & Lahav 2000), which is of relevance to the mapping of the mass overdensities in the local Universe.

Many all-sky X-ray surveys were conducted such as Uhuru, Ariel V, HEAO-1 as well as ROSAT, but the first systematic effort to identify galaxy clusters in ZoA was the "Clusters In the ZoA " (CIZA) survey (Ebeling et al. 2005, Kocevski et al. 2007). The CIZA survey used X-ray data from ROSAT All-Sky Survey (RASS), and resulted in more than 250 galaxy clusters. Fig. 1.7, reproduced from Kocevski et al. (2007), shows the X-ray clusters identified by the CIZA survey. The circles are clusters identified by Ebeling et al. (2005), whereas stars are the clusters identified by Kocevski et al. (2007). The clusters plotted in Figure 1.7 are not the complete sample identified by the CIZA survey, these clusters are the brightest ones (130 clusters) with fluxes higher than 3×10^{-12} ergs cm^{-2} s^{-1}.

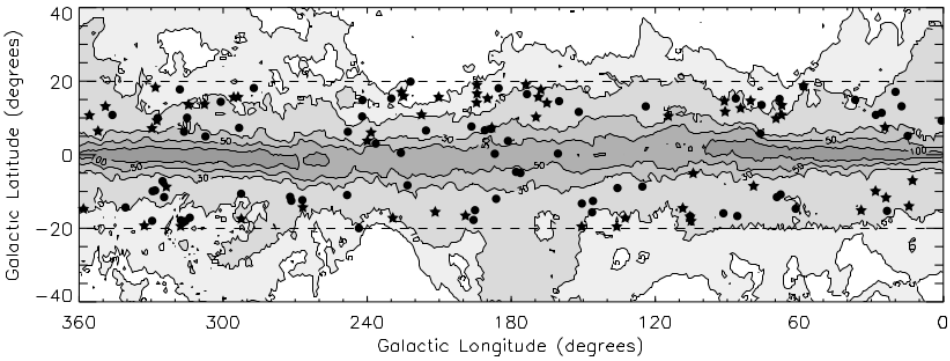

Figure 1.7: CIZA X-ray clusters, the circles are clusters identified by Ebeling et al. (2005), whereas stars are the clusters identified by Kocevski et al. (2007). These clusters have fluxes higher than 3×10^{-12} ergs cm^{-2} s^{-1}. Reproduced from Kocevski et al. (2007).

1.3 Superclusters

In this section, I will give a brief review on superclusters, in general, and highlight the case of the Shapley Supercluster (SSC) as one of the most thoroughly investigated nearby superclusters. The main purpose is to compare the properties of the prospective VSC candidate with those of the SSC, in terms of velocity distribution, velocity wedges, extent, number of clusters, and their masses (see chapter 4).

Superclusters are the largest, most massive and extended extragalactic systems in the Universe. These structures can extend over $\sim 30 - 100\,$Mpc, and have masses of a few $10^{16}\,M_{\odot}$. In general, superclusters tend to surround regions of comparable size and very low density called "voids" (Batiste & Batuski 2013a). In most cases they are connected through filaments and sheets of galaxies (Einasto et al. 1980). Studying the dynamics of these structures can provide us with an enhanced picture for structure formation theories (Araya-Melo et al. 2009, Sheth & Diaferio 2011) as well as the distribution of dark matter in the Universe (Cen 1994, Quintana et al. 1995).

During the past few decades, large-scale surveys have revealed relatively nearby superclusters. One of the best studied superclusters in the local Universe is the SSC. The SSC was first noted by Shapley (1930), it has been explored spectroscopically by Proust et al. (2006), later in X-ray by Mitsuishi et al. (2012), followed by multi-wavelength imaging by Merluzzi et al. (2015). This structure is centred at approximately (RA, Dec)=($13^{\rm h}\ 25^{\rm m}$,$-30°$), (l,b)= $(312°, 31°)$. At redshift of $z \sim 0.05$, it extends over an area of $12° \times 30°$ and contains 33 galaxy clusters. The SSC occupies a spatial volume of $\sim 10^{15}$ Mpc^3, and has a mass of about $\sim 5 \times 10^{16}\,M_{\odot}$ (de Filippis et al. 2005, Muñoz & Loeb 2008). In comparison with the SSC, the Horologium-Reticulum Supercluster (HRSC) is considered as the second most massive supercluster within 300 Mpc (Lucey et al. 1983, Zucca et al. 1993, Einasto

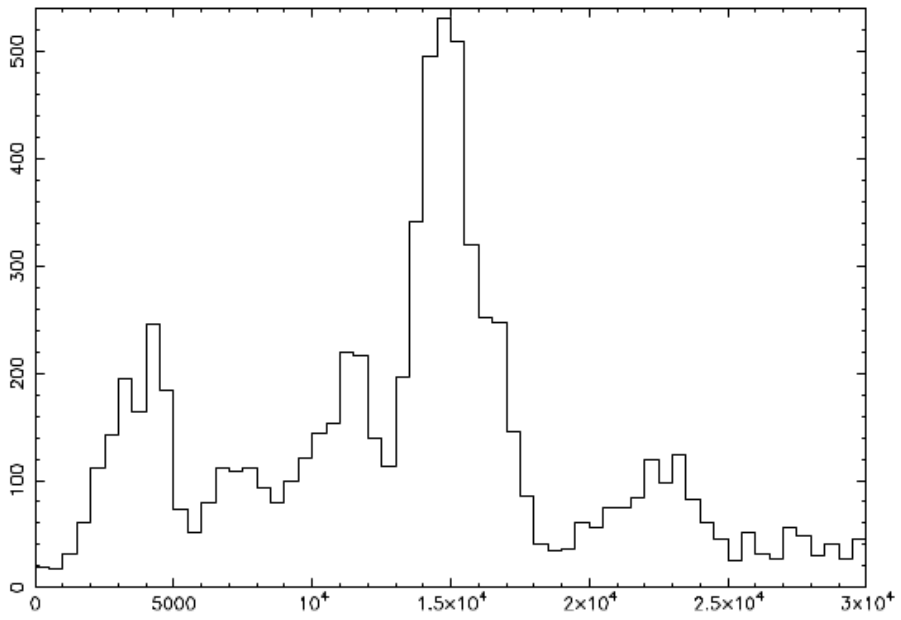

Figure 1.8: The velocity distribution of the galaxies in the direction of SSC, reproduced from Proust et al. (2006).

et al. 2001, Fleenor et al. 2006). The HRSC is centred at approximately (RA, Dec)= ($3^{\rm h}$ $19^{\rm m}$,$-50°$), (l,b)= ($261°, -53°$). At mean redshift $z \sim 0.066$, it extends over an area of $12° \times 12°$, and contains 21 galaxy clusters (Fleenor et al. 2006). Another massive supercluster within 300 Mpc is the the Corona Borealis Supercluster (CSC) (Batiste & Batuski 2013b, Pearson et al. 2014) . The CSC is centred at approximately (RA, Dec)= ($15^{\rm h}23^{\rm m}$, $30°$), (l,b)= ($46°, 56°$). At mean redshift $z \sim 0.07$, it extends over an area of $6° \times 6°$, contains 12 galaxy clusters, and has a mass of about $\sim 0.6 - 12 \times 10^{16}\,{\rm M}_{\odot}$ (Pearson et al. 2014). In summary, the Shapley Supercluster stands out more prominently compared to the other two massive superclusters in the nearby Universe because of its huge extent and unusual massive structures.

A thorough analysis of the SSC was conducted by Proust et al. (2006). They compiled redshift data from different surveys, namely, Las Campanas observatory (Quintana et al. 2000), UKST at Siding Spring, Australia (Drinkwater et al. 1999), and from the ESO 3.6 m telescope at La Silla, Chile (Quintana et al. 1997). A total of 8632 galaxy redshifts are compiled in their catalogue. Fig. 1.8, reproduced from Proust et al. (2006), shows the velocity distribution of the galaxies in Proust et al. (2006) catalogue. This histogram shows the galaxy velocities in the range of $0 \leq v \leq 30000\,{\rm km\ s^{-1}}$, with a step size of $500\,{\rm km\ s^{-1}}$. There are four peaks in this histogram, each indicating an excess density. The first peak at $4000\,{\rm km\ s^{-1}}$ corresponds to the Centaurus foreground Wall (Willmer et al. 1995), and the Norma Wall (Kraan-Korteweg et al. 1996, Woudt et al. 2008). The second peak, which extends from $9000 - 13000\,{\rm km\ s^{-1}}$, translates to what is dubbed the "Front-Eastern Wall".

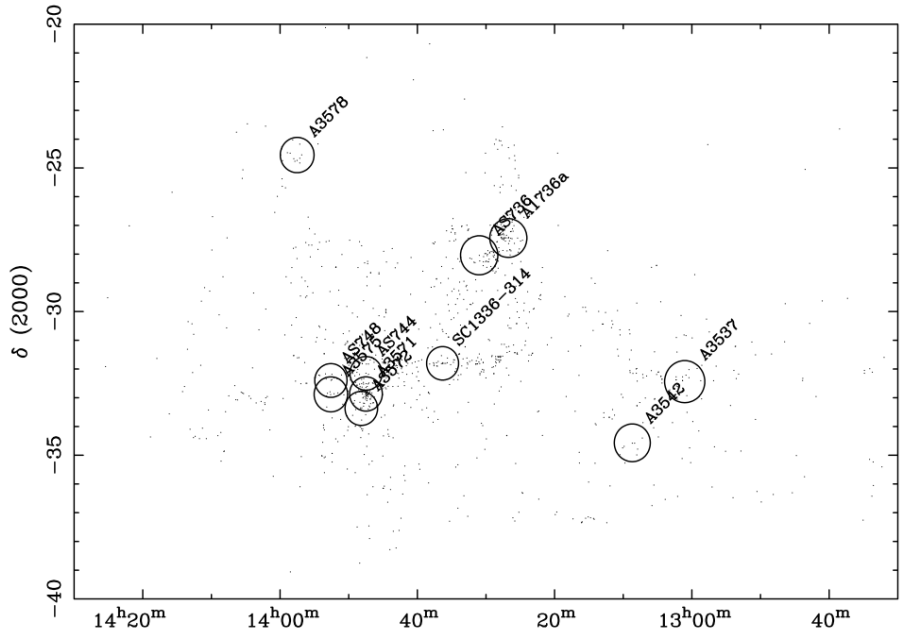

Figure 1.9: On-sky positions of the "Front Eastern Wall" clusters located within 9000 − 13000 km s^{-1}, adopted from Proust et al. (2006).

This wall encloses up to 7 clusters and one massive galaxy group, with masses in the range $2.1 \times 10^{14} - 2.3 \times 10^{15}\,M_{\odot}$ (Quintana et al. 2000). The on-sky distribution of these clusters is presented in Fig. 1.9, adopted from Proust et al. (2006).

The third peak at 15000 km s^{-1}, associated with a relatively broad buttresses extending from 13000 − 18000 km s^{-1}, is the SSC prime concentration. This concentration contains 33 clusters, with masses in the range $8.3 \times 10^{14} - 3.3 \times 10^{15}\,M_{\odot}$. Figure 1.10, reproduced from Proust et al. (2006), shows the on-sky distribution of the galaxies in the direction of the SSC. There are 33 clusters enclosed within SSC velocity range 13000 − 18000 km s^{-1}, a comprehensive list of these clusters is presented in Proust et al. (2006). The last peak, which extends from 20000 − 25000 km s^{-1}, corresponds to 4 clusters and one galaxy group, with masses in the range $1.8 \times 10^{14} - 4.9 \times 10^{14}\,M_{\odot}$, respectively (Proust et al. 2006).

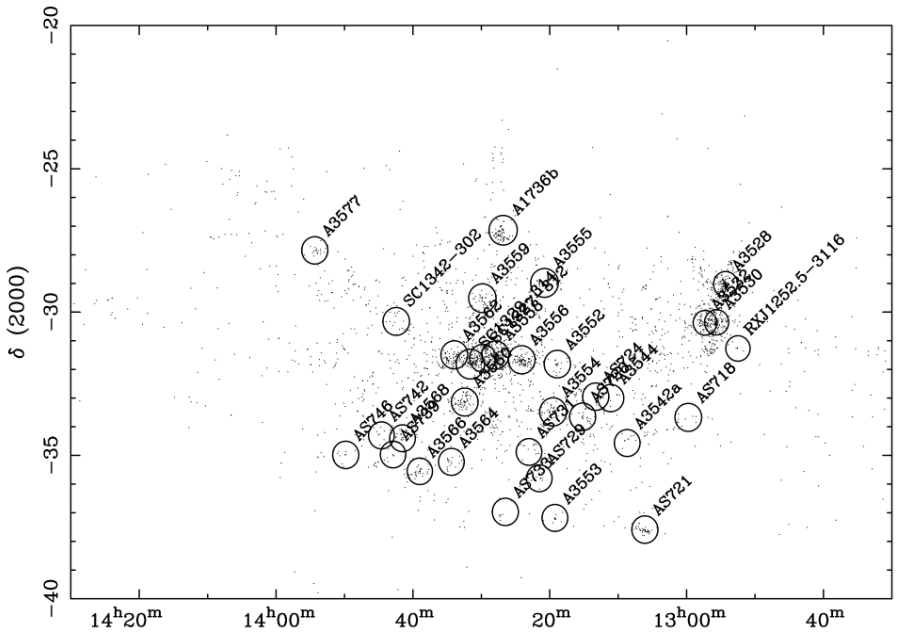

Figure 1.10: On-sky positions of the main SSC clusters located within $13000 - 18000\,\mathrm{km\ s^{-1}}$, reproduced from Proust et al. (2006).

Chapter 2

The Catalogue

This chapter describes the redshift catalogue that I assembled, dubbed the "Master Catalogue". It is based on deep optical galaxy source catalogues in the ZoA in the Hydra/Antlia and Vela regions ($245^\circ \lesssim l \lesssim 295^\circ, |b| \lesssim 10^\circ$) (Kraan-Korteweg 2000a, von Maltitz 2012), and the near infrared 2MASS Extended Source Catalogue (XSC) (Jarrett et al. 2000a, Skrutskie et al. 2006). A detailed description of this catalogue as well as the different sources of galaxy redshifts are presented in the following sections. Our main focus will be on the major new input from the 2dF+AAOmega observations. The redshifts data will be analysed and assessed for accuracy based on intercomparisons between the AAOmega observations and the other redshifts observations from the 6dF, the Optopus instrument, SALT, as well as redshift from the South African Astronomical Observatory (SAAO) using the 1.9 m telescope. The complete redshift catalogue with main galaxy parameters is presented in Appendix A.

2.1 The Master Catalogue

The Master Catalogue is a redshift catalogue that contains 5480 mostly new or unpublished redshifts in the combined Hydra/Antlia and Vela regions. The galaxies in this catalogue originate from deep optical source catalogues in the southern Milky Way in the Hydra/Antlia region (Kraan-Korteweg 2000a), and the adjacent Vela region (von Maltitz 2012), as well as from the near infrared 2MASS Extended Source Catalogue (XSC) (Jarrett et al. 2000a, Skrutskie et al. 2006). The two deep optical source catalogues form part of a series of deep optical surveys intended to reduce the extent of the southern ZoA (Woudt & Kraan-Korteweg 2000, Woudt et al. 2000, Fairall & Kraan-Korteweg 2000, von Maltitz 2012), and enhance the current understanding of the local cosmic flow fields.

The galaxies in the Hydra/Antlia region ($266^\circ \lesssim l \lesssim 296^\circ, -10^\circ \lesssim b \lesssim 8^\circ$) were identified using the IIIaJ copies of the ESO/SRC all sky survey, and a modified blinking machine (magnifying images 50 times). This diameter-limited search produced a total of 3279 galaxies with

a diameter limit $D \gtrsim 12''$, and a mean B-band magnitude limit of about $B_J \sim 18^m.5$. Only 97 galaxies were previously discovered by Lauberts (1982). This diameter limit ($D \gtrsim 12''$) is mainly imposed because it is hard to discriminate between stars and round galaxies below this limit, the refraction crosses of stars disappear below this limit (Kraan-Korteweg 2000a). Figure 2.1, reproduced from Kraan-Korteweg (2000a), shows the on-sky distribution of the galaxies in the Hydra/Antlia region, marked with the dashed line. The small dots specify the 3279 galaxies, in the Hydra/Antlia catalogue, with a diameter $D \gtrsim 12''$, whereas the larger dots are the galaxies in the (Lauberts 1982) optical catalogue, with $D \gtrsim 60''$. The extinction magnitudes $A_B = 1^m.0, 3^m.0$ and $5^m.0$ are marked with the contour lines.

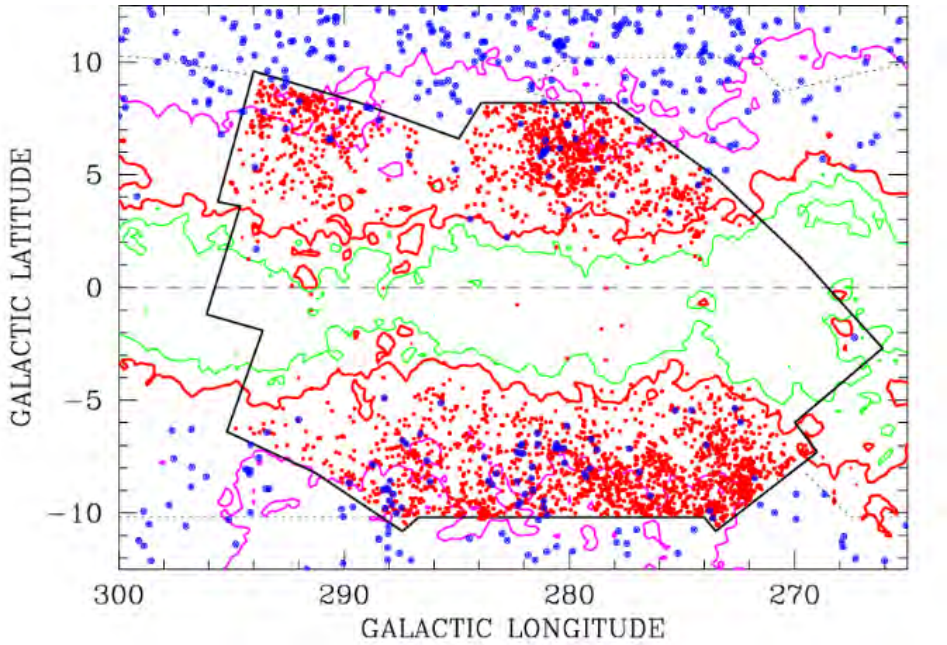

Figure 2.1: The on-sky distribution of the galaxies in the Hydra/Antlia Catalogue. The small dots specify the 3279 galaxies with a diameter $D \gtrsim 12''$, whereas the larger dots are the galaxies in Lauberts (1982) optical catalogue with $D \gtrsim 60''$. The extinction magnitudes $A_B = 1^m.0, 3^m.0$ and $5^m.0$ are marked with the contour lines as determined from Schlegel et al. (1998). From Kraan-Korteweg (2000a).

Galaxies in the Vela region ($245° \lesssim l \lesssim 280°, |b| \lesssim 10°$) were identified, also, using the ESO/SRC survey plates. A total of 4566 extended sources were found, of which 3,922 with diameter $D \gtrsim 12''$, and 388 galaxies with diameter $D < 12''$ to a mean B-band magnitude limit of $B_J \sim 18^m.4$. Galaxies with $D < 12''$ were not included in the Vela catalogue because below $12''$ it is difficult to make a distinction between the stars and the galaxies (von Maltitz 2012). Figure 2.2, adopted from von Maltitz (2012), demonstrates all the detected extended sources in the Vela catalogue. The solid line illustrates the Vela region, the blue dots are galaxies with $D \gtrsim 12''$, whereas the red dots are galaxies with $D < 12''$. The yellow contours

specify regions with extinction levels of $A_B = 1^m.0$, while the orange contours define regions with extinction levels of $A_B = 3^m.0$. For a detailed description on how the position, the diameter, the magnitude, and the morphology of the galaxies in the Vela catalogue were estimated, refer to von Maltitz (2012).

It is crucial to notice that not all the optical galaxies in the Master Catalogue have counterparts in the 2MASX catalogue and vice versa; this difference will appear when the B-band and the K_s-band magnitude counts for the overdense areas (chapter 4) are discussed. The B-band and the K_s-band magnitude counts for some dense areas will have homogeneous histogram shapes because most of the galaxies in the optical have counterparts in the infrared, whereas for other dense areas the magnitude histograms will not be homogeneous because not all the optical galaxies have counterparts in the infrared and vice versa. Moreover, the foreground dust extinction affects the optical magnitudes more severely than the near-infrared magnitudes.

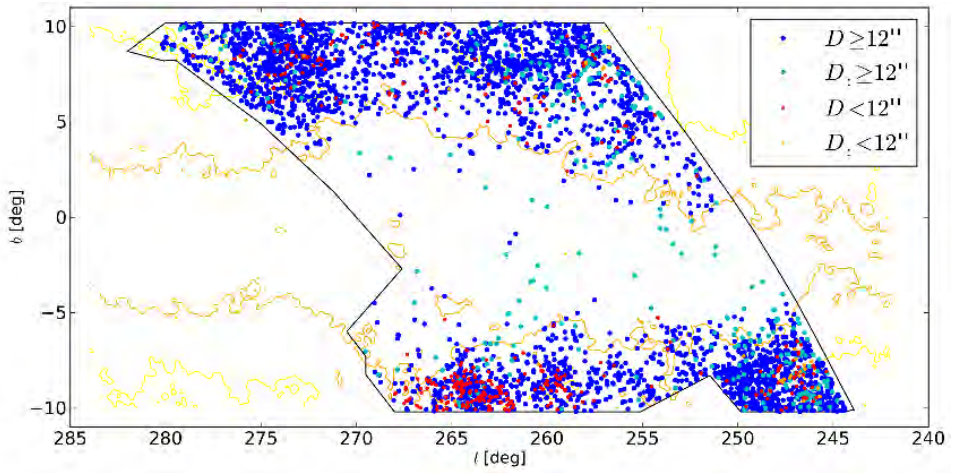

Figure 2.2: The on-sky distribution of the galaxies in the Vela Catalogue. The blue dots are galaxies with $D \gtrsim 12''$, whereas the red dots are galaxies with $D < 12''$.The yellow contours specify regions with extinction levels of $A_B = 1^m.0$, while the orange contours define regions with extinction levels of $A_B = 3^m.0$ as determined from Schlegel et al. (1998) dust extinction map. From von Maltitz (2012).

2.2 Redshift Data

In the following I describe the major redshift campaigns that were pursued in the Hydra/Antlia and Vela ZoA regions. This data is the basis of our subsequent analysis. The majority of the redshifts data in hand were observed by Kraan-Korteweg and M. Cluver using the AAOmega spectrograph on the Anglo Australian Telescope in February 2014.

Other redshift data are the result of earlier unpublished and complementary work by Kraan-Korteweg and collaborators. These are from the 6dF instrument on the Anglo-Australian Observatory's UK Schmidt Telescope, Optopus multiobject spectrograph facility on the ESO 3.6 m telescope at La silla, the Southern African Large Telescope (SALT), the South African Astronomical Observatory (SAAO) using the 1.9 m telescope. The redshift catalogue was complemented with redshifts in the literature using the extragalactic database HYPERLEDA*.

2.2.1 The AAOmega Redshift Data

The AAOmega Spectrograph is mounted on the Anglo-Australian Telescope (AAT). The AAT is a 3.9 m equatorially mounted telescope operated by the Australian Astronomical Observatory. It is located at an altitude of approximately 1100 m in Siding Spring, Australia (Smith et al. 2004, Saunders et al. 2004, Sharp et al. 2006).

Different front-ends are loadable on this spectrograph. For instance, the Two Degree Field ("2dF") multi-object system, KOALA integral field unit as well as the SAMI multi-object integral field unit. The Two Degree Field system ("2dF") is the AAT's most complex positioning astronomical instrument, and it is the instrument used for our observations. The 2dF system retrieves up to 392 concurrent spectra of objects within a two degree field on the sky (Colless et al. 2001a, Lewis et al. 2002). Moreover, the 2dF system consists of a robot gantry, which positions optical fibres to an accuracy of 0.3″ on the sky, a wide-field corrector as well as an atmospheric dispersion compensator.

The observations were conducted from the 1st to the 6th of February 2014, 4 dark nights and 2 grey nights, by Kraan-Korteweg and M. Cluver. The 580V and 385R grating sets, 570 nm dichroic beamsplitter and 570 nm blaze wavelength were used. A detailed log of the the observations is given in Appendix B. These observations yielded 4344 redshifts obtained from 25 fields in the Hydra/Antlia and Vela regions. The majority of these redshifts, 95%, are science quality redshifts, while the remaining spectra were dominated by a foreground star for which it was not possible to extract the spectrum of the targeted galaxy. A total of 2060 galaxies belong to the Vela catalogue, of which 953 galaxies are optical only and have no counterparts in the 2MASS XSC. Further, 481 galaxies belong to the Hydra/Antlia catalogue with no counterparts in the 2MASS XSC, and the remaining 1803 galaxies belong to the 2MASS XSC with no optical counterparts. Figure 2.3 shows the 25 fields of the AAOmega observing run superimposed on the galaxy distributions. Blue dots are optical galaxies, the red dots are 2MASS XSC galaxies, and the black dots are optical galaxies with counterparts in the 2MASS XSC. The AAOmega observed fields were selected below extinction levels of $A_B \geq 3$ mag and are positioned on the densest areas in the direction of

*http://leda.univ-lyon1.fr/

Vela and Hydra/Antlia regions. This can be inferred from Fig. 2.4 which shows density of galaxies in our survey regions. Figure 2.5 illustrates an example of the absorption and the emission lines of a typical galaxy spectra using the RUNZ software. The 2dFDR software, developed for the 2dFGRS at the AAO, adopts the standard tasks to extract spectra from 2D images, i.e. bias subtraction, flat-fielding, fibre trace fitting, and wavelength calibration (Hopkins et al. 2013). The redshifts of the observed objects were estimated using the fully automated AUTOZ code (Baldry et al. 2014). This code uses the cross-correlation method to measure the redshifts of the observed spectra. In the case of spectra blended with stars, RUNZ was used to confirm the galaxy redshifts where possible. RUNZ, also, adopts a cross-correlation method to measure the redshifts of the spectra. If the code fails to provide a reliable redshift measurement, it permits the observers to check the spectrum manually, before particularizing a redshift flag. These flags range from $0-4$. Flag 4 indicates a certain redshift, flag 3 implies a probably correct redshift, flag 2 specifies the need for self-reliant verification, flag 1 entails that no redshift matched, and flag 0 means that the spectrum is incorrect and a new observation is needed (Hopkins et al. 2013). Only flags 4&3 are deemed science quality.

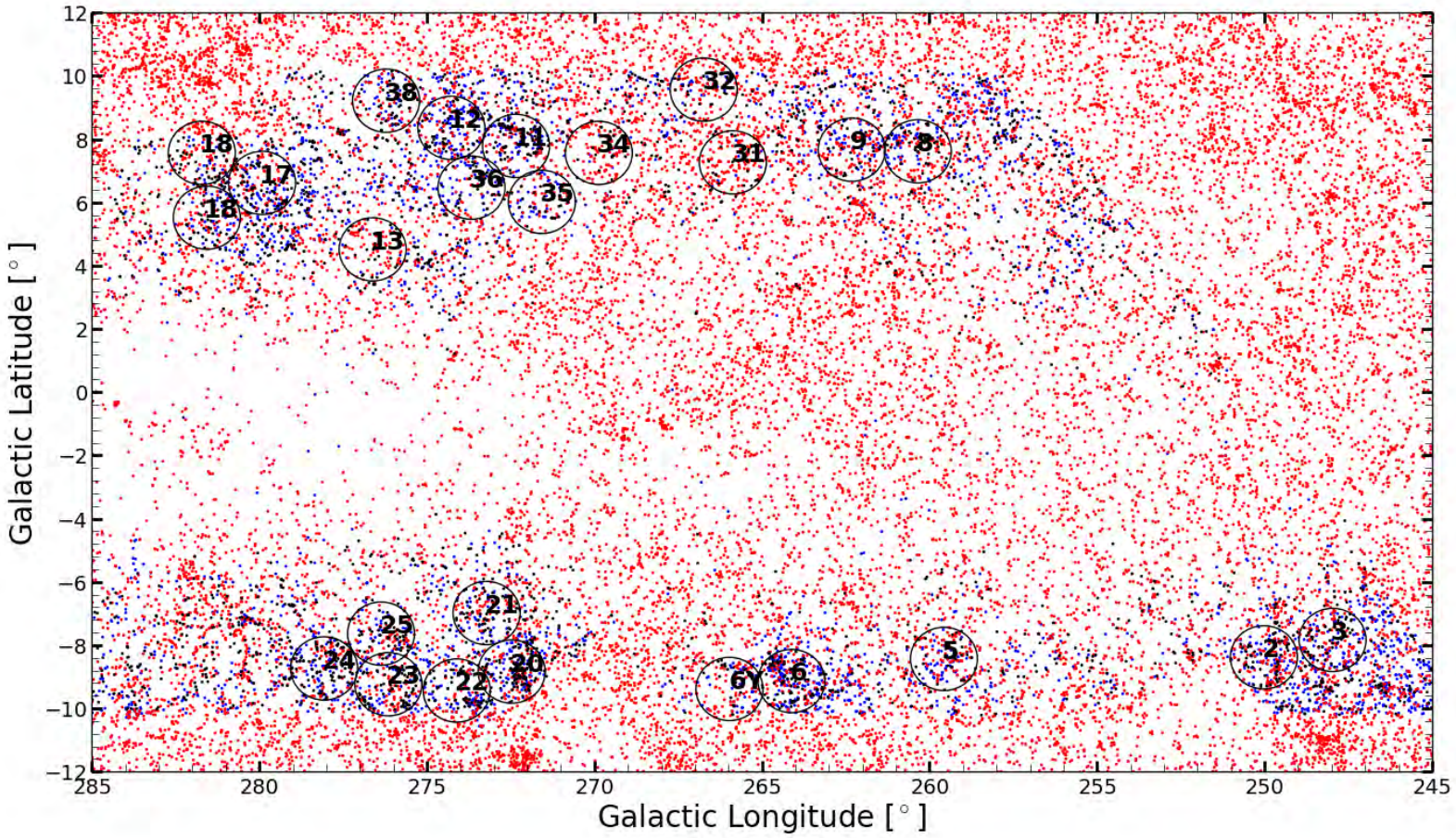

Figure 2.3: The AAOmega Observation fields. The blue dots are optical galaxies, the red dots are 2MASS XSC galaxies, and the black dots are optical galaxies with counterparts in the 2MASS XSC.

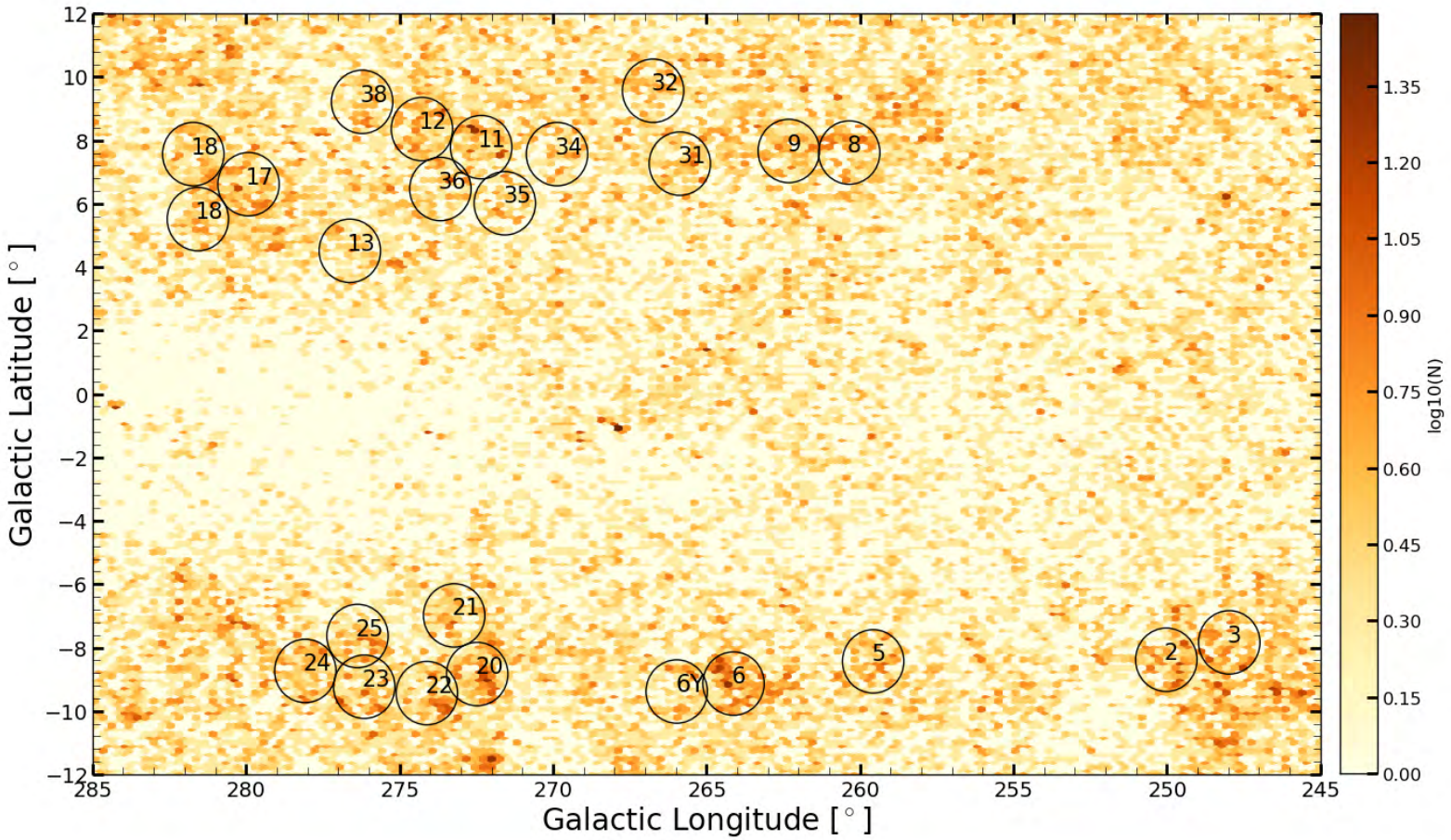

Figure 2.4: The AAOmega fields superposed on a density plot of all the galaxies in our source catalogues.

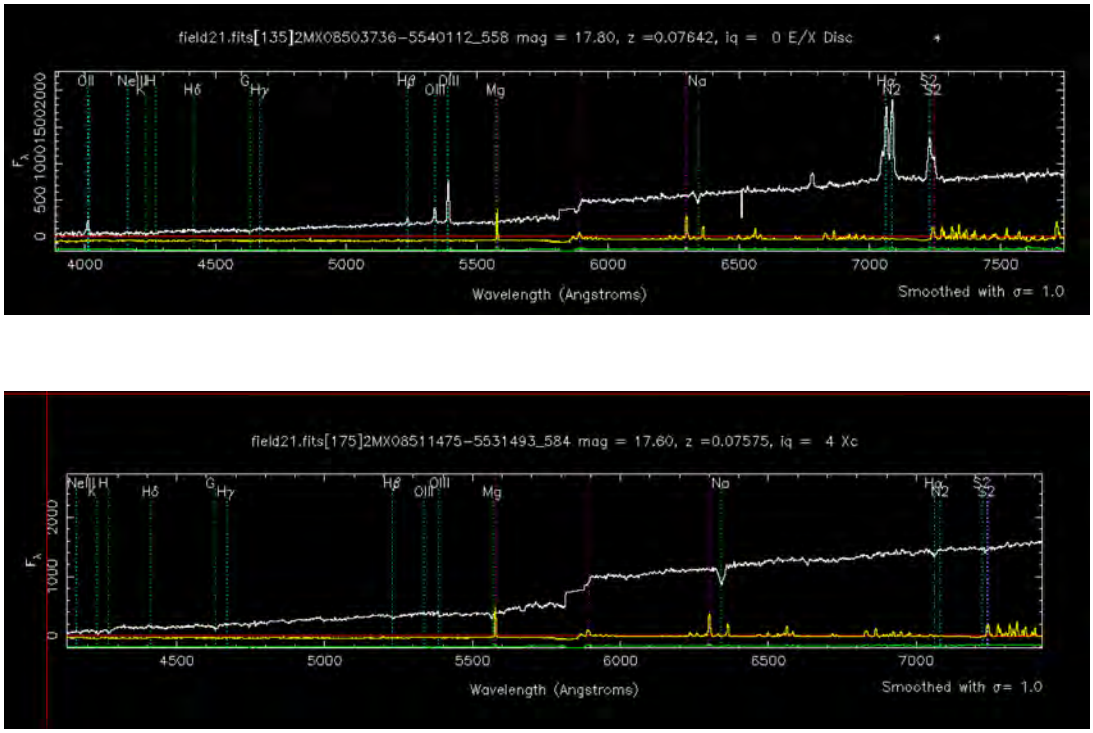

Figure 2.5: Emission and absorption lines for two different galaxy spectra, M. Cluver private commun.

Results from the AAOmega Observations:

In total 4433 redshifts were obtained in the 25 fields with the AAOmega spectrograph, of which 4126 are science quality redshifts. Table 2.1 shows some statistics with regard to the galaxies targeted with the AAOmega observations. The AAOmega fields are sorted in descending order of the number of fibred galaxies. There are nine entries in this table.

Column 1: Name of the field.

Column 2: Central Galactic coordinates of the field.

Column 3: Total number of galaxies within the field.

Column 4: Number of fibred galaxies in the field.

Column 5: The percentage of fibred galaxies in the field. The percentage of fibred galaxies (N%) is the ratio of the number of fibred galaxies to the total number of galaxies in that particular field.

Column 6: Number of star subtracted redshifts in the field.

Column 7: Number of undetected redshifts within the field. The star subtracted redshifts (star*) are spectra contaminated by stars for which the underlying galaxy spectra could be extracted and resulted in a reliable redshift unlike the "undetected redshift". In this case, it was impossible to get a redshift for the galaxies because their spectra were very contaminated or the signal to noise ratio was too low.

Column 8: Number of good redshift observations, these are the galaxy redshift measure-

ments, i.e excluding the star contaminated spectra.
Column 9: The percentage of good redshift within the field. The good redshift (%) is the percentage of the good redshift observations to the number of fibred galaxies.

For the fields $2, 3, 6, 11, 22$ and 32, the percentage of the unfibred galaxies is slightly higher. This might indicate a clustering of galaxies at these regions. Figure 2.6 displays a density plot of the galaxies in the Hydra/Antlia and Vela regions observed with the AAOmega, the fields $2, 3, 6, 11, 22$ and 32 are marked by the black circles. This figure shows that the fields $2, 3, 6, 11$, and 22 are indeed dense. In addition, these fields contain at least one massive cluster or one massive galaxy group (more discussion in chapter 4).

There are 25 objects that were observed in two different overlapping AAOmega fields. The majority of these objects $N = 19$ lie on the overlap area between fields F23 and F25, 2 on fields F11 and F36 as well as fields F06 and F06Y each. The last two double observed objects are on fields F20 and F22 and fields F11 and F35 each. Table 2.2 presents the names of the galaxies observed twice in two different fields, its redshifts in km s^{-1}, the difference between the two measured redshifts in km s^{-1}, and the velocity errors. There are two extreme outlier cases observed within fields F23 and F25, one galaxy has a star contaminating its spectrum and the second one has an offset of $\sim 10\%$ between the duplicate measured redshifts. To assess the reliability of the AAOmega redshifts, I compare the redshifts of the doubly observed galaxies. The standard deviation of the doubly observed galaxy velocities is $\sim 40\,\mathrm{km\ s^{-1}}$. This value is comparable to the typical velocity errors in each duplicate galaxy measurement. This indicates the high efficiency of the AAOmega spectrograph, and consequently, the accuracy of our data. Figure 2.7 shows the velocity scatter of the double observed galaxies, after excluding the star contaminated ones.

In total 4344 galaxies were observed with the 2dF+AAOmega spectrograph in 25 fields, of those we have science quality redshifts for 4126 galaxies, excluding the duplicate galaxies listed in Table 2.2. In our subsequent analysis, and throughout this thesis, we only used the redshifts with high reliability (flag 4&3). Figure 2.8 presents the velocity distribution histogram of the galaxies observed using the AAOmega redshifts, out to $V_{hel} = 50000\,\mathrm{km\ s^{-1}}$ and with bin size of $V = 1000\,\mathrm{km\ s^{-1}}$. In this histogram one can identify three peaks. The main body of the Vela overdensity is represented by the prominent peak centred at $18000 \pm 1000\,\mathrm{km\ s^{-1}}$ and associated with extended shoulders that range from 15000km s^{-1} to 22000km s^{-1}. This velocity distribution is very similar to that of the Shapley Supercluster (Proust et al. 2006), based on full systematic mapping of Shapley Supercluster (refer to Figure1.8), although Vela is a bit further away on average ($f = 1.2$). This is the first indication that the Vela overdensity is likely a massive supercluster. Before analysing this in further details, we will first explore the other redshifts data available in the Hydra/Antlia and Vela survey regions.

Table 2.1: Summary of the observed ZoA galaxies with the 2dF+AAOmega spectrograph in 2014.

stats	Field	(l°,b°)	N_{gal}	$N_{fibered}$	N%	stars*	no z	$N_{good\ z}$	good z(%)
Colu.	1	2	3	4	5	6	7	8	9
	06	264.1,-9.1	347	293	84.43	13	11	282	96.24
	20	272.5,-8.8	286	270	94.40	10	11	259	95.92
	02	250.0,-8.3	247	219	88.66	28	6	213	97.26
	03	248.0,-7.8	235	202	85.95	12	4	198	98.01
	11	272.3, 7.8	232	194	83.62	9	4	190	97.93
	12	274.3, 8.3	231	204	88.31	11	8	196	96.07
	22	274.1,-9.4	210	185	88.09	6	6	179	96.75
	17	279.9, 6.6	209	197	94.25	15	9	188	95.43
	24	278.1,-8.7	206	199	96.60	11	7	192	96.48
	23	276.1,-9.2	205	198	96.58	17	8	190	95.95
	08	260.3, 7.6	203	188	93.06	10	4	184	97.87
	05	259.6,-8.4	183	166	90.71	5	12	154	92.77
	09	262.3, 7.7	183	171	93.44	11	5	166	97.07
	25	276.4,-7.6	174	166	95.40	13	5	161	96.98
	21	273.2,-6.9	167	160	95.80	14	7	153	95.62
	19	281.7, 7.6	166	156	93.97	3	10	146	93.58
	31	265.9, 7.3	165	156	94.54	5	6	150	96.15
	18	281.6, 5.5	152	146	96.05	13	9	137	93.83
	32	266.7, 9.6	149	131	87.91	11	4	127	96.94
	06Y	266.0,-9.3	149	138	92.61	16	14	124	89.85
	38	276.2, 9.2	147	133	90.47	8	5	128	96.24
	36	273.7, 6.5	133	125	93.98	4	4	121	96.80
	34	269.9, 7.6	127	120	94.48	10	9	111	92.50
	35	271.6, 6.0	126	115	91.26	10	4	111	96.52
	13	276.6, 4.5	115	112	97.39	11	10	102	91.07
Total	-	-	4747	4344	<92.078>	276	182	4162	<95.59>

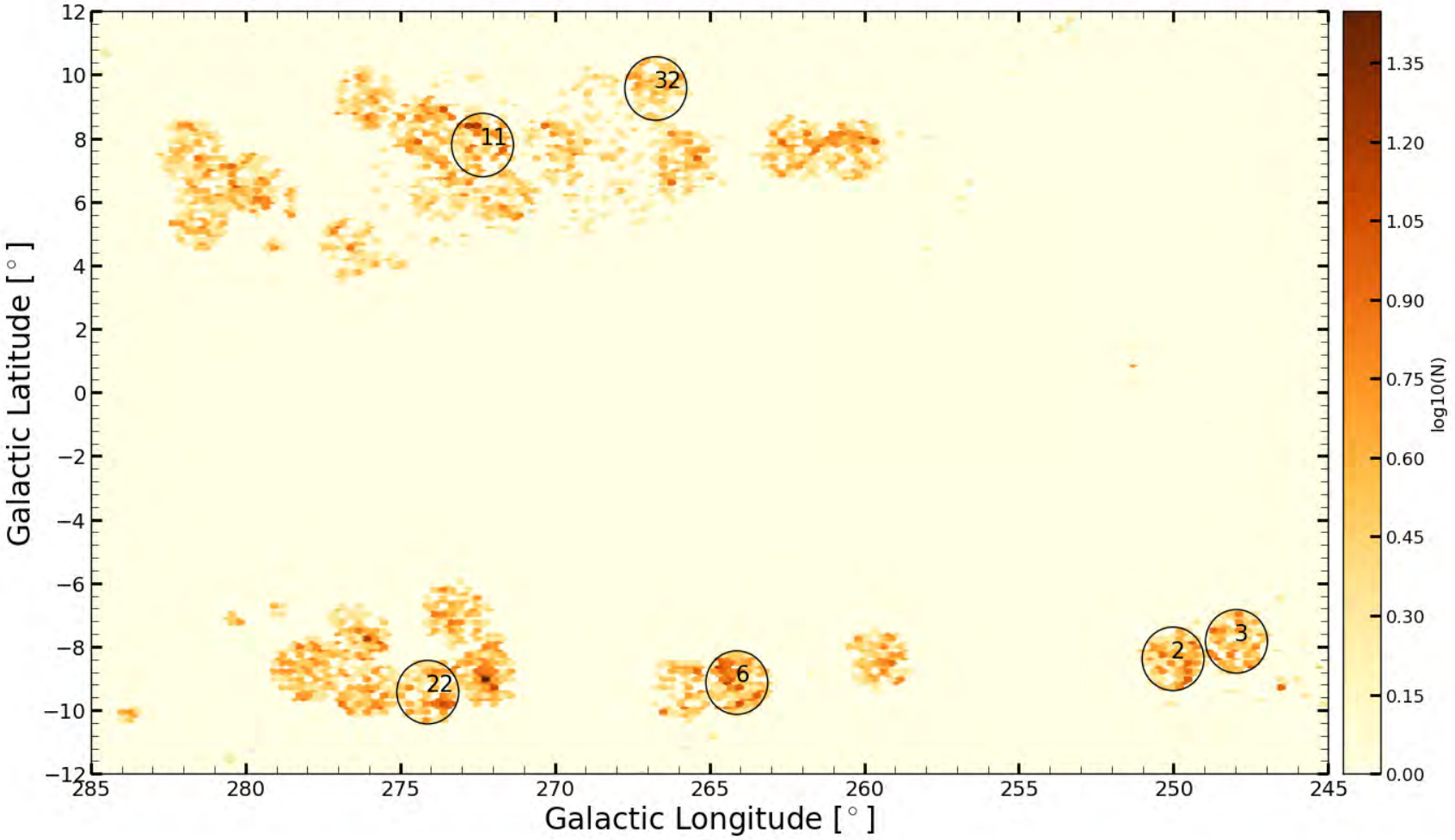

Figure 2.6: Density plot of the galaxies observed with 2dF+AAOmega in the Hydra/Antlia and Vela regions, the black circles mark AAOmega $2, 3, 6, 11, 22$ and 32 fields. This figure shows that the fields $2, 3, 6, 11$, and 22 are dense, which explains why the percentage of the unfibred galaxies in these fields are a bit higher than the remaining fields.

Table 2.2: The Doubly observed galaxies, the AAOmega fields, velocities, velocity difference, and velocity errors.

Name	Field	v_{rel} [km s^{-1}]	Δv_{rel} [km s^{-1}]	ϵv_{rel} [km s^{-1}]
2MX08080831 − 5002571 − 4120	F06	31794	52	47
	F06Y	31742		45
2MX08083602 − 5001060 − 1458	F06	19126	27	36
	F06Y	19153		39
2MX08394943 − 5641132	F20	17732	16	40
	F22	17716		39
2MX08562736 − 5822233	F23	37698	16	43
	F25	37714		47
2MX08572646 − 5845434	F23	17	80043	23
	F25	80060		23
2MX08574651 − 5832175	F23	106609	8099	22
	F25	98510		22
2MX08575239 − 5833115 − 770	F23	15997	110	28
	F25	15887		27
2MX08581797 − 5838193 − 783	F23	10166	1	25
	F25	10167		26
2MX08585847 − 5840453	F23	37387	11	48
	F25	37398		50
2MX08590185 − 5833332	F23	35107	95	28
	F25	35012		28
2MX08591875 − 5835299 − 811	F23	17622	2	23
	F25	17624		23
2MX08592719 − 5838460	F23	15363	14	26
	F25	15349		24
2MX08592796 − 5837090 − 823	F23	22566	42	25
	F25	22524		25
2MX08594579 − 5856199	F23	32	8	42
	F25	24		50
2MX08575834 − 5824384 − 774	F23	34738	36	49
	F25	34702		49
2MX09523500 − 4509537	F11	46832	37	46
	F36	46869		48
Vel−3067	F11	19851	34	26
	F35	19817		36
Vel−4267	F11	29529	15	28
	F36	29514		31
HyA−769	F23	36318	5	23
	F25	36323		24
HyA−755	F23	31347	43	52
	F25	31390		26
HyA−772	F23	28523	20	28
	F25	28503		23
HyA−773	F23	15384	41	24
	F25	15343		25
HyA−749	F23	37878	64	65
	F25	37814		46
HyA−771	F23	16061	7	23
	F25	16068		24
HyA−730	F23	15367	2	23
	F25	15365		23

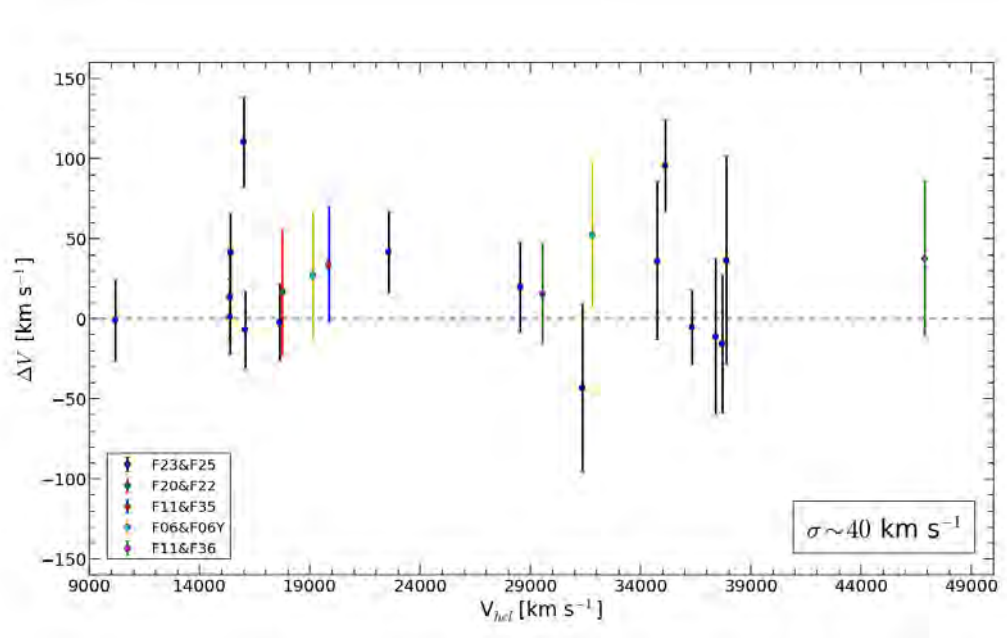

Figure 2.7: Velocity scatter for galaxies observed in two different AAOmega fields. Each colour corresponds to an overlap area of two AAOmega fields. The x-axis presents the velocities of the duplicate galaxies in one of the overlapped fields and the y-axis shows Δv_{rel} of the doubly observed galaxies between the two different fields.The errorbars are the averaged velocity error measurement for the specific doubly observed galaxy in the two different fields.

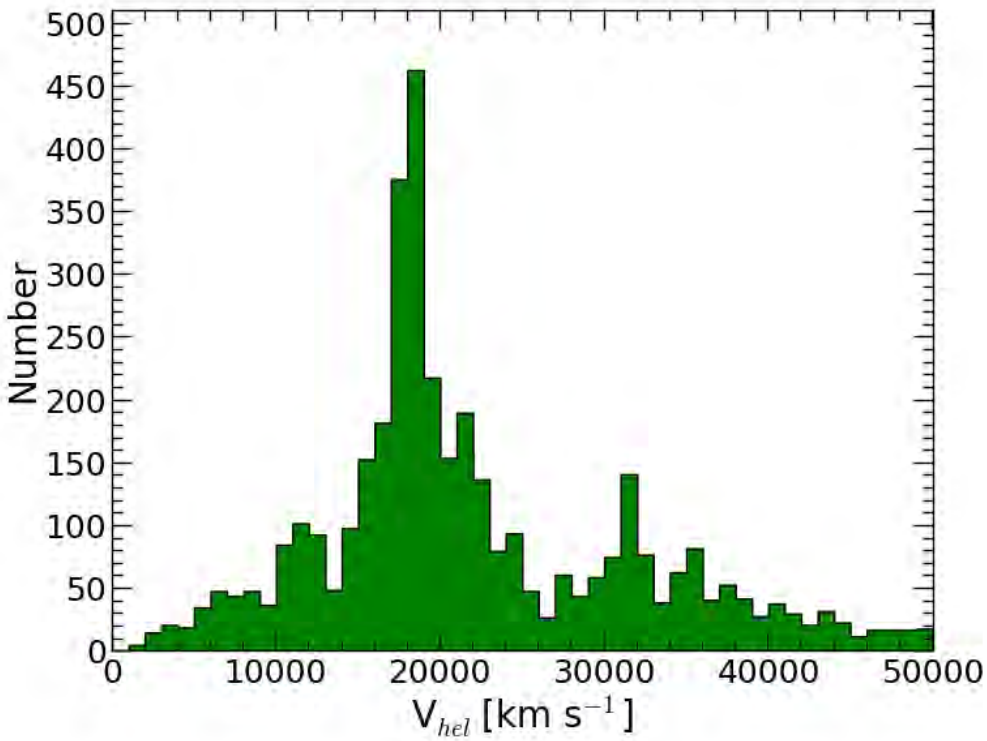

Figure 2.8: Velocity distribution of the galaxies observed using AAOmega redshifts, out to $V_{hel} = 50000\,\mathrm{km\ s^{-1}}$ and with a bin size of $V = 1000\,\mathrm{km\ s^{-1}}$. The main body of the Vela overdensity is represented by the prominent peak centred at $18000 \pm 1000\,\mathrm{km\ s^{-1}}$ and associated with extended shoulders that range from $15000\,\mathrm{km\ s^{-1}}$ to $22000\,\mathrm{km\ s^{-1}}$.

2.2.2 SALT and SAAO

Observations using the Southern African Large Telescope (SALT) were conducted in 2012-2013. The targeted galaxies were observed using the Robert Stobie Spectrograph (RSS) instrument with multi-slit spectroscopy. The main purpose of these observations is to obtain the redshift values for the core of potential galaxy clusters in the Vela Overdensity rather than systematically map the Vela and Hydra/Antlia regions. 13 different fields were observed, each field is $8' \times 8'$ on the sky. A total of 118 galaxies within Vela region were observed. Redshifts were extracted by T. Jarrett for 89 galaxies. Comparing the SALT data with the 2dF redshifts, 31 duplicate galaxies were found. Figure 2.9 shows the velocity scatter between the crossmatched galaxies. This time to test how accurate SALT measurements are for highly obscured galaxies in the ZoA. SALT redshifts of flag 1&2 were excluded, flag 1 and 2 usually indicate a high uncertainty in the measurement of the redshift and therefore, should be excluded from our calculations. The velocity scatter between these two different sets of data is $\sim 209\,\mathrm{km\ s^{-1}}$. The exposure time for the SALT observations was between from $12 - 20\,\mathrm{min}$, while for the AAOmega was around $60 - 90\,\mathrm{min}$. Therefore, this difference in exposure times balances the difference in aperture quite well. This

suggests that the errors of the SALT spectroscopy are larger than the AAOmega spectra, which is not unexpected when comparing the quality of the spectra. In total 72 SALT redshift measurements were added to the Master Catalogue, of which 38 are flags 4&3 redshifts.

Along with the SALT observations, observations for 54 galaxies were conducted at the South African Astronomical Observatory (SAAO) using the 1.9m telescope in 2010, by Kosma von Maltitz (von Maltitz 2012). Redshifts for 41 galaxies were obtained, 3 crossmatch with the 2dF redshifts and 4 crossmatch with the 6dF redshifts were found. Most of the observed galaxies are very local ($\lesssim 10000\,\mathrm{km\ s^{-1}}$). A total of 34 galaxy redshifts were added to the Master Catalogue.

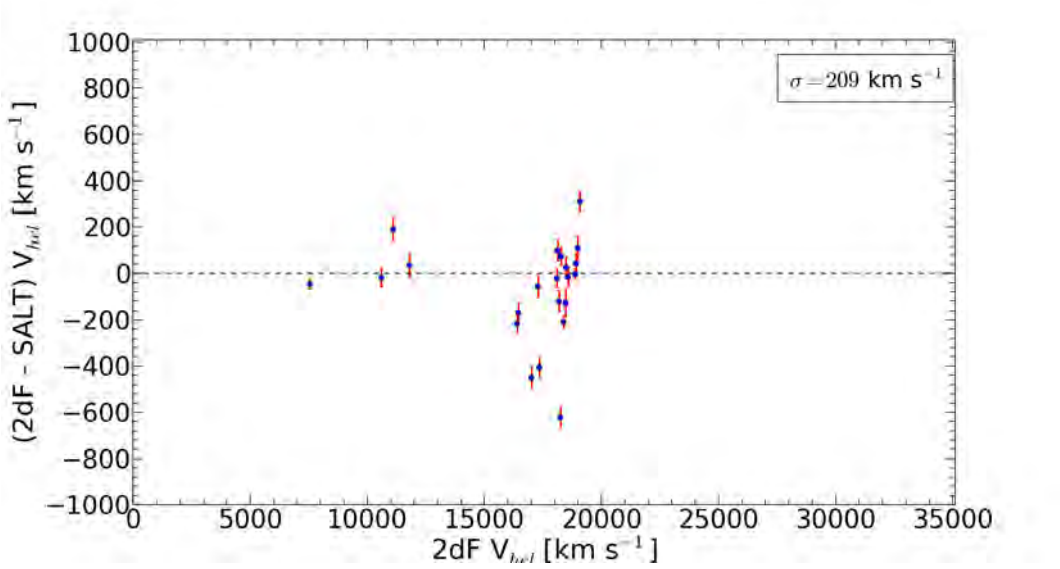

Figure 2.9: Comparison between SALT and the 2dF redshifts.

2.2.3 Other Redshift Data

The original data that gave rise to the suspicion of the Vela access density were based on the Optopus instrument at the European Southern Observatory and the 6dF observations at the Anglo Australian Observatory. In the this section I will describe these two observations.

OPTOPUS

In a chronological order, the first observations in the Vela overdensity region were conducted in 1991-1992 using the Optopus instrument on the ESO 3.6 m telescope at La silla. Using the Optopus system, spectra from up to 47 different objects located within a 33 arcminutes field can be simultaneously recorded. The Optopus instrument was used to observe the Hydra/Antlia regions by Kraan-Korteweg and collaborators in 1991 and 1992. A total of 271 galaxy redshifts were obtained in the Hydra/Antlia regions. Compiling this data with

the AAOmega redshifts, I find 123 crossmatched galaxies. Figure 2.10 shows the velocity scatter of the crossmatched galaxies observed using Optopus and 2dF. After excluding eight extreme points ($\mid 2dF - Opt \mid \geq 500$ km s^{-1}) the velocity scatter in this data is ~ 217 km s^{-1}. The figure also indicates no systematic offset errors. Bearing in mind the typical redshift uncertainty for the AAOmega, ~ 100 km s^{-1} (Baldry et al. 2014), compiling the 2dF and Optopus data is applicable for science purposes. This analysis is similar to the Shapley Supercluster analysis by Proust et al. (2006), whereby they compiled data from 3 major galaxy surveys, namely, Las Campanas observations (Quintana et al. 2000), UKST at Siding Spring, Australia (Drinkwater et al. 1999), and from the ESO 3.6 m telescope equipped with the Optopus spectrograph at La Silla, Chile (Quintana et al. 1997). Proust and collaborators eliminated the crossmatched galaxies that have scatter larger than 200 km s^{-1}. In total 146 Optopus redshift measurements were added to the Master Catalogue.

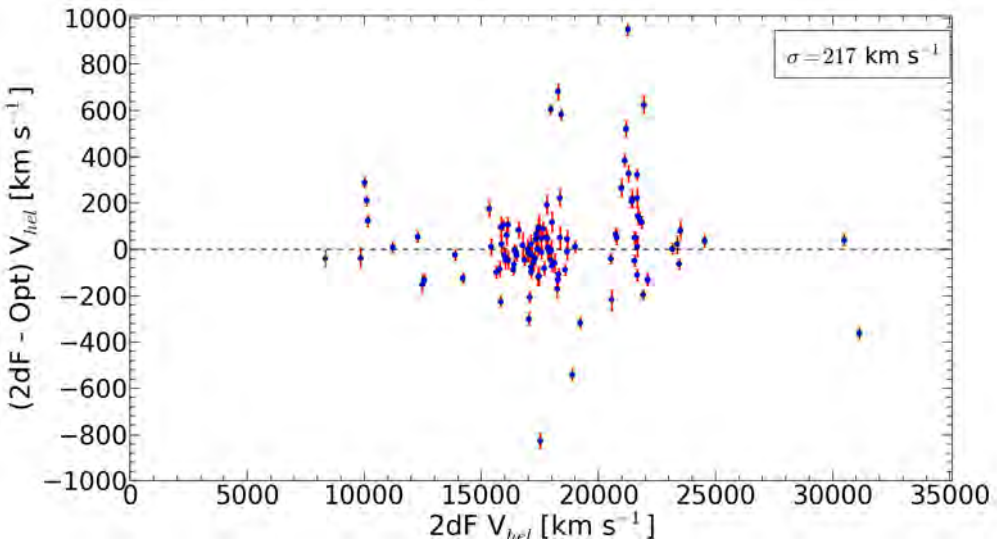

Figure 2.10: Comparison between Optopus and 2dF redshifts.

6dF

The 6dF is a multi-object spectroscopy system previously mounted on the Anglo Australian Observatory's 1.2 m UK Schmidt Telescope. It uses a robotic fibre positioner to configure up to 150 fibres on interchangeable field-plate units, which replaces the original photographic plateholders of the telescope. The system was built by the AAO and commissioned in 2001. Until August 2005, the instrument was used for 6dF Galaxy Survey observations and common-user non-survey observations (Watson et al. 2001, Wakamatsu et al. 2003).

Observations using the 6dF were conducted on various nights from April to July 2001 during the commissioning time of the system by Kraan-Korteweg and collaborators. At that point of time some test fields at lower latitudes were scheduled for the mapping of the large-

scale structure in the ZOA. This with the goal to investigate the efficiency of using 6dF at low Galactic latitudes possibly to extend the 6dF survey to lower latitudes, at least in parts of the ZOA. The observations were conducted using various exposure times with blue and red filters. The 6dF observations mapped two adjacent fields in the Vela region and yielded 373 galaxy redshifts, covering the region ($l \simeq 265° - 275°, b \simeq 5° - 10°$). Comparing this data set with AAOmega redshifts, I find 126 crossmatched galaxies. Figure 2.11 shows the velocity scatter in the crossmatched galaxies observed using the 2dF and the 6dF. Although there are 126 duplicate galaxies, this plot only presents 89 galaxies. The remaining galaxies have unreliable 6dF redshifts measurements, flag 1&2 redshifts. After excluding four extreme redshift measurements ($\mid 2dF - 6dF \mid \geq 500$ km s^{-1}), the standard deviation of the remaining crossmatched objects is ~ 194 km s^{-1}. The figure also indicates the absence of systematic offset errors. Taken together, this shows that compiling the 6dF data with the 2dF data is very reliable for science purposes, bearing in mind also that the typical redshift uncertainty for the AAOmega is about ~ 100 km s^{-1} (Baldry et al. 2014). In total 124 6dF redshift measurements were added to the Master Catalogue, of which 86 are flags 3&4 redshifts.

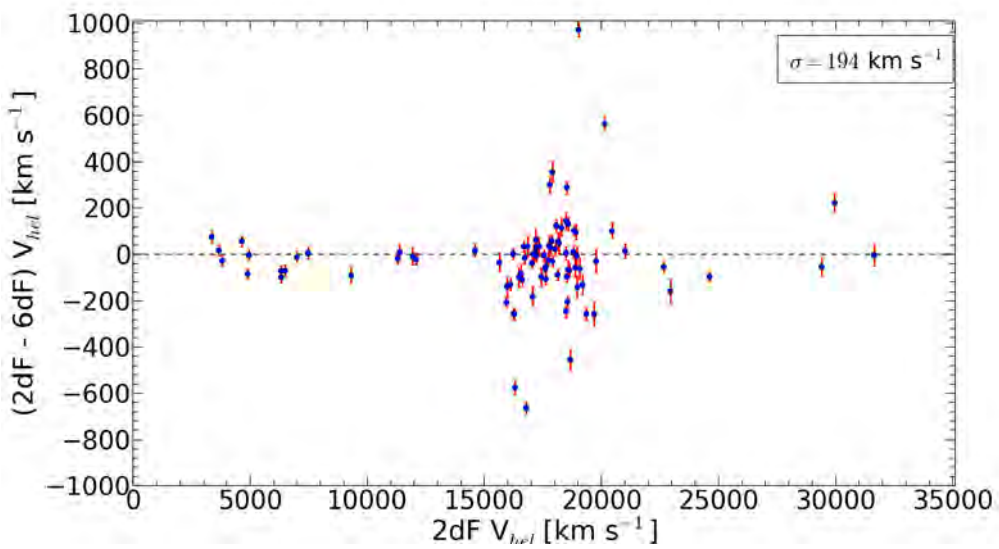

Figure 2.11: Comparison between the 6dF and the 2dF redshifts.

Literature Search

For the galaxies not observed by these campaigns, we checked the availability of redshifts in the literature using the extragalactic database HYPERLEDA within our survey area. A total of 760 galaxy redshifts were found. Compiling all the above redshifts as well as data from the extragalactic database HYPERLEDA, we have a total of 5480 redshifts in the Master Catalogue, of which 5190 redshifts are science quality redshifts. In our subsequent analysis, and throughout this thesis, we only used the science quality redshifts (flag 4&3).

Table 2.3: The Master Catalogue entries description.

Column	Description
1	A symbol for the catalogue P1: Both optical and 2MASS XSC galaxy, P3: Only optical catalogue galaxy, P5: Only 2MASS XSC galaxy.
2	The ID
3	α Right Ascension (J2000.0).
4	δ Declination (J2000.0).
5	l Galactic longitude.
6	b Galactic latitude.
7	Major axis in arcsec, as determined from B_J sky survey plates.
8	Minor axis in arcsec, as determined from B_J sky survey plates.
9	B_J Isophotal apparent magnitude.
10	$E(B-V)$ value as determined in Schlafly & Finkbeiner (2011).
11	D^0 Extinction-corrected major diameter.
12	B_J^0 Extinction-corrected magnitude.
13	Morphology.
14	Isophotal K_s-band total magnitude.
15	Isophotal K_s^0-band total magnitude.
16	Redshift.
17	Redshift flag.
18	Redshift Source

Of the 5190 galaxy redshifts, 1560 are optical galaxies with no counterparts in the 2MASS XSC, 1568 are optical galaxies with counterparts in the 2MASS XSC, and the remaining 2062 galaxies belong to the 2MASS XSC with no optical counterparts.

2.3 Catalogue Description

The Master Catalogue entries description is provided in Table 2.3. The catalogue is listed in Appendix A. It is important to mention that the $E(B-V)$ values are calibrated according to Schlafly & Finkbeiner (2011), the $E(B-V)$ values are taken from the the NASA/IPAC Infrared Science Archive*. The major and minor diameter axes were estimated from the magnified plates images using a ruler in units of millimetres. Then a conversion factor was applied to convert to units of arcsecs, based on the UK Schmidt Telescope Handbook, 1983. The major diameter and the B_J isophotal apparent magnitude are extinction-corrected using Cameron (1990) optimised approach in correcting for foreground dust extinction. On the other hand, I followed Riad et al. (2010) approach based on the central surface brightness μ_c to correct for foreground dust extinction in the isophotal K_s-band magnitude. For a more rigorous description on the morphology of the galaxies in this catalogue (Column 13) refer to Kraan-Korteweg (2000a) and von Maltitz (2012).

*http://irsa.ipac.caltech.edu/applications/DUST/docs/background.html

2.4 Summary

This chapter presented the combined optical-2MASS galaxy catalogue that we built, called the Master Catalogue. The optical part of this catalogue is based on deep optical galaxy source catalogues in the ZoA in the Hydra/Antlia and Vela regions ($245° \lesssim l \lesssim 295°, |b| \lesssim 10°$) (Kraan-Korteweg 2000a, von Maltitz 2012), whereas the second component originates from the near infrared 2MASS Extended Source Catalogue (XSC) (Jarrett et al. 2000a, Skrutskie et al. 2006). This catalogue forms the basis of the systematic redshifts observations in the Hydra/Antlia and Vela regions. An epitomized description of these different observations conducted to unveil the large-scale structures, hidden by the dust of the Milky Way, in the Hydra/Antlia and Vela regions is presented. The major part of the observed galaxies (80%) are from the 2dF+AAOmega spectrograph observations on the Anglo Australian Telescope in February 2014. We compiled a total of 5480 redshifts in the Master Catalogue, of which 5190 redshifts are science quality redshifts. Table 2.4 presents a short summary on the redshifts sources in the Master Catalogue. Of the 5190 science quality redshifts, 1560 are optical galaxies with no counterparts in the 2MASS XSC, 1568 are optical galaxies with counterparts in the 2MASS XSC, and the remaining 2062 galaxies belong to the 2MASS XSC with no optical counterparts.

Table 2.4: Summary on the redshifts sources in the Master Catalogue.

Observations	Flags 4&3	Flags 1&2
2dF+AAOmega	4126	218
Optopus	146	-
6dF	86	38
SALT	38	34
1.9 m SAAO	34	-
HYPERLEDA	760	-
Total	5190	290

Chapter 3

Redshifts Analysis

The following sections present the velocity distribution of the galaxies in the direction of the proposed Vela Supercluster (VSC), as well as the structures of this overdensity in velocity wedge diagrams. In our subsequent analysis, and throughout this thesis, we only used the redshifts with high reliability (flag 4&3), these are 5,190 galaxy redshifts in the direction of Hydra/Antlia and Vela regions.

3.1 The Velocity Distribution of the Vela Supercluster

Figure 3.1 presents the on-sky distribution of all the galaxies available in the direction of the Vela overdensity. These galaxies are colour-coded according to different velocity slices. Black are galaxies with velocities $v < 15000\,\mathrm{km\ s^{-1}}$, red are galaxies in the velocities range $15000 < v < 25000\,\mathrm{km\ s^{-1}}$, and green are galaxies with velocities $v > 25000\,\mathrm{km\ s^{-1}}$. The black circles mark the AAOmega observation fields, from which the majority of our data originate. The Vela overdensity is conspicuous in 20 of the 25 AAOmega fields and can be traced for $\Delta l \sim 25^\circ$ above the plane in the range($285^\circ > l > 260^\circ$), and for $\Delta l \sim 20^\circ$ below the plane in the range ($280^\circ > l > 260^\circ$). Moreover, the velocity histograms on both side of the plane are remarkably similar (refer to Fig.3.3-3.4), which brings to prospective that the Vela overdensity might be continuous across the plane (although we lack redshift data in the mostly opaque ZoA) and consequently having a width of about $\Delta b \sim 20^\circ$ across the plane.

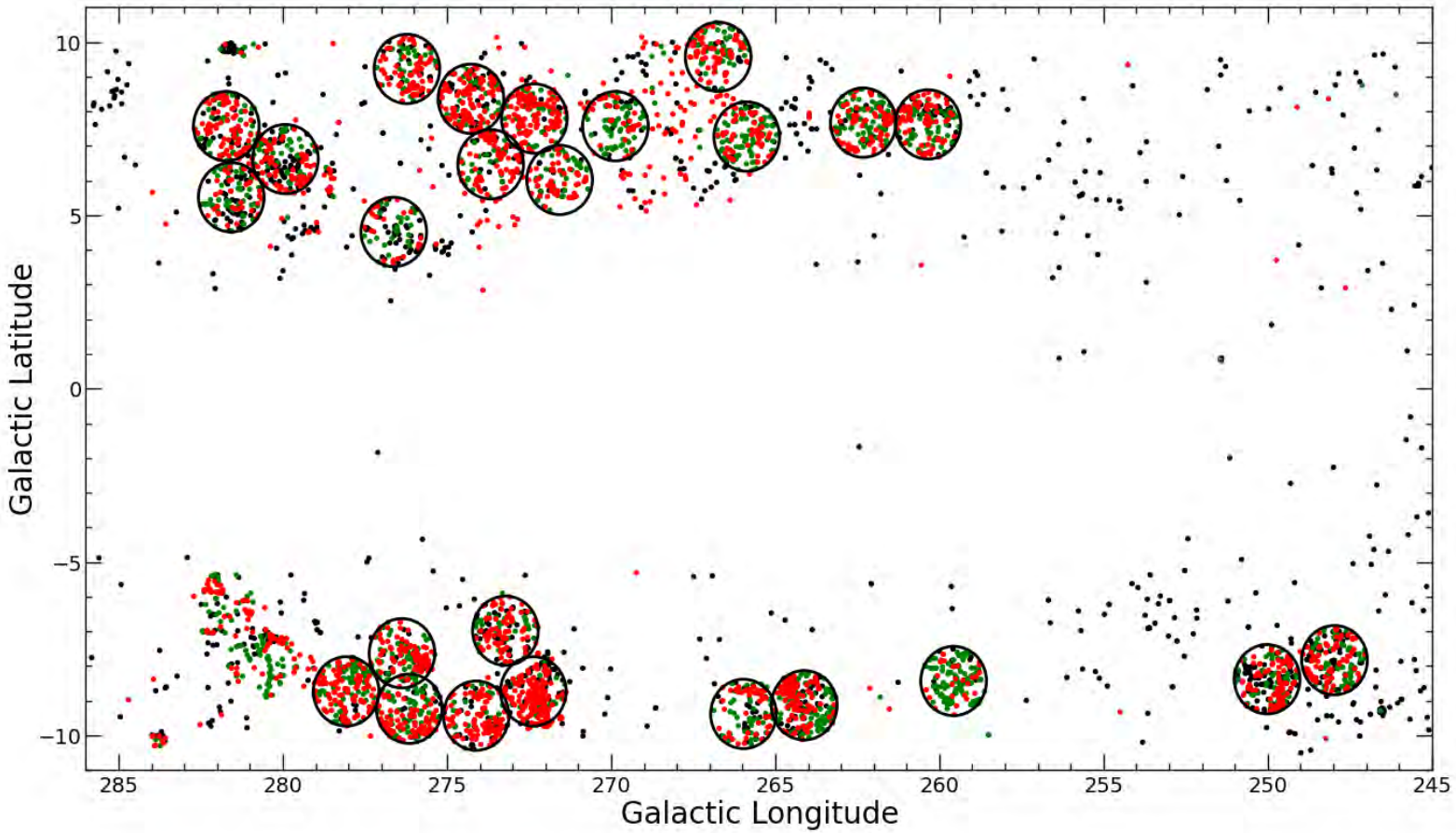

Figure 3.1: The on-sky distribution of all the galaxies available in the direction of the Vela overdensity, these galaxies are colour-coded according to there different velocities. Black are galaxies with ($v < 15000\,\mathrm{km\ s^{-1}}$), red are galaxies in the velocities range ($15000 < v < 25000\,\mathrm{km\ s^{-1}}$), and green are galaxies with velocities ($v > 25000\,\mathrm{km\ s^{-1}}$). The black circles delimit the AAOmega observation fields.

Figure 3.2 shows the velocity distribution of the galaxies in the direction of the Vela overdensity in velocity range from $0 < v < 50000\,\mathrm{km\ s^{-1}}$, and with bin size of $1000\,\mathrm{km\ s^{-1}}$. The main body of the Vela overdensity is represented by the salient peak at $v \sim 18000 \pm 1000\,\mathrm{km\ s^{-1}}$ and associated with very broad buttresses extending from $15000 - 23000\,\mathrm{km\ s^{-1}}$. This velocity distribution is nearly indistinguishable from that of the Shapley Supercluster (SSC), based on full systematic mapping of the SSC (refer to Fig.2 in Proust et al. (2006)). However, Vela is a bit further away on average ($f = 1.2$). This is the first indication that the Vela overdensity likely is a massive supercluster.

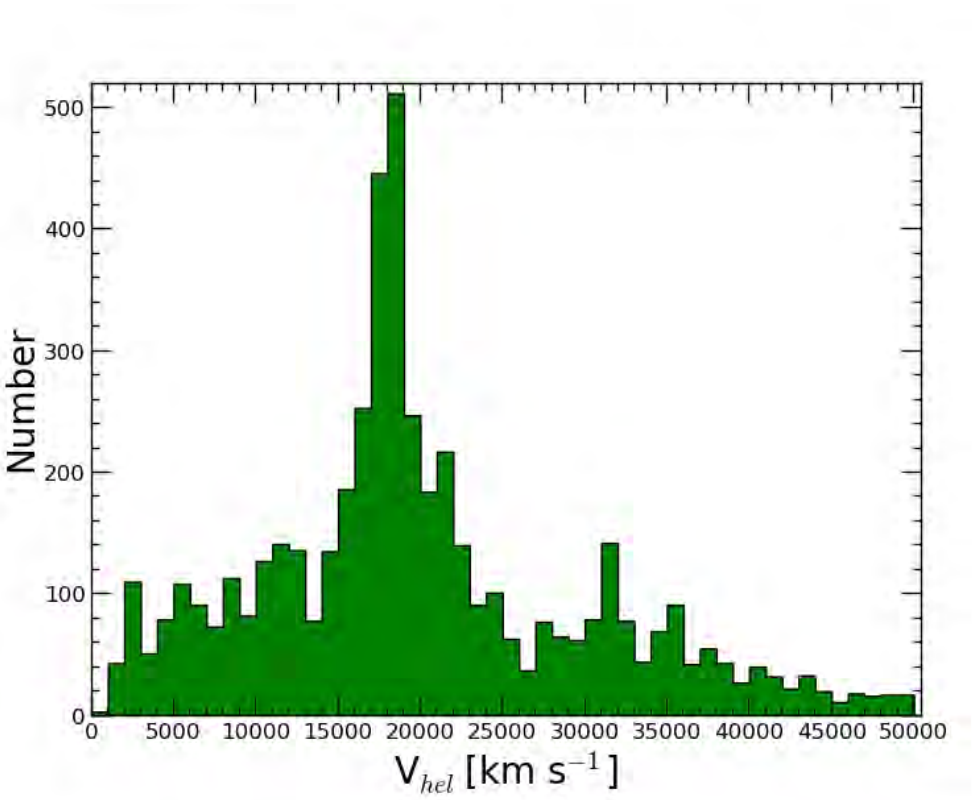

Figure 3.2: Velocity distribution of the galaxies in the direction of Vela overdensity based on the velocities available in our survey area ($245^\circ \lesssim l \lesssim 295^\circ, |b| \lesssim 10^\circ$), most of these redshifts are from the AAOmega observations.

In Figs. 3.3-3.4, I show the velocity distribution of the galaxies in the direction of the Vela overdensity above and below the Galactic plane, respectively, with velocity range from $0 < v < 50000\,\mathrm{km\ s^{-1}}$, and bin size of $1000\,\mathrm{km\ s^{-1}}$. These velocity histograms indicate that this overdensity is equally prominent on each side of the Galactic plane, which hints that the Vela overdensity might be continuous across the plane and as a result have a width of about $\Delta b \sim 20^\circ$ across the plane.

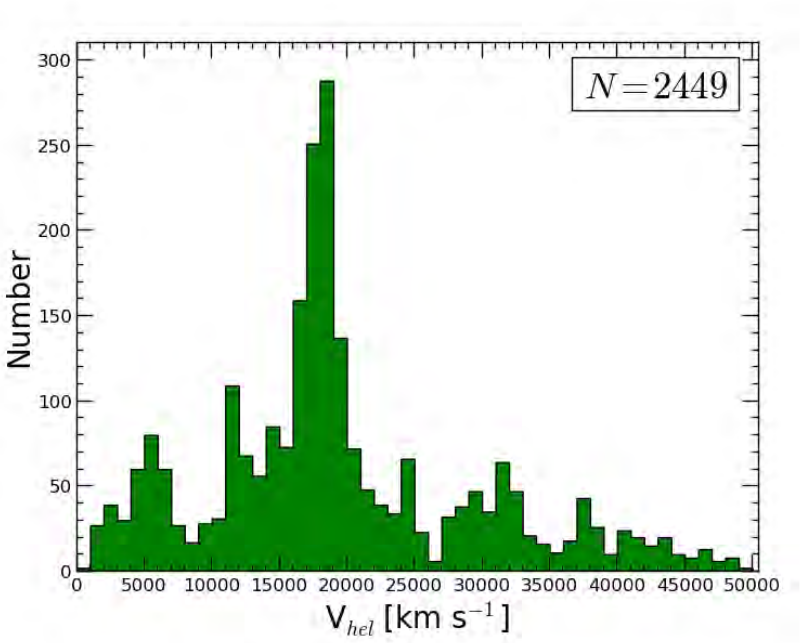

Figure 3.3: Velocity distribution of the galaxies in the direction of Vela overdensity based on the velocities available in our survey area ($245° \lesssim l \lesssim 295°, 0° \leq b \leq 10°$). There are 2,449 galaxy redshifts available within this velocity range.

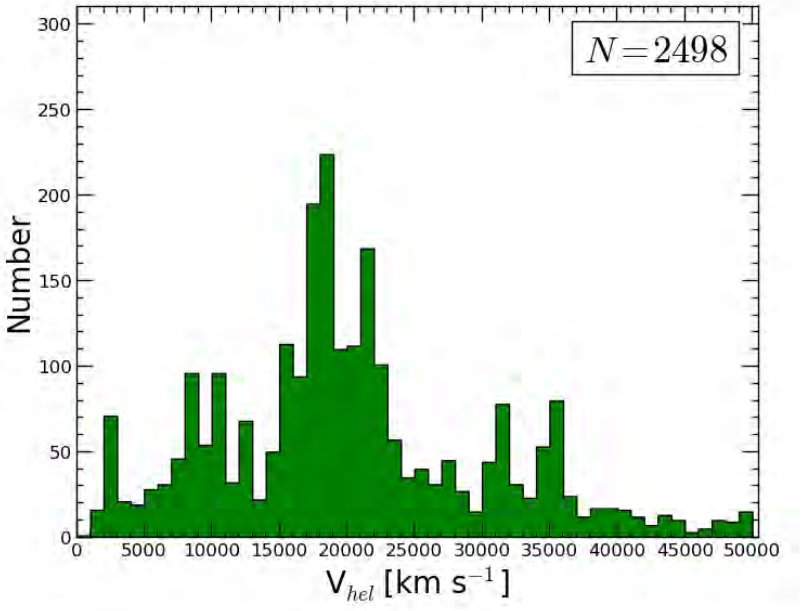

Figure 3.4: Velocity distribution of the galaxies in the direction of Vela overdensity based on the velocities available in our survey area ($245° \lesssim l \lesssim 295°, -10.0° \leq b \leq 0°$). There are 2,498 galaxy redshifts available within this velocity range.

The structure and the extent of the prospective VSC can be further analysed by inspecting the on-sky distribution of the galaxies in different velocity ranges. Figures 3.5-3.7 present the on-sky distribution of the galaxies in the direction of the potential VSC in the range $245° < l < 295°$ and $-10.0° < b < 10.0°$. Figure 3.5 encapsulates the nearby galaxies within velocity range from $3000 < v < 13000\,\mathrm{km\ s^{-1}}$. These galaxies are colour-coded according to velocity. Black are galaxies within the velocity range $3000 < v < 5500\,\mathrm{km\ s^{-1}}$, red are galaxies within velocity range $5500 < v < 8000\,\mathrm{km\ s^{-1}}$, green are galaxies within velocity range $8000 < v < 10500\,\mathrm{km\ s^{-1}}$, and blue are galaxies within velocity range $10500 < v < 13000\,\mathrm{km\ s^{-1}}$. There are galaxy agglomerations above and below the plane, these galaxies are mostly centred at $v \sim 10,000\,\mathrm{km\ s^{-1}}$ and possibly form galaxy groups (one possible galaxy group is found and marked with the black circle, see chapter 4).

Figure 3.6 encloses the more distant galaxies with velocity range from $13000 < v < 25000\,\mathrm{km\ s^{-1}}$. These galaxies are colour-coded according to different velocity slices. Black are galaxies within velocity range $13000 < v < 16000\,\mathrm{km\ s^{-1}}$, red are galaxies within velocity range $16000 < v < 19000\,\mathrm{km\ s^{-1}}$, green are galaxies within velocity range $19000 < v < 22000\,\mathrm{km\ s^{-1}}$, and blue are galaxies within velocity range $22000 < v < 25000\,\mathrm{km\ s^{-1}}$. There is a high increment in the density of the galaxies in Fig. 3.6; this is expected because the potential VSC lies within this velocity range. A number of dense areas have been recognised as potential galaxy clusters and groups. These are marked with the black circles (more discussion in chapter 4). Interestingly, this overdensity persists prominently on either side of the Galactic plane, which agrees with our conclusion from the velocity histograms of the galaxies above and below the Galactic plane, refer to Fig.3.3-3.4. This is a further evidence that the proposed VSC extends over a large area of the sky, straddling the Galactic Plane.

Figure 3.7 presents the most distant galaxies within velocity range from $25000 < v < 35000\,\mathrm{km\ s^{-1}}$. These galaxies are colour-coded according to different velocity slices. Black are galaxies within velocity range $25000 < v < 27500\,\mathrm{km\ s^{-1}}$, red are galaxies within velocity range $27500 < v < 30000\,\mathrm{km\ s^{-1}}$, green are galaxies within velocity range $30000 < v < 32500\,\mathrm{km\ s^{-1}}$, and blue are galaxies within velocity range $32500 < v < 35000\,\mathrm{km\ s^{-1}}$. The galaxy agglomerations in figure 3.7 indicate the background structures to the proposed VSC at approximately $v \sim 31,000\,\mathrm{km\ s^{-1}}$ (2 possible galaxy groups are found and marked with the black circles, more in chapter 4).

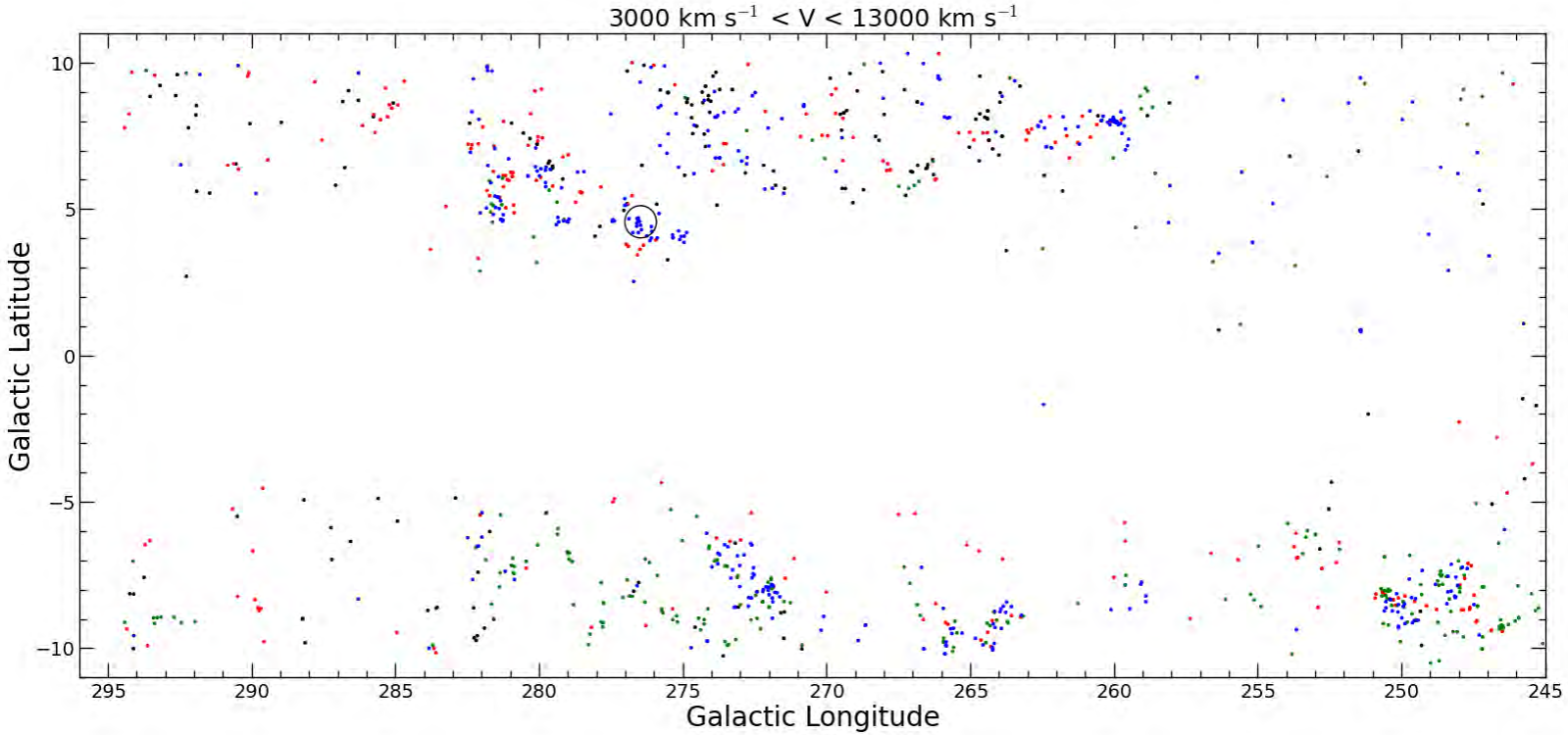

Figure 3.5: On-sky distribution of the galaxies in the direction of the prospective VSC, with velocity range from $3,000 < v < 13,000\,\mathrm{km\ s^{-1}}$. These galaxies are colour-coded according to different velocity slices. Black are galaxies within velocity range $3000 < v < 5500\,\mathrm{km\ s^{-1}}$, red are galaxies within velocity range $5500 < v < 8000\,\mathrm{km\ s^{-1}}$, green are galaxies within velocity range $8000 < v < 10500\,\mathrm{km\ s^{-1}}$, and blue are galaxies within velocity range $10500 < v < 13000\,\mathrm{km\ s^{-1}}$.

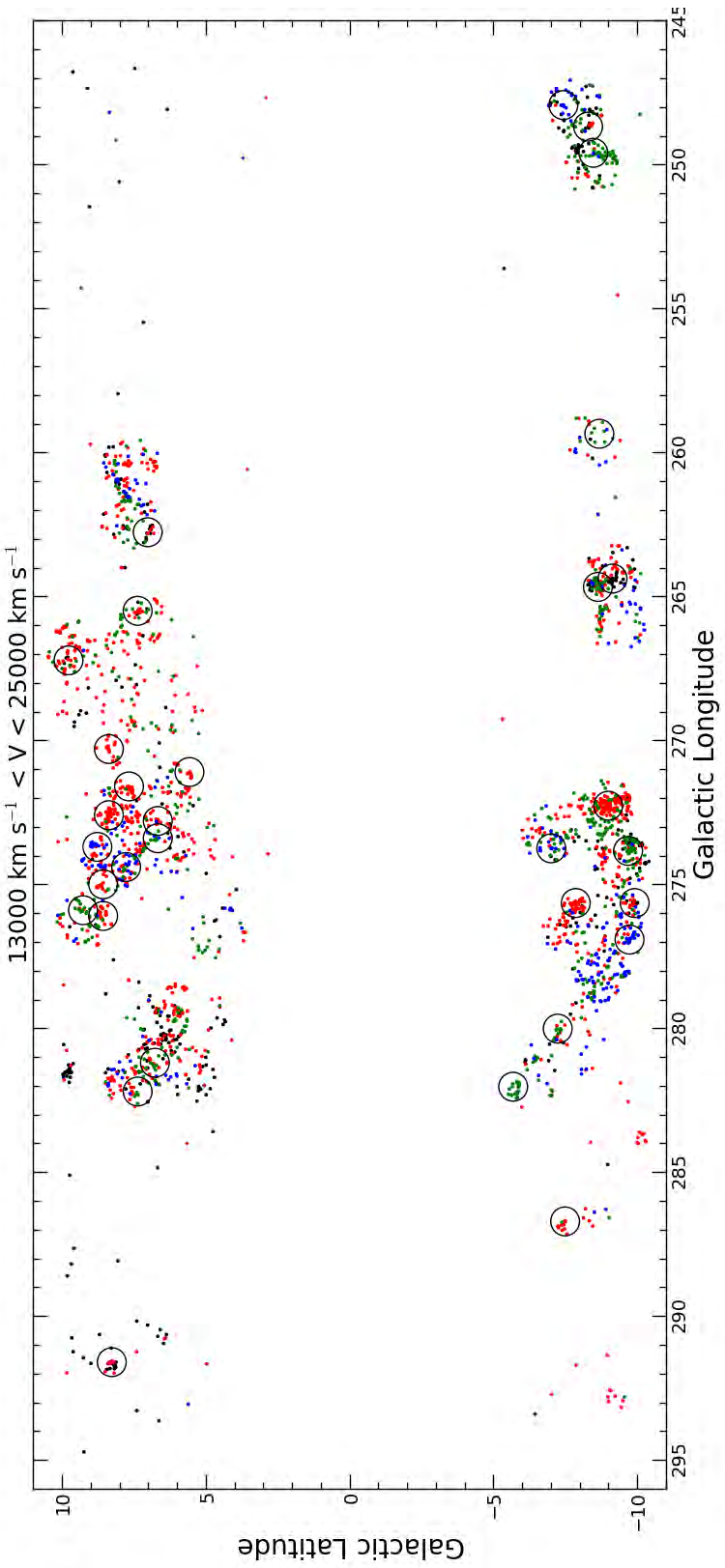

Figure 3.6: On-sky distribution of the galaxies in the direction of the prospective VSC, with velocity range from $13,000 < v < 25,000\,\mathrm{km\ s^{-1}}$. These galaxies are colour-coded according to different velocity slices. Black are galaxies within velocity range $13000 < v < 16000\,\mathrm{km\ s^{-1}}$, red are galaxies within velocity range $16000 < v < 19000\,\mathrm{km\ s^{-1}}$, green are galaxies within velocity range $19000 < v < 22000\,\mathrm{km\ s^{-1}}$, and blue are galaxies within velocity range $22000 < v < 25000\,\mathrm{km\ s^{-1}}$.

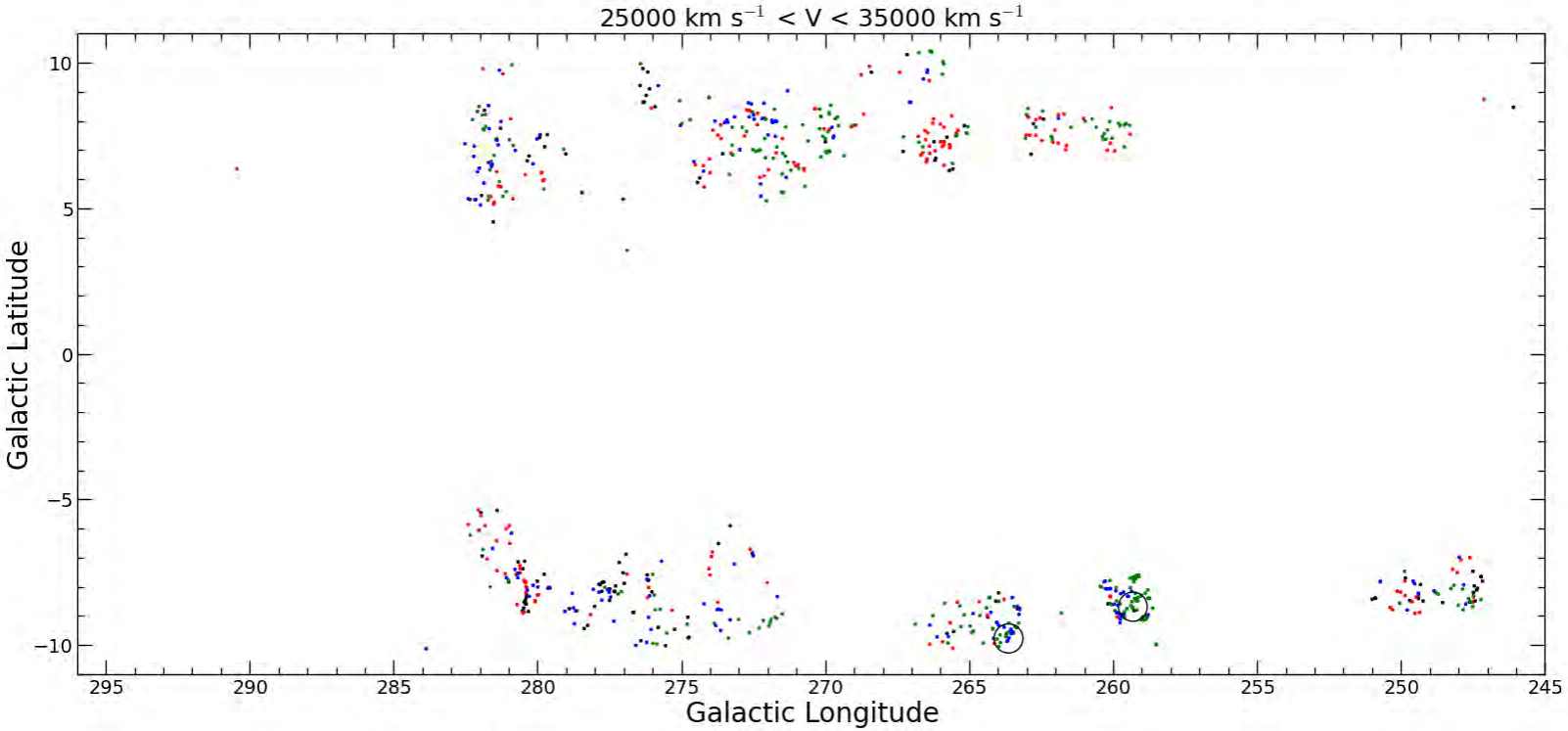

Figure 3.7: On-sky distribution of the galaxies in the direction of the prospective VSC, with velocity range from $25,000 < v < 35,000\,\mathrm{km\ s^{-1}}$. These galaxies are colour-coded according to different velocity slices. Black are galaxies within velocity range $25000 < v < 27500\,\mathrm{km\ s^{-1}}$, red are galaxies within velocity range $27500 < v < 30000\,\mathrm{km\ s^{-1}}$, green are galaxies within velocity range $30000 < v < 32500\,\mathrm{km\ s^{-1}}$, and blue are galaxies within velocity range $32500 < v < 35000\,\mathrm{km\ s^{-1}}$.

3.2 Velocity Wedges

This section presents the large-scale distribution of the galaxies in the direction of the proposed VSC using wedge diagrams. These diagrams are simply sectors of circles centred at the Milky Way with radial component of cz, the distance in km s^{-1}, and polar angle of either Galactic longitude or Galactic latitude. Figures 3.8-3.9 and 3.10 show wedge diagrams out to velocities of $v = 30000$ km s^{-1} in the general VSC region, covering the longitude range $245° \leq l \leq 295°$. Figure 3.8 encapsulates all the galaxies above and below the Galactic plane with a width of $\Delta b = 20°$, hence covers the whole ZoA within $|b| \leq 10°$. Figure 3.9 includes all the galaxies above the Galactic plane with a width of $\Delta b = 10°$, thus covering the ZoA within $0° < b < 10.0°$. Figure 3.10 encloses all the galaxies below the Galactic plane with a width of $\Delta b = 10°$, consequently covering the ZoA within $-10° < b < 0°$. Based on Fig. 3.8, the potential VSC shows up as a prominent wall-like structure. It actually consists of two walls, the main wall (wall one) at $v \sim 18000$ km s^{-1} and a smaller one (wall two) at slightly higher velocity. Tracers of wall one appear both above and below the Galactic plane, see Figs. 3.9-3.10. The second wall is present only below the plane (see Fig. 3.10). The large-scale distribution of the galaxies in the prospective VSC resembles the typical morphology of superclusters. In which, the galaxy clusters/groups are embedded in wall-like structures (Einasto et al. 2011a;b), see chapter 4.2. This is a second indicator that the Vela overdensity may form a massive supercluster.

Based on Fig. 3.8, the Vela overdensity occupies the region from $l = 262°$ to $l = 282°$ and in velocity space from approximately $v \sim 16000$ km s^{-1} extending to $v \sim 25000$ km s^{-1}. This indicates a very broad and extremely massive extended object of size of at least 20 degrees both in Galactic longitude and Galactic latitude, which corresponds to 87×87 Mpc on-sky. Figure 3.11 shows a wedge diagram out to velocities of $v = 50000$ km s^{-1} in the general VSC region, covering longitude range $245° \leq l \leq 295°$. Figure 3.11 encapsulates all the galaxies above and below the Galactic plane with a width of $\Delta b = 20°$, therefore covering the ZoA within $|b| \leq 10°$. The wall-like structure of the potential VSC appears prominently in this wedge diagram. Occupying the region from $l = 263°$ to $l = 283°$ and in velocity space from approximately $v \sim 16000$ km s^{-1} extending to $v \sim 25000$ km s^{-1}, the extent of this wall-like structure is about ~ 87 Mpc on-sky.

Figure 3.12 shows galaxies out to velocities of $v = 30000$ km s^{-1} in the general potential VSC region, covering longitude range $255° \leq l \leq 285°$, and encloses all the galaxies above and below the Galactic plane with a width of $\Delta b = 60°$, thus covering the region within $|b| \leq 30.0°$. These galaxies are colour-coded according to different redshift sources. Red are the galaxies in the Master Catalogue, while green are the galaxies available in the literature using the extragalactic database HYPERLEDA* within our survey area. Based on Fig. 3.12, the main wall (wall one) of the potential VSC appears prominently at $v \sim 18000$ km s^{-1}

*http://leda.univ-lyon1.fr/

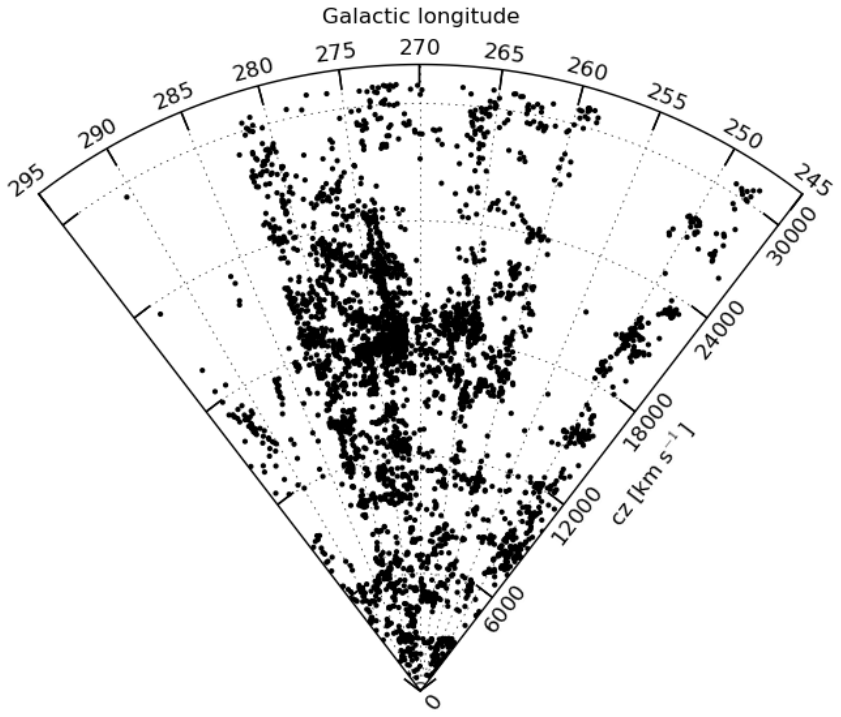

Figure 3.8: Velocity wedge diagram out to velocities of $v = 30000\,\mathrm{km\ s^{-1}}$ in the general proposed VSC longitude range $245° \leq l \leq 295°$ with a width of $\Delta b = 20°$, centred around the ZoA $|b| \leq 10°$.

on either side of the Galactic plane. This provides further evidence that the proposed VSC may well be continuous across the Galactic plane. Although we lack redshift data in the mostly opaque ZoA ($|b| \leq 5°$), the prospective VSC seems to cover the ZoA within $|b| \leq 10°$ and hence have width of about $\Delta b \sim 20°$.

There are discontinuities (gaps) in the structures of the proposed Vela overdensity, especially in Fig. 3.12. These originate from our sparse sampling of the Vela and Hydra/Antlia regions, also because the 2dF+AAOmega observations targeted regions with extinction levels below $A_B < 5\,\mathrm{mag}$. As a result, the opaque part of the overdensity, centred around the ZoA $|b| \leq 5°$, is completely unmapped. Consequently, the wall-like structure of this overdensity appears to be discontinuous in the wedge diagrams of Figs.3.9-3.10. The opaque unmapped region in the Vela overdensity, centred around the ZoA $|b| \leq 5°$, is more apparent in Fig.3.12.

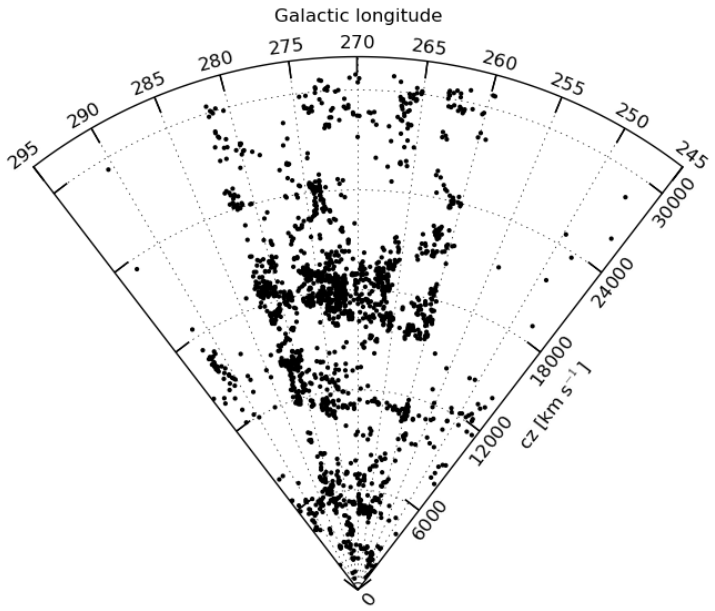

Figure 3.9: Velocity wedge diagram out to velocities of $v = 30000\,\mathrm{km\ s^{-1}}$ in the general proposed VSC longitude range $245° \leq l \leq 295°$ with a width of $\Delta b = 10°$, covering the ZoA within $0° < b < 10.0°$.

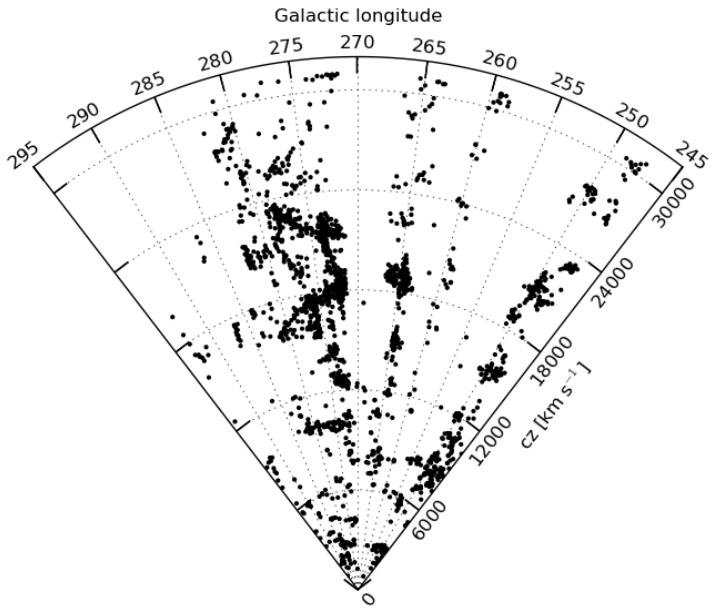

Figure 3.10: Velocity wedge diagram out to velocities of $v = 30000\,\mathrm{km\ s^{-1}}$ in the general proposed VSC longitude range $245° \leq l \leq 295°$ with a width of $\Delta b = 10°$, covering the ZoA within $-10° < b < 0°$.

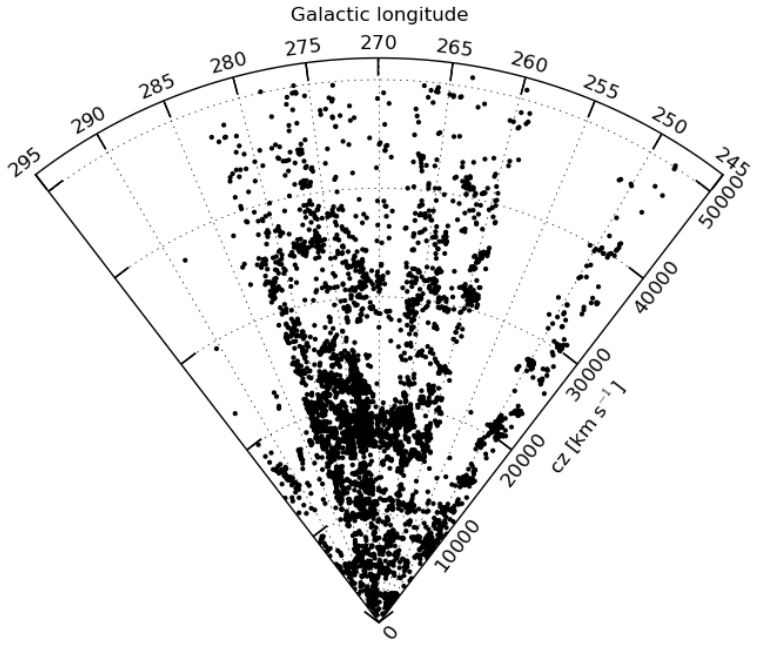

Figure 3.11: Velocity wedge diagram out to velocities of $v = 50000\,\mathrm{km\ s^{-1}}$ in the general proposed VSC longitude range $245° \leq l \leq 295°$ with a width of $\Delta b = 20°$, centred around the ZoA $|b| \leq 10°$.

To compare the prospective VSC with the well studied SSC, we reproduce Figs. 3.13-3.14 from Proust et al. (2006). These figures show wedge diagram out to velocities of $v = 30000\,\mathrm{km\ s^{-1}}$ and $v = 60000\,\mathrm{km\ s^{-1}}$ in the general direction of the SSC, respectively. The SSC fills an extended region of 12 degrees by 30 degrees on-sky, and occupies in velocity space the range from $v \sim 9,000$ km s^{-1} to $v \sim 18,000$ km s^{-1}. This translates to 50×112Mpc on-sky, centred at $v = 14,500$ km s^{-1} (Proust et al. 2006). The structures and the extent of the proposed VSC in wedge diagrams is very similar to that of the SSC. The wall like structure of the prospective VSC at $v \sim 18,000$ km s^{-1} (Fig. 3.8) is comparable to the SSC structures at $v \sim 15,000$ km s^{-1}(Fig.3.13). Further, the overdensity of the galaxies in the proposed VSC at $v \sim 18,000$ km s^{-1} (Fig. 3.11) is approximately as prominent as the overdensity of the galaxies in the SSC at $v \sim 15,000$ km s^{-1}(Fig.3.14). This is a further evidence that the Vela overdensity is likely a massive supercluster.

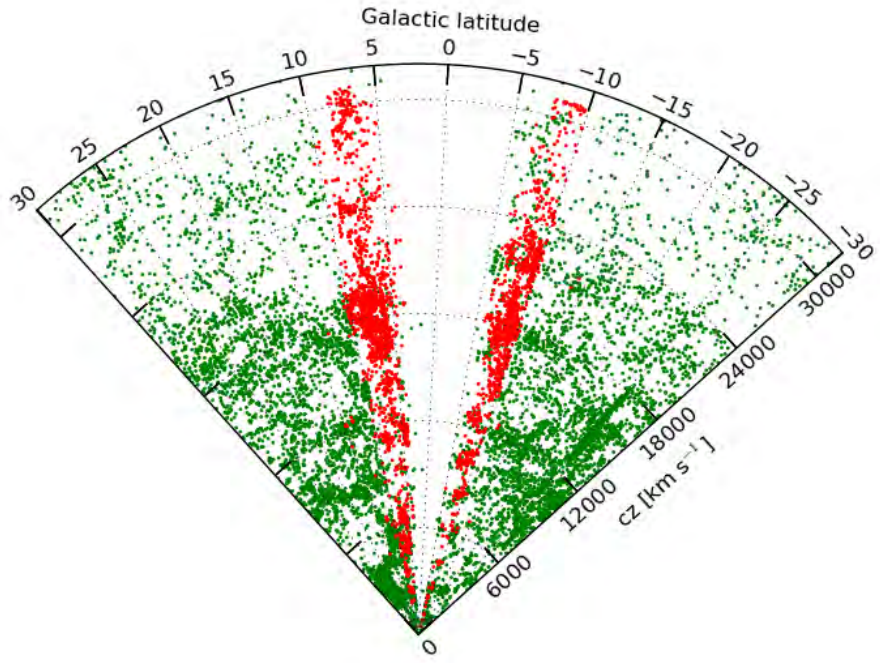

Figure 3.12: Velocity wedge diagram out to velocities of $v = 30000\,\mathrm{km\ s^{-1}}$ in the general proposed VSC longitude range $255° \leq l \leq 285°$ with a width of $\Delta b = 60°$, thus covering the region within $-30.0° < b < 30.0°$. These galaxies are colour-coded according to different redshift sources. Red are the galaxies in the Master Catalogue, while green are the galaxies available in the extragalactic database HYPERLEDA.

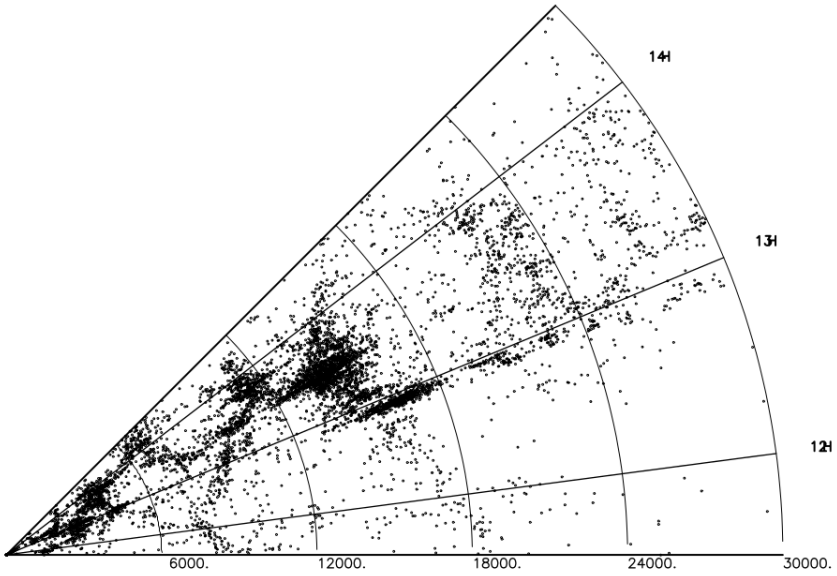

Figure 3.13: Velocity wedge diagram out to velocities of $v = 30,000\,\mathrm{km\ s^{-1}}$ in the direction of the SSC, reproduced from Proust et al. (2006).

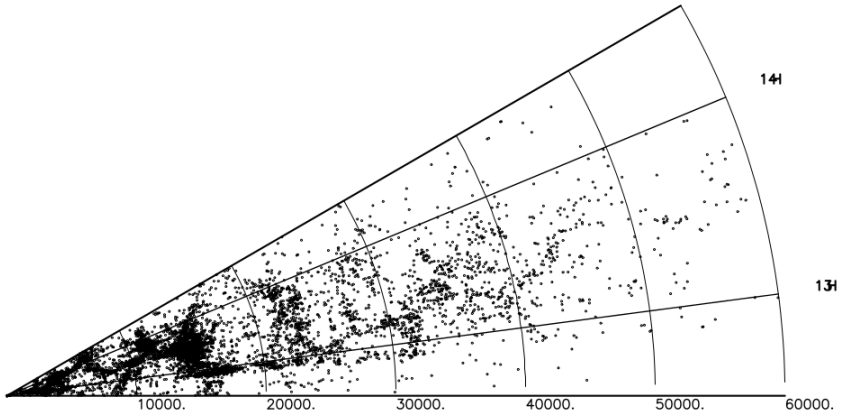

Figure 3.14: Velocity wedge diagram out to velocities of $v = 60,000\,\mathrm{km\ s^{-1}}$ in the direction of the SSC, reproduced from Proust et al. (2006).

3.3 Summary

This chapter discussed the velocity distribution of the galaxies in the direction of the potential VSC, refer to Figs.3.2, 3.3 and 3.4. These figures indicated that the velocity distribution of the galaxies in this candidate supercluster is similar to that of the SSC, based on a full systematic mapping of the SSC (refer to Fig.2 in Proust et al. (2006)), and that this potential supercluster extends over a large area on-sky, straddling the Galactic plane across the ZoA within $|b| \leq 10^{\circ}$. This Chapter also presented the large-scale distribution of the galaxies in the proposed VSC using wedge diagrams, see Figs.3.8-3.11. These figures showed that this candidate supercluster seems to be embedded in a wall like structure that extends over 87 Mpc on-sky. Further, the overdensity of the galaxies in this supercluster at $v \sim 18000$ km s^{-1} (see Fig. 3.11) is approximately as prominent as the overdensity of the galaxies in the SSC at $v \sim 15,000$ km s^{-1} (refer to Fig.3.14). Taken together, we argue that the Vela overdensity appears to be a strong supercluster candidate.

Chapter 4

Cluster Analysis

The main goal of this chapter is to identify the potential galaxy clusters/groups within the proposed Vela Supercluster (VSC). Some authors define a supercluster as a structure that contains at least 3 galaxy clusters (Batiste & Batuski 2013a). Others introduce more restricted criteria to define a supercluster. For example, Araya-Melo et al. (2009) defines a massive supercluster as containing no less than five galaxy clusters with a mass average of $3.6 \times 10^{14}\,\mathrm{M}_{\odot}$ per galaxy cluster. After the identification of the potential galaxy clusters/groups, I estimate the velocity dispersions and the virial masses of these dense regions and compare their richness and velocity dispersions with the galaxy clusters identified within the Shapley Supercluster by Proust et al. (2006). Further, I study the large-scale distribution of the potential galaxy clusters/groups within the proposed VSC using wedge diagrams.

4.1 Potential Galaxy Clusters/Groups Within the Vela Supercluster

In this section, I present two cases of a galaxy cluster candidate and a galaxy group candidate, and describe how I classified these two dense regions into a potential cluster and a galaxy group. As a first step in the identification of the potential galaxy clusters and groups within the proposed VSC, I produce, for all the dense areas in redshift space, a velocity histogram, a velocity distribution as a function of centric distance (in degrees), a M^0_{Ks}-band magnitude count, and a M^0_{BJ}-band magnitude count. Appendix C contains plots for all the dense regions and their classification based on the same criteria described below.

To locate the populous regions within this candidate supercluster, I used two methods. I first started by producing on-sky plots for the galaxies in the direction of the potential VSC in different redshift bands. Using zoomed-in versions, it is easy to examine by eye the agglomerated areas and assess whether we are looking at a cluster/group candidate by taking other criteria into consideration such as presented in Figs. 4.1-4.2. The second method is

by using a nearest neighbour algorithm. This algorithm searches for the galaxies with the highest number of neighbours in velocity space. These neighbours must lie within one Abell radius at that specific redshift from the respective centre. The Abell radius is the typical radius of a galaxy cluster and it equals:

$$R_A = 1.7/z \;\; arcmin \tag{4.1}$$

where z is the redshift of the cluster (Bahcall 1977a). For a typical cluster within the proposed VSC $cz = 18000\,\mathrm{km\ s^{-1}}$, the Abell radius of that cluster equals $R_A \sim 28'$, which translates to a radius of 2 Mpc. The Abell radius is smaller or larger for background or foreground clusters, respectively. In practice, this algorithm searches for dense areas in velocity range out to $v = 35000\,\mathrm{km\ s^{-1}}$ for the galaxies in the direction of the proposed VSC in different velocity slices, $\Delta v = 500\,\mathrm{km\ s^{-1}}$, $\Delta v = 700\,\mathrm{km\ s^{-1}}$ and $\Delta v = 900\,\mathrm{km\ s^{-1}}$. Using different velocity slices ensure that no galaxy agglomeration that lies in the border of one slice shell is unaccounted for. Locating the dense regions using this method is more accurate than using zoomed-in versions and examining the on-sky distribution of the galaxies by eye. However, both methods gave similar results, I will describe these dense regions in the following in more detail.

In general, clusters have a Gaussian velocity histogram with a high peak because of their high galaxy densities, while the galaxy groups have relatively lower peaks (Tully 2015, Woudt et al. 2008, Colless & Dunn 1996). Panel 1 in Figs. 4.1-4.2 illustrates the velocity histogram of two dense areas in the direction of the VSC, namely region 4 and 33, respectively (see Fig. 4.3). From the Gaussian velocity histogram of region 4, see panel 1 in Fig. 4.1, and the high peak of this distribution at $v \sim 18000\,\mathrm{km\ s^{-1}}$ this region is likely a cluster candidate. On the other hand, region 33 is likely a group candidate because of the relatively lower peak and the small width of the semi-Gaussian shape of its velocity distribution, refer to panel 1 in Fig. 4.2. Panel 2 in Figs. 4.1- 4.2 shows the velocity distribution as a function of the cluster/group centric-distance for the same two dense regions, the likely cluster candidate (region 4) and the potential group candidate (region 33), respectively. The red dots are the galaxies that belong to the cluster/group and lie within 1 Abell radius from the chosen centre. The velocity limits for the potential cluster/group membership are taken as 3 times the velocity dispersion σ of the respective candidate around its mean velocity. The blue dots are the galaxies in the background and foreground of the cluster/group.

The on-sky distribution of the galaxies in the clusters/groups gives an indication of the symmetry of the structure. It is a spherical shape in the case of early type clusters, and irregular shape in the case of late type clusters and the galaxy groups (Bahcall 1977b). Panel 5 in Figs. 4.1-4.2 display the on-sky distribution of the galaxies for the potential cluster candidate, and the group candidate, respectively. The red points show the galaxies that are members of the potential cluster/group. These members lies within 1 Abell radius and

within 3σ of the mean velocity of the prospective cluster/group candidate. The black dot represents the optimised cluster/group center. The optimised centre is taken as the densest region of the prospective cluster/group candidate. The blue dots represent the foreground and background surrounding galaxies for which we have redshift measurements, while the green dots represent the foreground and background surrounding galaxies for which we have no redshift measurements. The black circles delimit the AAOmega observation fields, from which the majority of our data originate. The number in these circles correspond to the number of the AAOmega fields. Some of the candidate galaxy clusters/groups lie in the borders of the AAOmega fields which means that these regions are not fully sampled (see Appendix C). For the case of the likely cluster candidate, the galaxies are distributed in a spherical shape indicating a virialized structure, refer to panel 5 of Fig. 4.1, while the galaxies in the group candidate are distributed in an irregular shape as shown in panel 5 of Fig. 4.2.

The Absolute Magnitude Histograms of the Galaxy Clusters/Groups:
Now, I will evaluate the absolute magnitude distribution of the potential clusters/groups candidates using both the isophotal B-band and the K_s-band magnitude available in the Master Catalogue. It is crucial to mention that not all the optical galaxies in the Master Catalogue have counterparts in the 2MASX catalogue and vice versa. This difference will appear when the extinction-corrected absolute B-band magnitude (M^0_{BJ}) and the extinction-corrected absolute K_s-band magnitude (M^0_{Ks}) histograms for the overdense areas are displayed. These histograms do not always contain the same galaxies. The M^0_{BJ} and the M^0_{Ks} magnitude distributions for some dense areas will have homogeneous histogram shapes because most of the galaxies in the optical have counterparts in the infrared, whereas for other dense areas the magnitude histograms will not be homogeneous because not all the optical galaxies have counterparts in the infrared and vice versa. Moreover, the B-band magnitude distribution is more strongly affected by varying foreground extinction than the K_s-band magnitude.

The M^0_{BJ} and the M^0_{Ks} magnitude histograms display the magnitude distribution of the galaxies in the galaxy clusters and the galaxy groups. It gives further insights to the class of the dense regions. For instance, clusters are usually associated with very luminous galaxies like cD-galaxies. On the other hand, only a handful of these luminous galaxies are present in the poor clusters and the galaxy groups. In the following, I use the M^0_{BJ} and the M^0_{Ks} magnitude histograms to study the galaxy clusters/groups candidates in further details. I first calculate the extinction-corrected magnitude in the K_s-band following Riad et al. (2010) optimised approach based on the central surface brightness μ_c, and the extinction-corrected magnitude in the B-band using Cameron (1990) optimised approach in correcting for foreground dust extinction using the following equations,

$$K^0_s = K_s - 0.368E(B-V) - \Delta K_s, \tag{4.2}$$

$$B^0 = B - 4.107E(B-V) - \Delta B, \tag{4.3}$$

where ΔK_s and ΔB are correction factors for the K_s-band and the B-band estimated as in Riad et al. (2010) and Cameron (1990). Then, the absolute magnitude equals

$$M = m^0 - 5log(d_L) - 25 \tag{4.4}$$

where d_L is the luminosity distance of the potential cluster/group candidate determined using the mean velocity of that respective candidate, and a value of $H_0 = 75\,\mathrm{km\ s^{-1}\ Mpc^{-1}}$. m^0 is the extinction-corrected magnitude in the B-band or the K_s-band corresponding to an extinction-corrected absolute isophotal magnitude in the B-band (M^0_{BJ}) or the K_s-band (M^0_{Ks}), respectively.

In addition to the absolute magnitude, I estimate the approximate magnitude completeness limit for the potential galaxy clusters/groups. First, I use equations 4.2 and 4.3 to find the extinction-corrected magnitude. Where the value of $K_s = 13^m.5$, $B = 18^m.5$ (Kraan-Korteweg 2000a), and the average extinction $E(B-V)$ for the cluster/group members are used, a typical extinction value at that region is of the order $E(B-V) \sim 0.2$. Then, I use equation 4.4 to calculate the magnitude completeness limit, where d_L is the luminosity distance measured using the mean velocity (redshift) of the prospective galaxy cluster/group. A typical cluster in the prospective VSC lies at $cz = 18000\,\mathrm{km\ s^{-1}}$, which corresponds to $d_L \sim 240\,\mathrm{Mpc}$.

Further, I use the characteristic absolute magnitude M^* for clusters/groups found in the literature and compare it with the magnitude completeness limit for all the clusters/groups candidates I locate. M^* is the "knee" of the Schechter (1976) luminosity function for the cluster/group. Galaxies fainter than M^* are described by a power law distribution, while galaxies brighter than M^* have a logarithmic density distribution. According to Gardner et al. (1997), the value of $M^* = -19^m.7 \pm 0.1$ for the cluster B-band luminosity function. For the cluster K_s-band luminosity function, the value of $M^* = -23^m.1 \pm 0.2$, see for example Lin et al. (2004). On the other hand, the value of $M^* = -19^m.5$ for the group B-band luminosity function (Zepf et al. 1997), and the value of $M^* = -22^m.8$ for the group K_s-band luminosity function (Miles et al. 2006). Panels 3 and 4 in Figs. 4.1-4.2 show the M^0_{BJ} and the M^0_{Ks} magnitude histograms for the cluster candidate and the galaxy group candidate, respectively. As discussed previously, clusters have more luminous galaxies than galaxy groups. In comparison, the M^0_{BJ} magnitude histogram of the cluster candidate in panel 3 of Fig. 4.1, there are many galaxies with $M^0_{Bj} < -20$, whereas the M^0_{BJ} magnitude histogram of the group candidate in panel 3 of Fig. 4.2, fewer galaxies have $M^0_{Bj} < -20$.

Furthermore, I use the virial theorem, given by the following equation, to calculate the mass of the clusters/groups candidates (Fig. 4.3), see for example Zwicky (1957), Bahcall

(1977c), Smith (1936),

$$M \sim \frac{5\sigma^2 R}{G}, \tag{4.5}$$

where σ is the velocity dispersion of the cluster/group members. The dispersion velocity is measured for the red dots only (refer to panel 2 in Figs. 4.1-4.2), i.e., the galaxies that are members of the potential cluster/group. These members lies within 1 Abell radius and within 3σ of the mean velocity of the prospective cluster/group candidate. G is the gravitational constant ($G = 4.302 \times 10^{-3}\,\mathrm{pc M_\odot^{-1} (km\ s^{-1})^2}$, and R is the Abell radius at the mean redshift of the cluster/group, for a typical cluster/group within the proposed VSC $R = 2\,\mathrm{Mpc}$.

VC04: $(l, b) = (272.27°, -8.96°)$

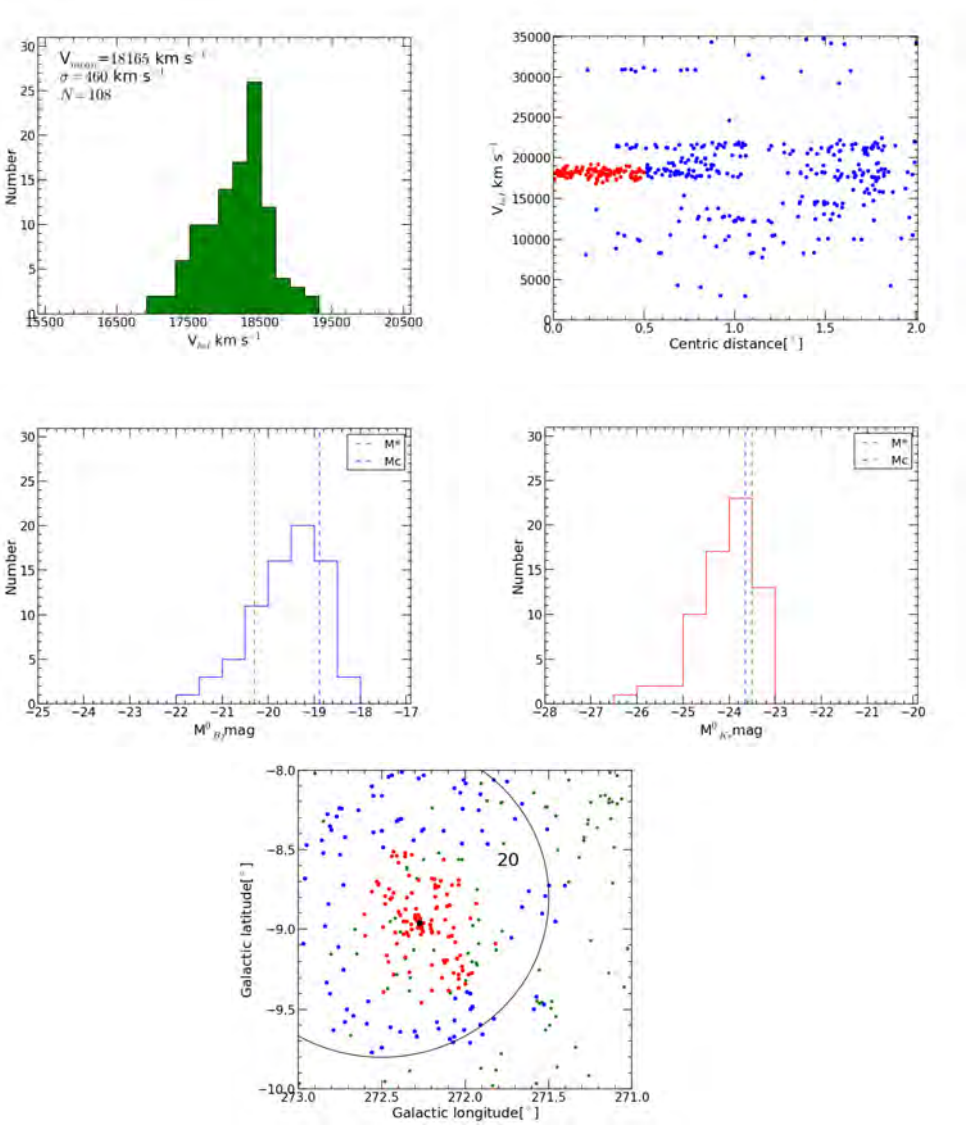

Figure 4.1: This area is a strong cluster candidate and has a mass of $4.91 \times 10^{14}\,\mathrm{M}_{\odot}$. This cluster is the densest cluster within the proposed VSC identified up to date. Though it has a small mass compared to the other cluster candidates, this is due to the small velocity dispersion of its members. It seems to be virialized and most likely in a state of equilibrium (very early cluster). The black circle in panel 5 delimits the AAOmega observation field.

VG20: $(l, b) = (275.91°, 9.33°)$

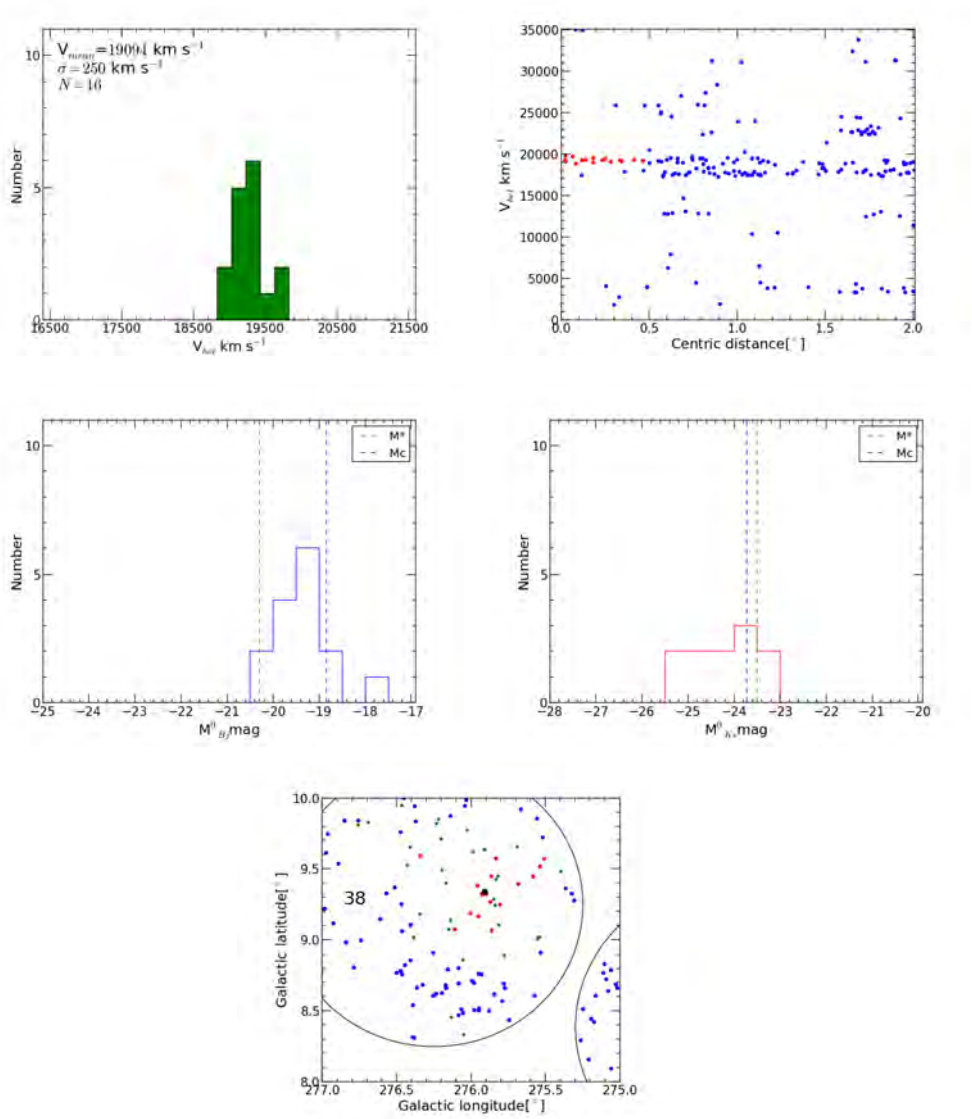

Figure 4.2: From the luminosity function, panel 3 and 4, this region is a strong group candidate. It has a high velocity histogram peak (panel 1), and a very dense centre , almost 90% of the members lie within 400 km s^{-1} from the center (panel 2). This potential galaxy group has a mass of $1.45 \times 10^{14}\,M_{\odot}$. The black circles in panel 5 delimit the AAOmega observation fields.

The locations of the candidate galaxy clusters/groups are shown in Fig. 4.3. This figure encapsulates the galaxies with $0 < v < 35000\,\mathrm{km\ s^{-1}}$. These galaxies are colour-coded according to different velocity slices. Black are galaxies within velocity range $0 < v < 15000\,\mathrm{km\ s^{-1}}$, red are galaxies within velocity range $15000 < v < 25000\,\mathrm{km\ s^{-1}}$ (the approximate range of the VSC), and green are galaxies within velocity range $25000 < v < 35000\,\mathrm{km\ s^{-1}}$. The potential cluster candidates are marked with the blue circles, while the potential group candidates are marked with the black circles. The labels of the candidates in Fig. 4.3, the positions, the mean velocities (V_m) in km $\mathrm{s^{-1}}$, the number of members, the velocity dispersions (σ) in km $\mathrm{s^{-1}}$, and the masses of these candidates are presented in Tables 4.1-4.2. The galaxy clusters/groups are sorted by increasing Right Ascension.

There are 13 potential galaxy clusters candidates, and 22 potential galaxy groups in the direction of the proposed VSC identified up to date. Out of the 13 potential clusters, 8 clusters lie below the Galactic plane, whereas the remaining 5 clusters are located above the Galactic plane. Eight of these potential clusters are strong candidates, while the remaining five potential clusters, namely VC03,VC06, VC07, VC09 and VC13, are weak candidates. However, these weak cluster candidates are very under sampled and lie close to the edge of the AAOmega fields (see Appendix C). On the other hand, 13 out of the 22 potential group candidates lie above the Galactic plane. Moreover, thirteen of the galaxy groups are strong group candidates, while the remaining 9 groups are weak candidates. Out of the nine weak candidates, six are undersampled candidates, namely VG01, VG02, VG07, VG13, VG16 and VG17. Five of the undersampled potential groups lie close to the edge of the AAOmega field. The sixth weak group candidate (VG17) was observed using SALT, which is known to have small FOV $8' \times 8'$ on the sky, refer to Appendix C.

Based on a full systematic mapping of the Shapley Supercluster (SSC), Proust et al. (2006) identified 33 galaxy clusters within the SSC velocity range from $13000 - 18000\,\mathrm{km\ s^{-1}}$. The SSC clusters are comparable to the 13 clusters located within the proposed VSC both in richness and velocity dispersion (refer to Table 4 in Proust et al. 2006). The vast majority of the SSC clusters have between $20 - 60$ members and only a handful of these clusters have more than 90 members. The same applies to the clusters within the VSC, where most of the clusters have comparable richness to the clusters within the SSC, i.e. have number of members in the range from $20 - 60$. However, only one cluster in the prospective VSC contains more than 90 members. This resulted from our sparse sampling of the Vela and Hydra/Antlia regions, and because the 2dF+AAOmega observations targeted regions with extinction levels below $A_B < 5\,\mathrm{mag}$. Consequently, we only sampled the tip of the iceberg of the true richness of the potential clusters/groups within the potential VSC. In terms of velocity dispersion, the majority of the galaxy clusters within both the SSC and the proposed VSC have comparable velocity dispersions, in the range from $400 - 800\,\mathrm{km\ s^{-1}}$.

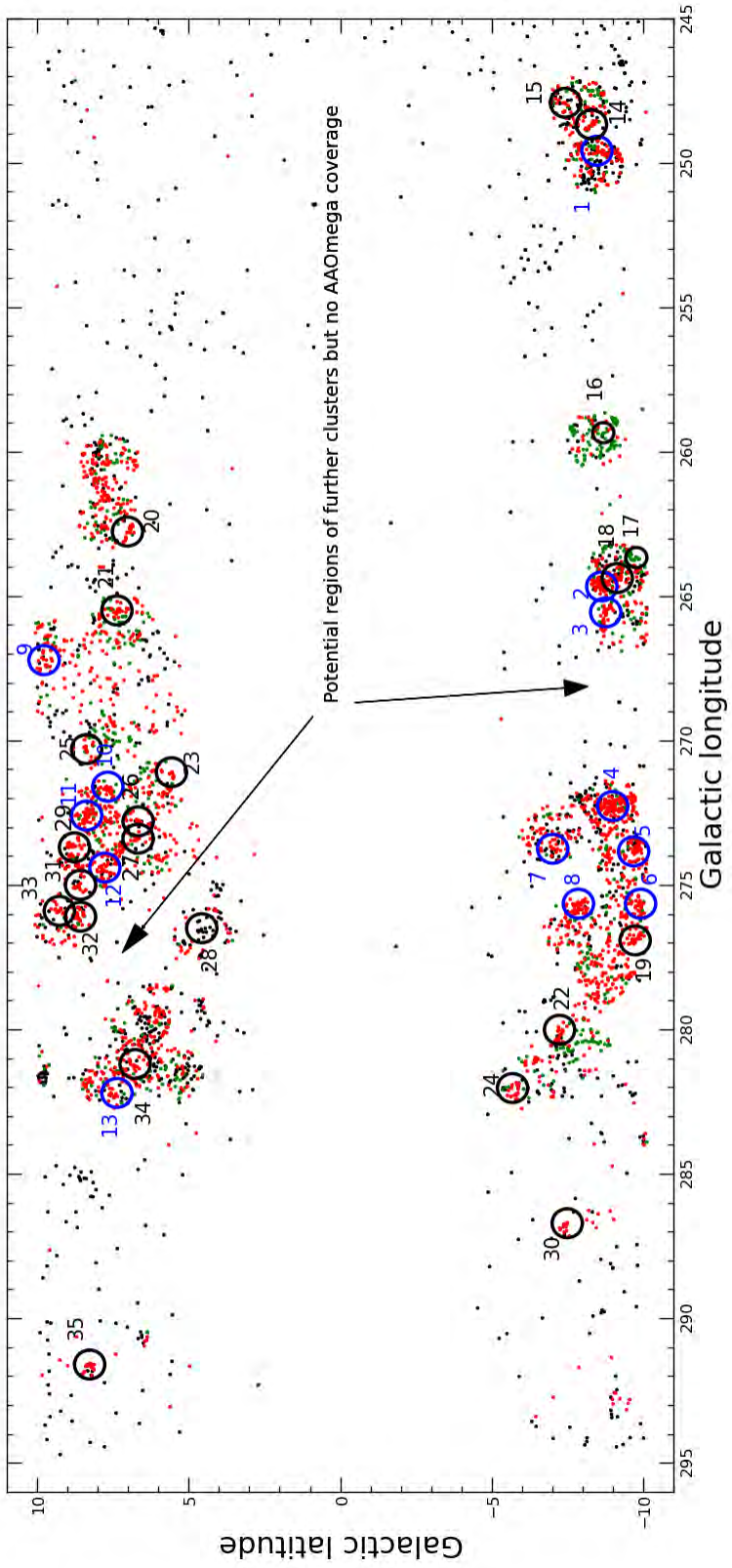

Figure 4.3: Potential candidate galaxy clusters/groups within the proposed VSC. This figure encapsulates the galaxies with velocities out to $v = 35000\,\mathrm{km\ s^{-1}}$. These galaxies are colour-coded according to different velocity slices. Black are galaxies within velocity range $0 < v < 15000\,\mathrm{km\ s^{-1}}$, red are galaxies within velocity range $15000 < v < 25000\,\mathrm{km\ s^{-1}}$, and green are galaxies within velocity range $25000 < v < 35000\,\mathrm{km\ s^{-1}}$. The galaxy clusters are marked with blue circles, while the galaxy groups are marked with the black circles. There are 13 potential galaxy clusters and 22 potential galaxy groups identified up to date.

Table 4.1: Some statistics for the galaxy clusters candidates within the prospective VSC.

Region	Name	Centre (α, δ) (° , °)	Centre (l, b) (° , °)	N	V_m km s^{-1}	σ km s^{-1}	Mass 10^{14} M$_\odot$	Comments
1	VC01	112.77,-36.34	249.59, -8.44	29	21191	591	8	Strong candidate
2	VC02	122.69, -49.39	264.67, -8.60	50	18972	657	10	Strong candidate
3	VC03	123.25,-50.20	265.56, -8.73	25	18981	334	3	Weak candidate
4	VC04	129.14,-55.81	272.27, -8.96	108	18165	460	5	Strong candidate
5	VC05	129.78,-57.47	273.84, -9.65	39	21172	552	7	Strong candidate
6	VC06	131.49,-59.04	275.65, -9.88	21	16132	468	5	Weak candidate
7	VC07	133.52,-55.76	273.75, -6.98	24	22219	729	12	Weak candidate
8	VC08	134.54,-57.75	275.65, -7.83	38	17363	656	10	Strong candidate
9	VC09	144.77,-39.37	267.22, 9.80	22	18672	350	2	Weak candidate
10	VC10	147.38,-43.84	271.67, 7.71	29	18190	618	9	Strong candidate
11	VC11	149.0,-43.89	272.62, 8.41	57	17876	712	12	Strong candidate
12	VC12	150.60,-45.46	274.49, 7.87	28	18524	589	8	Strong candidate
13	VC13	159.82,-50.04	282.25, 7.45	16	18675	665	10	Weak candidate

Table 4.2: Some statistics for the galaxy groups candidates within the prospective VSC.

Region	Name	Centre (α, δ) (° , °)	Centre (l, b) (° , °)	N	V_m km s^{-1}	σ km s^{-1}	Mass 10^{14} M$_\odot$	Comments
14	VG01	112.44,-35.46	248.68, -8.26	13	15824	567	7	Weak candidate
15	VG02	112.96,-34.40	247.93, -7.40	8	23110	134	0.4	Weak candidate
16	VG03	118.64,-44.91	259.35, -8.65	10	31194	102	0.2	Weak candidate
17	VG04	120.41,-49.14	263.67, -9.74	11	31865	828	16	Strong candidate
18	VG05	121.79,-49.42	264.38, -9.11	26	15114	488	5	Strong candidate
19	VG06	133.29,-59.91	276.92, -9.70	15	22729	330	2	Strong candidate
20	VG07	138.10,-38.25	262.69, 6.94	12	15834	269	1	Weak candidate
21	VG08	141.12,-39.97	265.55, 7.43	16	16196	329	3	Strong candidate
22	VG09	141.15,-60.51	280.01, -7.20	10	21022	203	1	Weak candidate
23	VG10	144.85,-45.07	271.10, 5.60	11	16525	269	2	Weak candidate
24	VG11	146.29,-60.73	282.03, -5.65	19	20922	372	3	Strong candidate
25	VG12	146.59,-42.41	270.30, 8.43	17	18429	635	9	Strong candidate
26	VG13	147.74,-45.36	272.85, 6.70	9	17280	271	2	Weak candidate
27	VG14	148.40,-45.70	273.42, 6.73	14	19750	493	6	Strong candidate
28	VG15	150.07,-49.27	276.53, 4.61	21	11639	356	3	Strong candidate
29	VG16	150.56,-44.20	273.71, 8.85	12	17605	401	4	Weak candidate
30	VG17	151.85,-65.03	286.71, -7.46	10	16932	405	4	Weak candidate
31	VG18	151.87,-45.12	275.01, 8.68	17	17500	625	9	Strong candidate
32	VG19	153.21,-45.77	276.17, 8.69	30	18428	861	15	Strong candidate
33	VG20	153.43,-45.09	275.91, 9.33	16	19094	250	1	Strong candidate
34	VG21	158.05,-50.06	281.27, 6.86	15	18719	377	3	Strong candidate
35	VG22	174.16,-52.86	291.65, 8.36	15	15993	304	2	Strong candidate

4.2 Structures of the Galaxy Clusters/Groups in Velocity Wedges

This section presents the large-scale distribution of the potential galaxy clusters/groups within the proposed VSC using wedge diagrams. Figures 4.4-4.5 and 4.6 show wedge diagrams out to velocities of $v = 30000\,\mathrm{km\ s^{-1}}$ in the general VSC region, covering longitude range $245^\circ \leq l \leq 295^\circ$. Figure 4.4 encapsulates the galaxies within the Galactic plane, hence covering the ZoA within $|b| \leq 10^\circ$. Figure 4.5 includes all the galaxies above the Galactic plane with a width of $\Delta b = 10^\circ$, thus covering the ZoA within $0^\circ < b < 10.0^\circ$. Figure 4.6 encloses all the galaxies below the Galactic plane with a width of $\Delta b = 10^\circ$, consequently covering the ZoA within $-10^\circ < b < 0^\circ$. The red dots are the galaxies that belong to the potential galaxy clusters or the potential galaxy groups. Based on Fig. 4.4, the proposed VSC shows up as a prominent wall-like structure. The galaxy clusters/groups (red dots) seem to be implanted in the wall-like structure of this supercluster. This is expected because galaxy clusters/groups mostly favour to lie within wall-like structures which have higher density than filamentary structures (Pimbblet et al. 2005, Doroshkevich et al. 2004).

The wall-like structure of the prospective VSC consists of two walls (as discussed in chapter three), the main wall (wall one) at $v \sim 18000\,\mathrm{km\ s^{-1}}$ and a smaller one (wall two) at slightly higher velocity. Tracers of wall one appear both above and below the Galactic plane (see Figs. 4.5-4.6). The second wall is present only below the plane, see Fig. 4.6. The galaxy clusters/groups (red dots) are embedded in both walls (one and two), but it is more prominent in wall one. This is expected, because wall one is the larger wall. It extends about $\sim 87\,\mathrm{Mpc}$ on the sky. Further, the galaxy clusters/groups seems to be equally distributed in either side of the Galactic plane. The discontinuities (gaps) in the wall-like structure present in the wedge diagrams are not an indication of discontinuities in this wall-like structures. These gaps originate from our sparse sampling of the Vela and Hydra/Antlia regions, and also because the 2dF+AAOmega observations targeted regions with extinction levels below $A_B < 5\,\mathrm{mag}$.

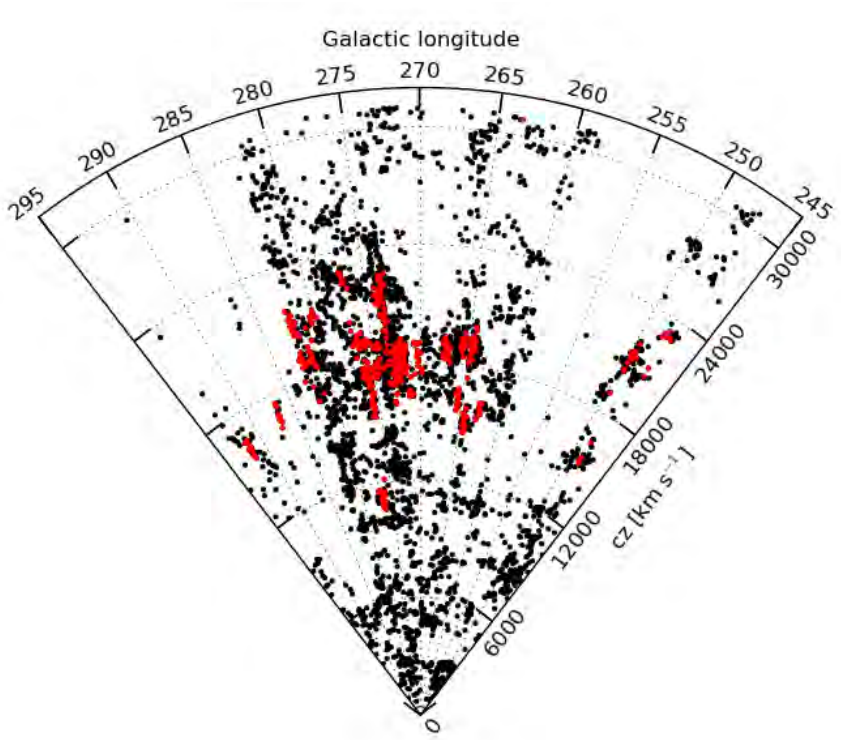

Figure 4.4: Velocity wedge diagram out to velocities of $v = 30000\,\mathrm{km\ s^{-1}}$ in the general proposed VSC longitude range $245° \leq l \leq 295°$ with a width of $\Delta b = 20°$, centred around the ZoA $|b| \leq 10°$. The red dots are the galaxies that belong to the potential galaxy clusters/groups.

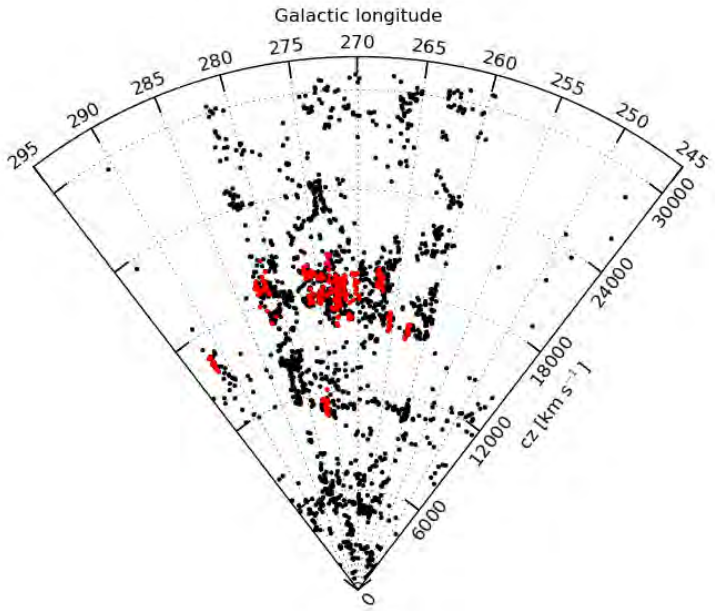

Figure 4.5: Velocity wedge diagram out to velocities of $v = 30000\,\mathrm{km\ s^{-1}}$ in the general proposed VSC longitude range $245° \leq l \leq 295°$ with a width of $\Delta b = 10°$, covering the ZoA within $0° < b < 10.0°$. The red dots are the galaxies that belong to the potential galaxy clusters/groups.

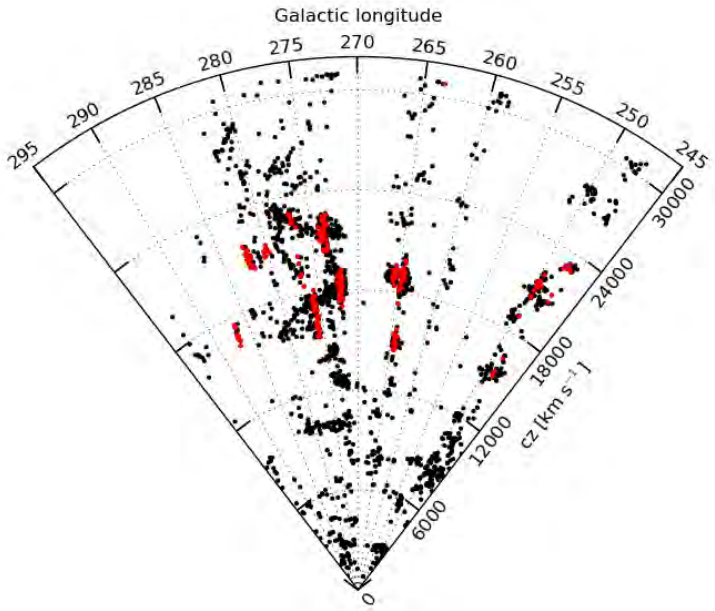

Figure 4.6: Velocity wedge diagram out to velocities of $v = 30000\,\mathrm{km\ s^{-1}}$ in the general proposed VSC longitude range $245° \leq l \leq 295°$ with a width of $\Delta b = 10°$, covering the ZoA within $-10° < b < 0°$. The red dots are the galaxies that belong to the potential galaxy clusters/groups.

4.3 Summary

In this chapter, I discussed the two methods used to identify the potential galaxy clusters/groups within the proposed VSC. In total, there are 13 potential galaxy clusters, and 22 potential galaxy groups within this supercluster, refer to Fig. 4.3 and Tables 4.1-4.2. The potential galaxy clusters identified in this supercluster are comparable to the galaxy clusters within the Shapley Supercluster, both in richness and velocity dispersion (refer to Table 4 in Proust et al. 2006). This strongly suggests that the proposed VSC is a massive supercluster. Further evidence for this assumption is based on the velocity distribution and the wedge diagrams for the galaxies in the direction of the potential VSC (see Figs. 3.2 and 3.8 discussed in the previous chapter). A comparison between these figures and similar figures for the galaxies in the direction of the Shapley Supercluster, see Figs. 1.8-3.13, showed that the two superclusters are comparable to each other. This chapter also presented the large-scale distribution of the galaxy clusters/groups within the proposed VSC in wedge diagrams (see Figs. 4.4, 4.5 and 4.6). These figures show that the galaxy clusters/groups are embedded in the wall-like structure of this supercluster. This is a typical morphology for galaxy clusters/groups, commonly these dense regions favour to lie within wall-like structures (Pimbblet et al. 2005, Doroshkevich et al. 2004).

Chapter 5

Photometric Redshifts

The main purpose of this chapter is to study the extent and the structures of the Vela Supercluster (VSC) and its connection to the neighbouring large-scale structures, using both spectroscopic and photometric redshifts. I extracted 41,401 spectroscopic redshifts for the galaxies in the direction of both the VSC and the SSC from the Master Catalogue and the 6dF Galaxy Survey (6dFGS). We further asked Dr Maciej Bilicki to estimate the photometric redshifts for the galaxies in our source catalogues (see chapter 2) using the same approach he followed in Bilicki et al. (2014). I compiled the estimated photometric redshifts with other photometric redshifts in the direction of both the VSC and the SSC available in the 2MPZ catalogue (Bilicki et al. 2014). A total of 201,846 photometric redshifts were extracted.

5.1 Photometric Redshifts

For a better understanding of the true structures and the extent of the VSC, we need as many redshifts as possible for the galaxies within ($240^\circ \lesssim l \lesssim 295^\circ, |b| \lesssim 15^\circ$). Unfortunately, the VSC lies within the ZoA, where the dust of the Milky Way makes obtaining spectroscopic redshifts a very onerous task. In the Master Catalogue we have science quality redshifts for 5,190 galaxies within ($245^\circ \lesssim l \lesssim 295^\circ, |b| \lesssim 10^\circ$). This is only 12% of the galaxies in the direction of the VSC available in the 2MASS and the optical source catalogues (Kraan-Korteweg 2000a, von Maltitz 2012). This is not enough to draw firm conclusions about the scope of this supercluster. Consequently, we supplement the redshifts samples in the Master Catalogue with photometric redshifts. Even though the photometric redshifts are not very accurate, it is very useful for our study objectives.

There are many techniques to derive the photometric redshifts. For instance, it is possible to establish the relation between the photometry and the redshifts using samples of galaxies with known spectroscopic redshifts, the training set, and exploit this relation to estimate the unknown redshifts. This method usually involves a training software, responsible

for establishing the relation between the photometry and the known redshifts and applying this relation to find the unknown redshifts for the rest of the samples. One of these software is the Artificial Neural Network (ANN$_z$) package (Firth et al. 2003, Collister & Lahav 2004). This package is free and available on-line*. The measured photometric redshifts are very approximate, with typical accuracy of $\sigma_z \sim 0.015$ (Bilicki et al. 2014). Nonetheless, for studying large sample of galaxies, i.e. superclusters, these measurements are applicable especially because no precise spectroscopic measurements are required.

Recently, our collaborators used the ANN$_z$ to estimate photometric redshifts for one million galaxies built from the 2MASS XSC, WISE, and SuperCOSMOS sky survey (Bilicki et al. 2014). This yielded in the generation of one of the largest 3D catalogues, the 2MASS Photometric Redshift catalogue (2MPZ). The photometric redshifts in this catalogue have an accuracy of $\sigma_z \sim 0.015$. The training spectroscopic redshifts sets used to derive the 2MPZ photometric redshifts are comprised from the Sloan Digital Sky Survey, 6dFGS, and 2dFGRS. We asked Dr Maciej Bilicki to kindly derive the photometric redshifts for the galaxies in our source catalogues using the ANN$_z$. As discussed in chapter 2, the source catalogue originates from two deep optical surveys in the ZoA in the Hydra/Antlia and Vela regions (Kraan-Korteweg 2000a, von Maltitz 2012), and the near infrared 2MASS XSC (Jarrett et al. 2000a, Skrutskie et al. 2006). A total of 44,178 galaxies in our survey area ($240^\circ \lesssim l \lesssim 295^\circ, |b| \lesssim 15^\circ$) are available in these catalogues. Of these galaxies 4535 are optical galaxies with no counterparts in the 2MASS XSC, 3054 are optical galaxies with counterparts in the 2MASS XSC, and the remaining 36,589 galaxies belong to the 2MASS XSC with no optical counterparts.

As mentioned above, the derivation of photometric redshifts requires a set of training redshifts. We already have the spectroscopic redshifts in hand, the Master Catalogue of redshifts. However, only the galaxies that are listed in the 2MASS XSC will be used. Since the NIR photometry of the galaxies (JHK_s magnitudes) is essential in training the ANN$_z$ algorithm. In total, the Master Catalogue contains 5,190 science quality redshifts. Of these galaxies 1560 are optical galaxies with no counterparts in the the 2MASS XSC, which had to be excluded from the training set. The remaining 3622 galaxies have NIR photometry and represent part of the training set. In addition to the galaxies in the Master catalogue, spectroscopic redshifts from the 6dF Galaxy Survey (Jones et al. 2009) and the 2MASS Redshift Survey (Huchra et al. 2012) were supplemented to our training sample. A total of 7100 spectroscopic redshifts within ($240^\circ \lesssim l \lesssim 295^\circ, |b| \lesssim 15^\circ$) were used as a training set for the ANN$_z$ algorithm.

Although the near-infrared band is less affected by the foreground dust extinction of the Milky Way, I prepared the extinction-corrected JHK_s magnitudes, and the extinction-corrected isophotal radii r_{k20} for the galaxies in our training sets that originate from the

*http://www.homepages.ucl.ac.uk/ ucapola/annz.html

Master Catalogue. The remaining supplemental spectroscopic redshifts sets have the JHK_s magnitudes and the isophotal radii r_{k20} already corrected as those have been used as part of the 2MPZ training set. I followed the optimised approach of Riad et al. (2010) based on the central surface brightness μ_c to correct for foreground dust extinction. Dr Bilicki used this data as well as the WISE mid-infrared photometry for our training sample to estimate the photometric redshifts for the galaxies in our source catalogues. A total of 36,012 photometric redshifts within our survey area ($240^\circ \lesssim l \lesssim 295^\circ, |b| \lesssim 15^\circ$) were estimated.

5.2 Photometric Redshifts Reliability

To assess the reliability of the photometric redshifts, I compare the galaxies that have both spectroscopic redshifts and photometric redshifts. A total of 6,523 galaxies were found in the range $z \lesssim 0.27$. The redshift error in the crossmatched galaxies has rms of $\sigma_z \sim 0.010$, after excluding the most extreme outlier galaxies ($\sim 3\%$). Figure 5.1 presents these crossmatched galaxies, the red dashed line is the line of equality between the spectroscopic redshifts z_{spec} and the photometric redshifts z_{phot}. The lower panel of Fig. 5.1 shows the redshifts offset $\Delta = z_{spec} - z_{phot}$ versus z_{spec} for the same sample of galaxies. The outlier galaxies have offset $\Delta > 0.05$ and rms of $\sigma_z \sim 0.032$, these galaxies are presented by the green dots in Fig 5.1. It is important to note that the galaxies within the redshift range of the VSC have the smallest σ_z and the lowest systematic offset.

The large errors in the photometric redshifts have significant implications on the distribution of the galaxies in overdense regions. The high peaks of the overdense areas are considerably washed-out when the photometric redshifts are introduced. To emphasis this, Fig. 5.2 shows the velocity distribution of the galaxies in the direction of the VSC using spectroscopic redshifts (red curve), photometric redshifts (blue), and best redshifts measurements available (cyan). The best redshift measurement *zbest* equals z_{spec} (if available) or z_{phot} (if no z_{spec} is available). In this figure, the VSC overdensity is very prominent at $V_{hel} \sim 18000\,\mathrm{km\ s^{-1}}$ in spectroscopic redshifts space (red line), but this overdensity is washed-out when only photometric redshifts are employed (the blue and the cyan lines). Bearing in mind all the above drawbacks, I will use the photometric redshifts in the following section for further analysis of the VSC.

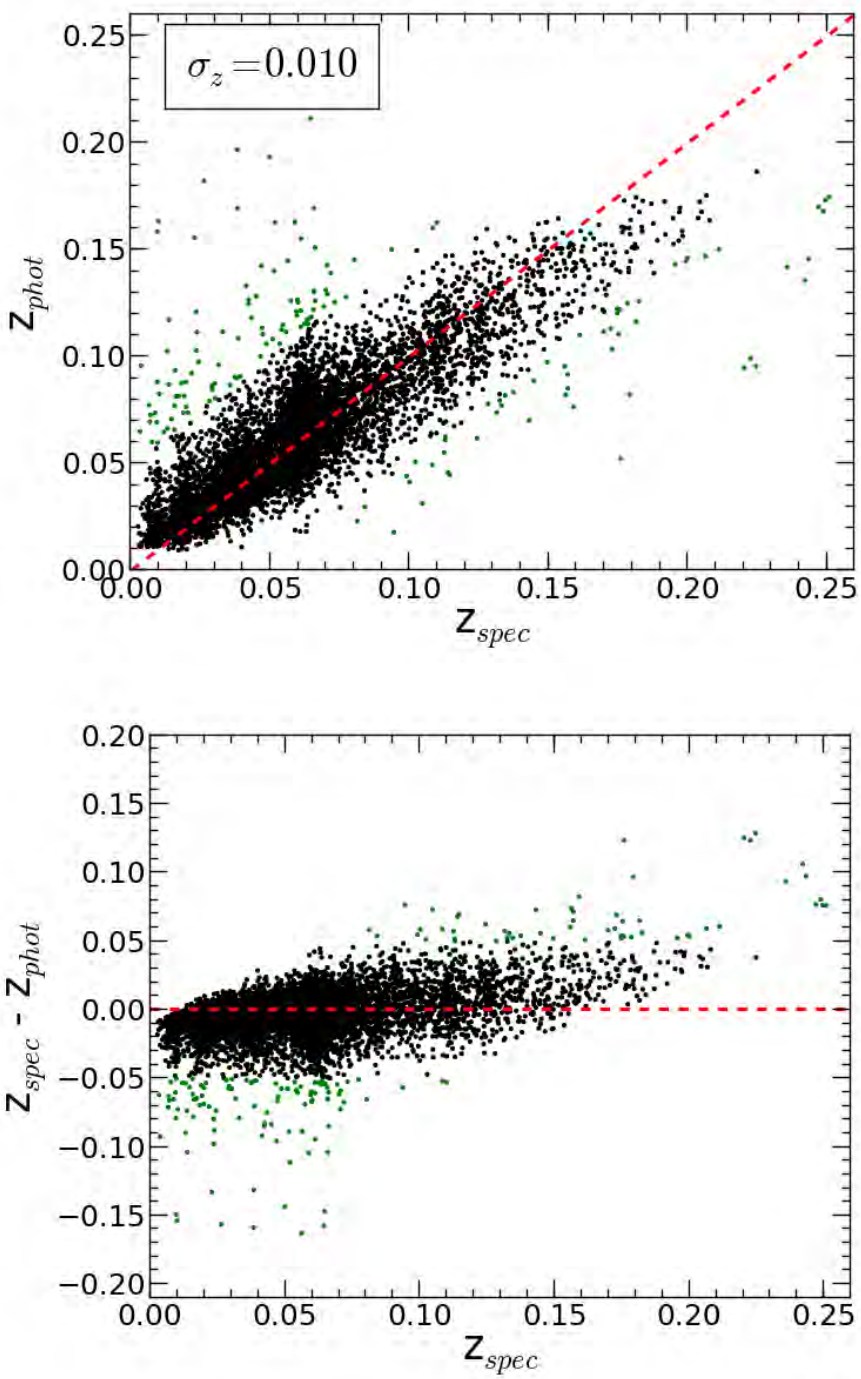

Figure 5.1: Comparsion between the spectroscopic and photometric redshifts for the cross-matched galaxies in the direction of the VSC. The green dots represent the outlier galaxies ($\sim 3\%$). The red dashed line is the line of equality between z_{spec} and z_{phot}. The lower panel shows the redshift offset $\Delta = z_{spec} - z_{phot}$ versus z_{spec} for the same galaxies.

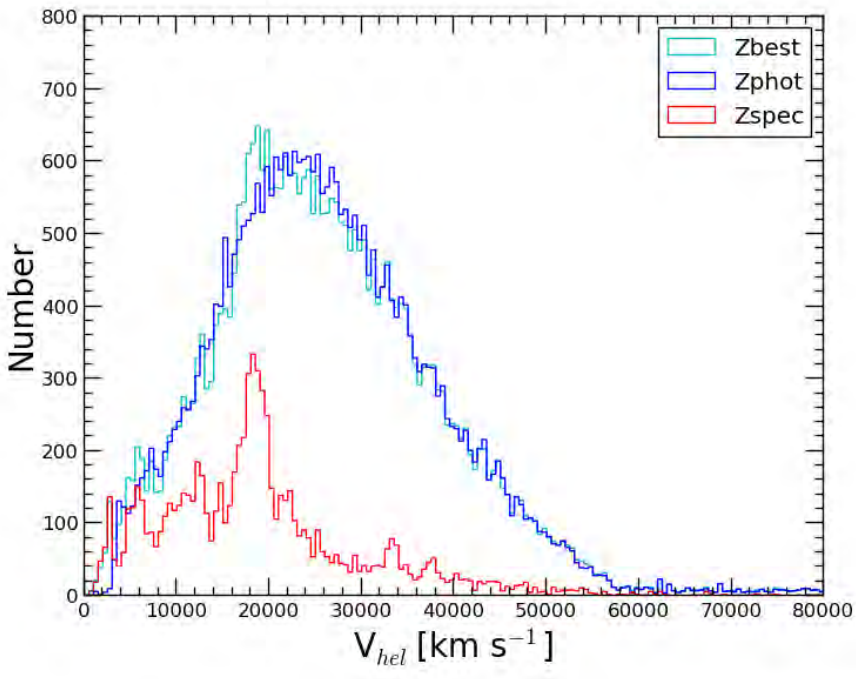

Figure 5.2: The redshift distribution of the galaxies in the direction of the VSC using spectroscopic redshifts (red curve), photometric redshifts (blue), and best redshifts measurements available (cyan). The best redshift measurement equals z_{spec} if available, otherwise equals z_{phot}.

5.3 The Distribution of the Vela Supercluster in Photometric Redshifts Space

In this section, I study the extent of the VSC and its connection to the adjacent large-scale structures in both spectroscopic and photometric redshifts. I added to the spectroscopic redshifts available in the Master Catalogue other spectroscopic redshifts extracted from the 6dF Galaxy Survey (6dFGS) within the range ($240^\circ \lesssim l \lesssim 330^\circ, |b| \lesssim 45^\circ$). A total of $41,401$ spectroscopic redshifts are available in this list. Further, I combined the photometric redshifts estimated by Dr Bilicki for the galaxies in our source catalogues to other photometric redshifts extracted from the 2MPZ catalogue (Bilicki et al. 2014) within the range ($240^\circ \lesssim l \lesssim 330^\circ, |b| \lesssim 45^\circ$). A total of $201,846$ photometric redshifts are available in this list.

The structures of the VSC and the SSC can be studied from the on-sky distribution of the galaxies in different redshift slices, through which the large-scale structures can easily be identified. Figure 5.3 presents the on-sky distribution of the galaxies in the direction of the VSC and the SSC within ($240^\circ \lesssim l \lesssim 330^\circ, |b| \lesssim 45^\circ$) using spectroscopic redshifts. These galaxies are colour-coded according to different redshifts: blue are the galaxies within redshift range $0.04 < z < 0.05$, black within $0.05 < z < 0.06$, red within $0.06 < z < 0.07$, and magenta within $0.07 < z < 0.08$. From this figure the SSC is centred at $(315^\circ, 30^\circ)$, and extends about $12^\circ \times 30^\circ$ on-sky (Proust et al. 2006). At $cz = 14,500\,\mathrm{km\ s^{-1}}$, the extent of the SSC translates to $50 \times 112\,\mathrm{Mpc}$ on-sky. On the other hand, the VSC seems to occupy the region from $l = 262^\circ - 282^\circ$. Assuming that the VSC straddles the Galactic plane, this corresponds to a very broad and extremely massive extended object of size of at least 20 degrees both in Galactic longitude and Galactic latitude. At $cz = 18,000\,\mathrm{km\ s^{-1}}$, the extent of the VSC corresponds to $87 \times 87\,\mathrm{Mpc}$ on-sky.

I further use the photometric redshifts to explore the possibility of a connection between the VSC and the adjacent large-scale structures. Figure 5.4 presents the on-sky distribution of the galaxies in the direction of the VSC and the SSC within the range ($240^\circ \lesssim l \lesssim 330^\circ, |b| \lesssim 45^\circ$) using photometric redshifts. These galaxies are colour-coded similarly to Fig. 5.3. The VSC appears to be more extended than noted previously from the on-sky distribution of spectroscopic redshifts. It extends from $l = 262^\circ - 292^\circ$ above the Galactic plane and from $l = 262^\circ - 282^\circ$ below the Galactic plane. Further, the gap in Galactic latitude caused by the opaque part of the Zone of Avoidance is reduced. This provides hints that the VSC may likely be continuous across the Galactic plane and that it is more extended than $87 \times 87\,\mathrm{Mpc}$ on-sky.

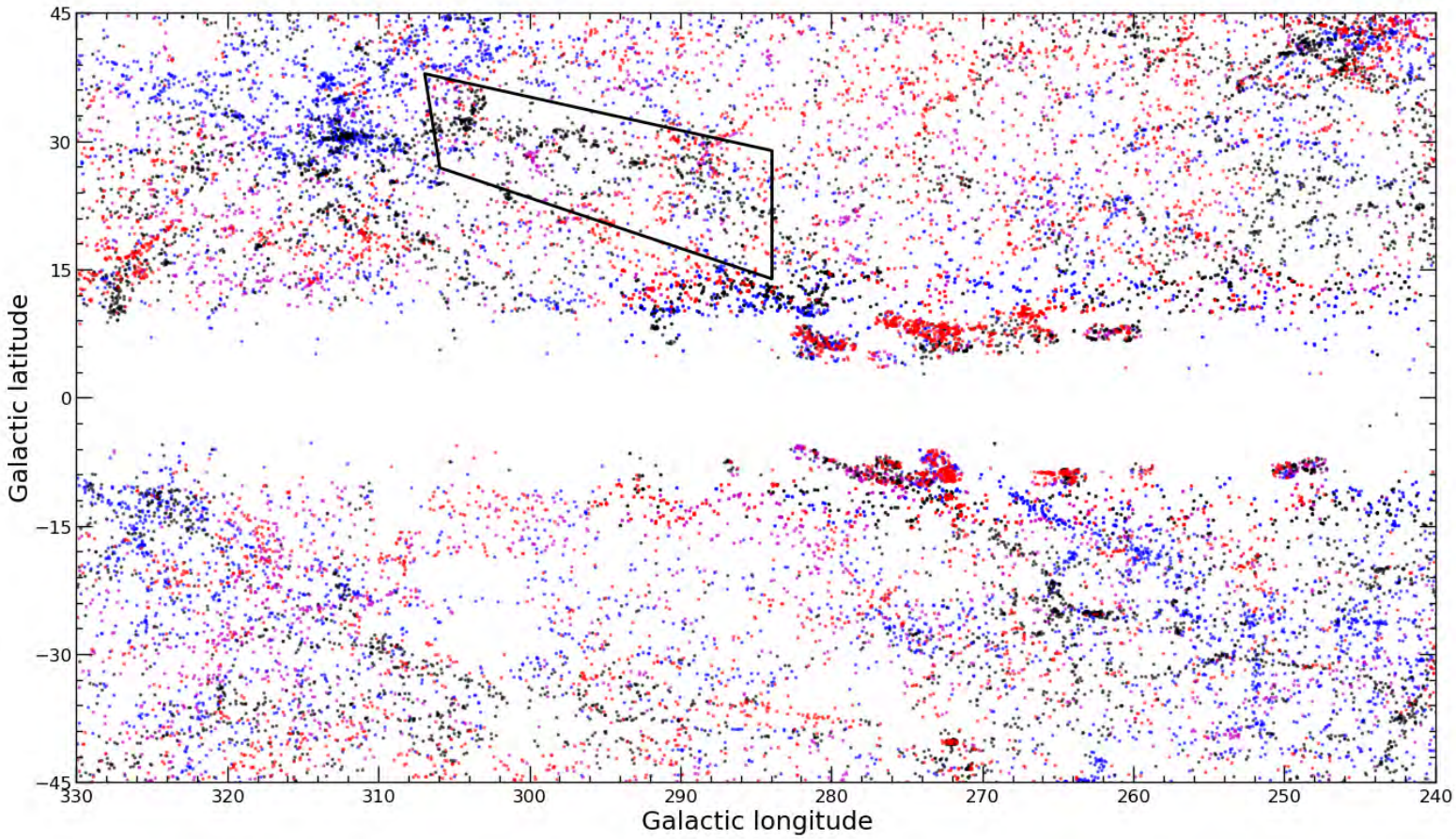

Figure 5.3: The on-sky distribution of the galaxies in the direction of the VSC ($z \sim 0.06$) and the SSC ($z \sim 0.05$), using spectroscopic redshifts. The galaxies presented in this figure are colour-coded according to redshifts: blue are the galaxies within redshift range $0.04 < z < 0.05$, black within $0.05 < z < 0.06$, red within $0.06 < z < 0.07$, and magenta within $0.07 < z < 0.08$.

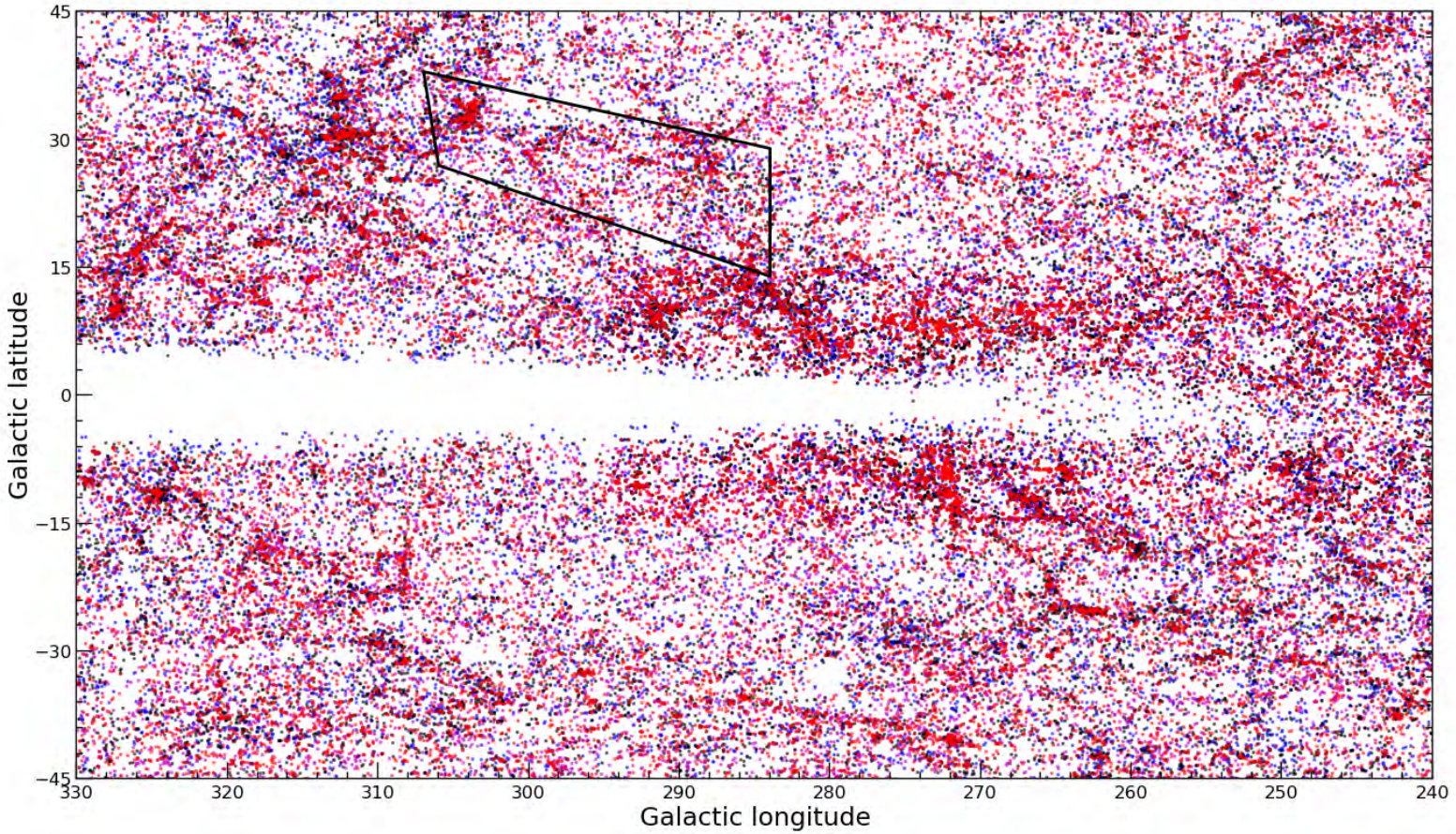

Figure 5.4: The on-sky distribution of the galaxies in the direction of the VSC ($z \sim 0.06$) and the SSC ($z \sim 0.05$), using photometric redshifts.The galaxies are colour-coded according to their redshifts similarly to Fig. 5.3

The filamentary structure, encapsulated by the trapezoidal shape, in Figs. 5.3-5.4 suggests a possible link between the SSC and the VSC. Prof. T. Jarrett used the photometric and the spectroscopic redshifts and smoothed the data according to their integrated flux, in an attempt to enhance the visibility of the large-scale structures in that region. The net product of this is Fig. 5.5, in which the galaxies are colour-coded according to redshifts: green are galaxies within the redshift range $0.04 < z < 0.055$, yellow within $0.055 < z < 0.07$, and orange within $0.07 < z < 0.085$. The filamentary structure is quite distinctive in this figure. The VSC has been shown to be a major, very extended supercluster. The above discussion has emphasised its location within the cosmic neighbourhood.

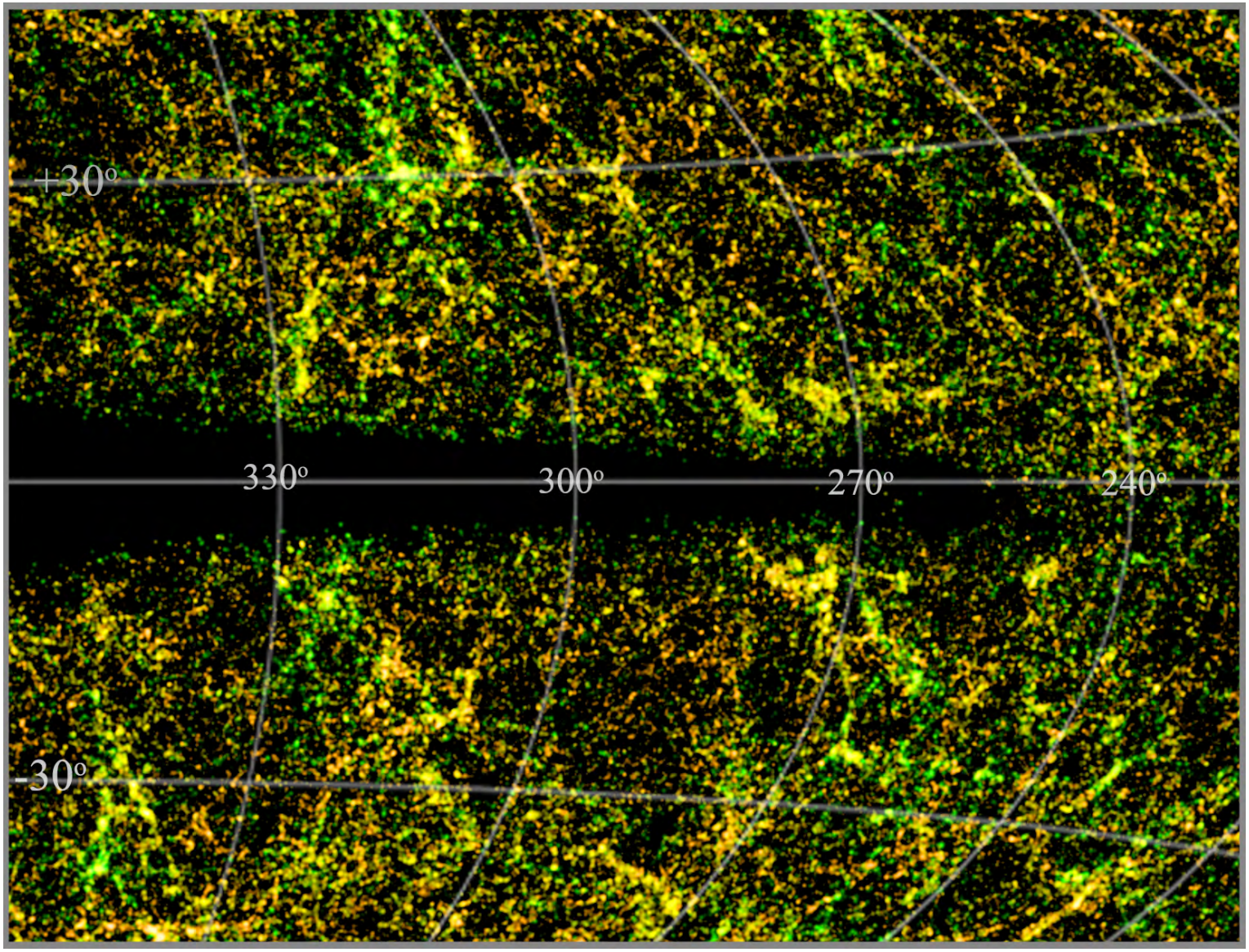

Figure 5.5: The smoothed distribution of the galaxies in the direction of the VSC ($z \sim 0.06$) and the SSC ($z \sim 0.05$), using spectroscopic/photometric redshifts. The galaxies in this figure is coded according to redshifts: green are galaxies within redshifts range $0.04 < z < 0.055$, yellow within $0.055 < z < 0.07$, and orange within $0.07 < z < 0.085$ (Tom Jarrett private commun.).

5.4 Summary

In this chapter, I discussed the extent of the VSC both in spectroscopic and photometric redshift space. Based on spectroscopic redshifts, the on-sky distribution of the galaxies in the direction of both the VSC and the SSC is presented in Fig. 5.3. From this figure the SSC is centred at $(315°, 30°)$, and extends about $12° \times 30°$ on-sky (Proust et al. 2006). At $cz = 14,500\,\mathrm{km\ s^{-1}}$, the extent of the SSC translates to $50 \times 112\,\mathrm{Mpc}$ on-sky. Similarly, the VSC extends about $20° \times 20°$ on-sky. At $cz = 18,000\,\mathrm{km\ s^{-1}}$, the extent of the VSC translates to $87 \times 87\,\mathrm{Mpc}$ on-sky. Using photometric redshifts, the on-sky distribution of the galaxies in the direction of both the VSC and the SSC is presented in Figs. 5.4-5.5. From these figures the VSC appears to be more extended than $87 \times 87\,\mathrm{Mpc}$. Further, we find a possible "bridge" between the VSC and the SSC. This surmised link is a filamentary structure that may well contain galaxy clusters and groups connecting both superclusters.

Chapter 6

Follow-Up Observations

6.1 NIR JHK_s Observations

To enhance our understanding of the true extent of the VSC, its mass, number of rich clusters within it, and to study its connection to other superclusters, such as the SSC, deeper observations are necessary. The first step toward this process is to conduct deeper infrared observations for the known potential clusters within this supercluster. The infrared band is the most suitable waveband because it is less affected by the dust of the Milky Way unlike the optical waveband.

As previously discussed, the Master Catalogue originates from a deep optical source catalogues in the southern Milky Way in the Hydra/Antlia region (Kraan-Korteweg 2000a), and the adjacent Vela region (von Maltitz 2012), as well as from the near infrared 2MASS XSC (Skrutskie et al. 2006, Jarrett et al. 2000a). The depth of the optical sample is limited to a B-band magnitude of $B_J \sim 18^m.5$. This translates to an absolute magnitude of $M_{B_J} = -18^m.5$, at the average distance of this supercluster $\sim 240\,\mathrm{Mpc}$. Further, the optical sample is severely affected by varying foreground extinction and has typical extinction values of $A_{B_J} \sim 0.^m3 - 10^m.0$. On the other hand, the 2MASS is complete to $K_s = 13^m.5, M_{K_s} = -23^m.4$. Indeed, it is less affected by dust and has typical extinction values of $A_{K_s} \sim 0.^m1 - 1^m.0$. These absolute magnitudes are only about $\sim 1^m.0$ below the characteristic absolute magnitude M^* for typical clusters (Gardner et al. 1997, Lin et al. 2004) which is not enough to draw firm conclusions on the mass or the richness of these clusters. Hence, I put forward a proposal to observe the potential galaxy clusters within the VSC using the Infrared Survey Facility (IRSF) telescope at the SAAO.

The IRSF telescope is an Alt-Azimuth Cassegrain telescope, that uses a near infrared camera (SIRIUS), capable of imaging three near infrared bands (JHK_s) simultaneously. The Simultaneous 3-color Infrared Imager for Unbiased Survey (SIRIUS) contains three detectors, 1024×1024 pixel HgCdTe HAWAII arrays. The camera has limiting magnitudes

of $J = 20.6, H = 19.4, K_s = 19.1$, a field of view of 7.8arcmin/frame, and a plate scale of $0.45''$/pixel (Nagashima et al. 1999). Using this camera is advantageous to the VSC studies. For instance, these observations will help in perusing the spatial distribution of the galaxies from the centre of each cluster as well as the number density distribution. A much deeper K_s luminosity function can be obtained. These luminosity functions will give concrete insights to the richness of the VSC potential clusters, and will allow the comparison between these clusters and neighbouring clusters.

The idea was to image an area close to the size of the Abell radius of the respective cluster. We made imaging mosaics over an area of 46×46 arcmin^2 , i.e. a grid of 6×6 slightly overlapped fields for each cluster. To avoid image saturation as a result of long exposure times (≥ 1 min), while at the same time enable faint galaxies detections we planned for multiple exposure frames. Following the approach of Woudt et al. (2005) and Nagayama et al. (2006) in observing clusters in the ZoA; each field was imaged in 25 successive frames of 24 s exposure each, the total observation time per field is 600 s. This means a factor of 4.5 better than 2MASS resolution $\sim 2^m.0$ deeper in K_s-band (Riad 2010), hence we can detect galaxies to greater levels of Galactic extinction and stellar density. Three weeks were allocated for our observations in February, March and April 2015. I was trained initially by K. Said for two days and completed the rest of the observations myself. Ten clusters were completely mapped. Unfortunately, because of the bad weather only the central part of $VC11$ was observed whereas $VC12$ and $VC13$ were not observed. A summary of the observations is given in Table 6.1.

Table 6.1: The IRSF/SIRIUS observations summary.

Cluster	Date	Run Number	Weather & Seeing
VC01	25/02/2015	1-575	P. Cloudy, 67% Humidity, seeing 1.8″
	27/02/2015	1-225	P. Cloudy, 48% Humidity, seeing 1.5″
VC02	27/02/2015	226-600	P. Cloudy, 48% Humidity, seeing 1.5″
	28/02/2015	100-525	P. Cloudy, 50% Humidity, seeing 1.6″
VC03	28/02/2015	526-850	P. Cloudy, 50% Humidity, seeing 1.6″
	01/03/2015	1-250	P. Cloudy, 50% Humidity, seeing 1.5″
	02/03/2015	100-325	Clear, 20% Humidity, seeing 1.35″
VC04	02/03/2015	326-1125	Clear, 20% Humidity, seeing 1.35″
VC07	03/03/2015	100-700	P. Cloudy, 15% Humidity, seeing 2.15″
	25/03/2015	1-150 & 176-275	P. Cloudy, 75% Humidity, seeing 1.45″
VC05	25/03/2015	276-325	P. Cloudy, 75% Humidity, seeing 1.45″
	26/03/2015	100-325	P. Cloudy, 75% Humidity, seeing 1.0″
	28/03/2015	100-350	Clear, 30% Humidity, seeing 1.0″
VC06	28/03/2015	351-575 &651-900	Clear, 30% Humidity, seeing 1.0″
	29/03/2015	1-325	Clear, 34% Humidity, seeing 1.1″
VC08	29/03/2015	326-475 &501-725	Clear, 34% Humidity, seeing 1.1″
	30/03/2015	1-425	P. Cloudy, 50% Humidity, seeing 1.4″
VC09	30/03/2015	451-750	P. Cloudy, 50% Humidity, seeing 1.4″
	31/03/2015	1-225	P. Cloudy, 40% Humidity, seeing 1.02″
	01/04/2015	1-175	P. Cloudy, 50% Humidity, seeing 1.02″
	03/04/2015	1-125	Clear, 27% Humidity, seeing 1.45″
VC10	03/04/2015	126-275	Clear, 27% Humidity, seeing 1.45″
	04/04/2015	1-150	P. Cloudy, 70% Humidity, seeing 2.10″
	05/04/2015	1-250	Clear, 70% Humidity, seeing 1.45″
	07/04/2015	1-250	Clear, 80% Humidity, seeing 2.02″
VC11	07/04/2015	251-525	Clear, 80% Humidity, seeing 2.02″

6.2 WISE Follow-Up

In addition to the IRSF observations, I used WISE to inspect and identify galaxies for a subset of clusters within the VSC. This was intended as a pilot project to examine the ability of WISE in identifying galaxies within the ZoA. I studied three galaxy clusters using WISE, namely, VC06, VC10, as well as VC13. The purpose behind the WISE search is to explore the clusters' true richness, and to prepare new targets for follow-up spectroscopic observations and thus have conclusive measurement for the velocity dispersion and the mass of these overdensities. On average, I found ~ 300 new galaxies in each cluster that were not in our source catalogues. As an example, Fig. 6.1 shows the on-sky distribution of the galaxies in the VC10 cluster. The red points are the galaxy cluster members. These members lies within 1 Abell radius and within 3σ of the mean velocity of the cluster. The black dot is the optimised cluster/group center. The blue dots are the foreground and background surrounding galaxies for which we have redshift measurements, while the green are the foreground and background surrounding galaxies for which we have no redshift measurements. The magenta dots are the new galaxies found using WISE. The black circle delimits the AAOmega observation field. A list of the prepared targets for the three galaxy clusters are in Appendix D.

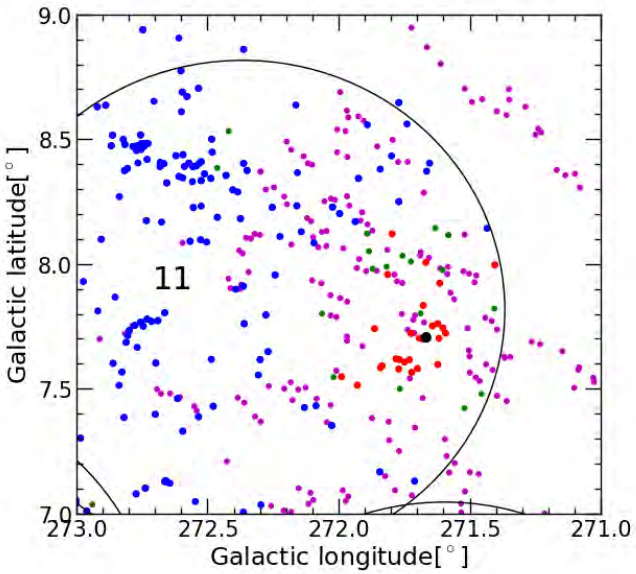

Figure 6.1: The on-sky distribution of the galaxies in VC10. The red are the galaxy cluster members. The black dot is the optimised central galaxy. The blue dots are the foreground and background surrounding galaxies for which we have redshift measurements, while the green dots are the foreground and background surrounding galaxies for which we have no redshift measurements. The magenta dots are the new galaxies found using WISE. The black circle delimit the AAOmega observation field.

Chapter 7

Conclusion

The purpose of this thesis was to investigate the conjectured presence of a massive supercluster hidden by the Zone of Avoidance (ZoA) in the Hydra/Antlia and Vela regions ($245° \lesssim l \lesssim 295°, |b| \lesssim 10°$) at approximately $cz \sim 18,000$ km s^{-1}, and assess its extent and mass. This prospective supercluster is called the Vela Supercluster (VSC), for the constellation in which it is located. A further aspect of this project was to scrutinise this potential supercluster and identify the galaxy clusters and the galaxy groups contained within it. Both spectroscopic and photometric redshifts for the galaxies in the direction of the VSC were used to study this structure, examine its possible extent and connections with large-scale structures adjacent to the ZoA.

I prepared a homogeneous redshift catalogue that contains 5, 190 science quality redshifts for the galaxies in the Hydra/Antlia and Vela regions. The galaxies in this catalogue are based on deep optical galaxy source catalogues in the ZoA (Kraan-Korteweg 2000a, von Maltitz 2012), and the near infrared 2MASS Extended Source Catalogue (XSC) (Jarrett et al. 2000a, Skrutskie et al. 2006). The observed redshifts were mainly obtained using the 2dF+AAOmega spectrograph at the Anglo-Australian Telescope ($N = 4126$). Other redshift data are the result of earlier unpublished and complementary work by Kraan-Korteweg and collaborators. These are from the 6dF instrument on the Anglo-Australian Observatory's UK Schmidt Telescope ($N = 86$), Optopus multiobject spectrograph facility on the ESO 3.6 m telescope at La Silla ($N = 146$), the Southern African Large Telescope ($N = 38$), and the South African Astronomical Observatory (SAAO) using the 1.9 m telescope ($N = 34$). The redshift catalogue was further complemented with redshifts in the literature using the extragalactic database HYPERLEDA ($N = 760$).

The velocity distribution of the VSC has a very prominent peak centred at $v \sim 18000 \pm 1000$ km s^{-1} and associated with extended shoulders that range from $15000 - 23000$ km s^{-1}. This velocity distribution is very similar to that of the Shapley Supercluster (SSC), refer to Fig. 2 in Proust et al. (2006). This indicates that the VSC likely is a massive supercluster.

The velocity distribution of the VSC is equally prominent on either side of the Galactic plane, which suggests that the VSC might be continuous across the plane, and as a result have a width of about $\Delta b \sim 20^\circ$ across the Galactic plane. The large-scale distribution of galaxies in the VSC hints that this candidate supercluster is embedded in a wall-like structure that extends over 87 Mpc on-sky. The large-scale distribution of the galaxies in the potential VSC at $v \sim 18000\,\mathrm{km\ s^{-1}}$ (refer to Fig. 3.11) is approximately as prominent as the overdensity of the galaxies in the SSC at $v \sim 15,000\,\mathrm{km\ s^{-1}}$ (refer to Fig. 3.14). This provides another clue that the potential VSC is likely a strong supercluster candidate.

There are 13 potential galaxy clusters, and 22 potential galaxy groups within the VSC (see Fig. 4.3 and Tables 4.1-4.2). The identified galaxy clusters/groups are similar to the galaxy clusters/groups within the SSC, both in richness and velocity dispersion; refer to Table 4 in Proust et al. (2006). Being mindful of our sparse sampling, the above suggests that the VSC is comparable to the SSC. The on-sky distribution of the galaxies in both spectroscopic and photometric redshift space shows that the VSC extends for at least $\sim 20^\circ$ in Galactic longitude and 20° in Galactic latitude, which at $cz = 18,000\,\mathrm{km\ s^{-1}}$ translates to 87×87 Mpc on-sky. According to Proust et al. (2006), the SSC extends about $12^\circ \times 30^\circ$ on-sky, which at $cz = 14,500\,\mathrm{km\ s^{-1}}$ translates to 50×112 Mpc on-sky. This indicates that the VSC is more extended than the SSC. In photometric redshift space these two massive superclusters seem to be connected by a filamentary structure that may well contain further galaxy clusters and groups connecting both structures.

In conclusion, we showed that the VSC is a major supercluster similar to the well studied SSC. The existence of the VSC is expected to have significant implications on the Local Group motion and the bulk flow studies. Especially, if we put into perspective the close proximity between the VSC and the SSC, which is considered one of the major contributors to the bulk flow motion, and the recent residual bulk flow measurements (Springob et al. 2014, Tully et al. 2014). Thus the VSC may well be key in resolving the long-enduring bulk flow controversies and the misalignment of flows with the CMB measurement. Further, Sheth & Diaferio (2011) showed that structure formation models have difficulty in reconciling the existence of the SSC and the Sloan Great Wall with the assumption of Gaussian initial conditions and values of σ_8 less than 0.9. Consequently, the proximity of a further supercluster (VSC) is expected to increase this tension.

Appendix A

The Master Catalogue

In this appendix, I present the first page of the Master Catalogue. The full table is at
`http://www.ast.uct.ac.za/~ahmed/MasterCatalogue.dat`
This table contains the science quality redshifts (flag 3&4) that were used in our analysis throughout this thesis.
The table of galaxies with low flag redshifts (flag 1&2) is at
`http://www.ast.uct.ac.za/~ahmed/flag1and2MasterCatalogue.dat`
These redshifts were not included in ANY part of our analysis, it is presented here just for completeness.

Table A.1: The Master Catalogue.

Sym.	ID	α	δ	l	b	D	d	B_J	EBV	D^0	B_J^0	Mor.	K_s	K_s^0	z	flag	Sor.
		[^{h}:^{m}:^{s}]	[$^\circ$:$'$:$''$]	$^\circ$	$^\circ$	[$''$]	[$''$]	mag.	mag.	[$''$]	mag.	Mor.	mag.	mag.			
(1)	(2)	(3)	(4)	(5)	(6)	(7)	(8)	(9)	(10)	(11)	(12)	(13)	(14)	(15)	(16)	(17)	(18)
P3	Vel-379	7 25 46	-34 26 43	247.39	-8.53	34.0	27.0	16.1	0.23	48	14.9	E...	.	.	0.033	4	2dF
P5	2MX07255260-3458366	7 25 53	-34 58 36	247.88	-8.76	14.0	12.0	.	0.32	.	.	....	13.53	13.39	0.110	4	2dF
P1	2MX07260273-3416153-3956	7 26 03	-34 16 15	247.26	-8.40	9.0	9.0	18.8	0.19	12	17.8	E...	12.78	12.85	0.109	4	2dF
P3	Vel-394	7 26 10	-34 41 45	247.65	-8.57	50.0	9.0	16.9	0.27	74	15.4	S.ME	.	.	0.026	4	2dF
P3	Vel-397	7 26 16	-34 28 15	247.46	-8.45	16.0	4.0	19.2	0.23	21	18.0	S...	.	.	0.095	4	2dF
P3	Vel-407	7 26 22	-34 12 27	247.23	-8.31	24.0	7.0	17.9	0.20	30	16.9	S.E.	.	.	0.072	4	2dF
P3	HyA-652	8 53 07	-59 53 40	276.90	-9.70	8.0	5.0	19.6	0.16	9	18.8	....	.	.	0.080	4	2dF
P1	2MX09385056-3926036-2870	9 38 51	-39 26 04	267.22	9.73	13.0	7.0	19.0	0.28	19	17.5	S.E.	13.31	13.13	0.064	4	6dF
P1	2MX09392610-3933307-2881	9 39 26	-39 33 31	267.39	9.71	19.0	5.0	19.0	0.31	30	17.3	S.E.	12.59	12.43	0.065	4	6dF
P1	2MX09394995-4234257-2894	9 39 50	-42 34 26	269.49	7.52	13.0	13.0	18.0	0.39	27	15.7	E...	12.24	12.04	0.066	4	6dF
P1	2MX09395130-3947567-2895	9 39 51	-39 47 57	267.62	9.59	19.0	13.0	17.8	0.34	33	15.9	S.E.	11.54	11.44	0.065	4	6dF
P1	2MX09403940-3929038-2905	9 40 39	-39 29 04	267.52	9.93	16.0	8.0	18.6	0.27	23	17.2	S.E.	13.82	13.73	0.064	4	6dF
P1	2MX09410448-4233574-2915	9 41 04	-42 33 57	269.65	7.68	13.0	7.0	19.1	0.40	28	16.7	S...	13.13	13.00	0.064	4	6dF
P5	2MX09413835-4151368	9 41 38	-41 51 37	269.26	8.28	29.0	23.0	.	0.52	.	.	....	12.73	12.35	0.315	3	6dF
P5	2MX09424517-4215563	9 42 45	-42 15 56	269.69	8.11	24.0	20.0	.	0.40	.	.	....	12.97	12.67	0.112	4	6dF
P3	Vel-2304	9 10 02	-36 24 59	264.00	7.84	20.0	5.0	18.7	0.25	28	17.3	S...	.	.	0.055	4	2dF
P3	Vel-2317	9 10 21	-36 21 29	264.00	7.93	13.0	8.0	18.8	0.24	18	17.5	S...	.	.	0.059	4	2dF
P3	HyA-2706	10 33 37	-51 09 59	282.03	6.03	20.0	11.0	17.7	0.33	34	15.9	....	.	.	0.053	4	2dF
P3	HyA-2708	10 33 50	-49 47 16	281.36	7.23	17.0	9.0	18.4	0.29	26	16.8	....	.	.	0.059	4	2dF
P3	HyA-2709	10 33 58	-50 21 24	281.67	6.75	19.0	7.0	18.7	0.28	27	17.2	S..?	.	.	0.084	4	2dF
P3	HyA-2711	10 34 07	-52 00 30	282.53	5.34	15.0	3.0	20.1	0.29	22	18.6	S...	.	.	0.049	4	2dF
P3	HyA-2713	10 34 21	-49 34 08	281.32	7.46	12.0	8.0	19.3	0.36	22	17.2	....	.	.	0.072	4	2dF
P3	HyA-2718	10 34 47	-49 49 49	281.51	7.27	13.0	7.0	19.0	0.29	20	17.4	S..?	.	.	0.066	4	2dF
P3	HyA-2719	10 34 51	-50 16 01	281.74	6.90	13.0	9.0	18.6	0.30	19	17.1	....	.	.	0.064	4	2dF
P3	HyA-2721	10 34 55	-50 59 05	282.12	6.29	15.0	3.0	19.8	0.28	22	18.3	S...	.	.	0.119	4	2dF
P3	HyA-2726	10 35 06	-49 46 13	281.53	7.35	17.0	7.0	18.5	0.32	28	16.7	....	.	.	0.049	4	2dF
P3	HyA-2729	10 35 17	-49 00 20	281.17	8.03	16.0	7.0	18.6	0.28	23	17.1	....	.	.	0.084	4	2dF
P3	HyA-2731	10 35 20	-49 17 36	281.32	7.78	15.0	9.0	18.9	0.35	27	16.9	....	.	.	0.095	4	2dF
P3	HyA-2732	10 35 26	-49 58 27	281.68	7.20	19.0	4.0	19.3	0.32	31	17.5	S...	.	.	0.068	4	2dF
P3	HyA-2741	10 35 59	-50 09 13	281.85	7.09	13.0	9.0	18.8	0.36	24	16.7	....	.	.	0.065	4	2dF
P3	HyA-2745	10 36 34	-49 20 30	281.52	7.84	16.0	7.0	19.3	0.35	28	17.4	....	.	.	0.065	4	2dF
P3	HyA-2747	10 36 44	-49 20 40	281.54	7.85	20.0	4.0	19.5	0.36	35	17.6	S...	.	.	0.070	4	2dF
P3	HyA-2760	10 37 55	-49 21 47	281.72	7.93	13.0	7.0	19.5	0.36	23	17.6	....	.	.	0.083	4	2dF
P5	2MX10381973-5016447	10 38 20	-50 16 45	282.24	7.17	20.0	20.0	.	0.46	.	.	....	13.74	13.57	0.122	4	2dF
P3	HyA-2781	10 39 35	-49 39 25	282.11	7.81	17.0	5.0	19.4	0.39	32	17.3	S...	.	.	0.049	4	2dF
P5	2MX10393520-4955078	10 39 35	-49 55 08	282.24	7.58	20.0	20.0	.	0.42	.	.	....	13.48	13.32	0.065	4	2dF
P3	HyA-2782	10 39 38	-49 25 52	282.00	8.01	15.0	5.0	18.8	0.35	26	16.8	S...	.	.	0.063	4	2dF
P3	HyA-2793	10 40 03	-50 20 04	282.50	7.25	20.0	7.0	18.9	0.45	46	16.3	S..?	.	.	0.024	4	2dF
P3	HyA-2797	10 40 34	-49 25 01	282.13	8.10	42.0	31.0	16.1	0.33	69	14.3	I.9?	.	.	0.043	4	2dF
P5	2MX10415569-4903526	10 41 56	-49 03 53	282.15	8.51	23.0	23.0	.	0.32	.	.	....	13.10	12.98	0.139	4	2dF

Appendix B

AAOmega Observations

Table B.1: This table describes the AAOmega+2dF observations at the Anglo-Australian Telescope.

Date	Field	Run number	Obs Type	Exposure Time (sec)	Weather
1/Feb/2014	F6	36-39	SCI	4×1800	Partly cloudy.
	F20	43-45	SCI	3×1800	
	F8	49-51	SCI	3×1800	
	F12	52-54	SCI	3×1800	
2/Feb/2014	F2	24-26	SCI	3×1500	Clear.
	F5	30-32	SCI	3×1500	
	F24	36-38	SCI	3×1500	
	F17	42-44	SCI	3×1500	
	F19	47-49	SCI	3×1800	
3/Feb/2014	F22	9-11	SCI	3×1800	Clear at the beginning, but cloudy at the end.
	F23	15-17	SCI	3×1500	
	F9	21-23	SCI	3×1500	
	F11	27	SCI	1000	
4/Feb/2014	F3	68-70	SCI	3×1500	Thin and patchy clouds at the beginning.
	F6Y	74-76	SCI	3×1500	
	F21	70-82	SCI	3×1800	
	F11	86-88	SCI	3×1500	
	F13	89-91	SCI	3×1800	
5/Feb/2014	F35	4-6	SCI	3×1800	Very cloudy.
	F36	10-11	SCI	2300	
6/Feb/2014	F25	8-9	SCI	2×1800	Clear.
	F36	13-14	SCI	2×1200	
	F31	18-19	SCI	2×1800	
	F32	23-24	SCI	2×1800	
	F34	28-29	SCI	2×1800	
	F18	33-34	SCI	2×1800	
	F38	35-36	SCI	2×2100	

Appendix C

Potential Clusters/Groups within the Vela Supercluster

Galaxy Clusters Candidates:

VC01: $(l, b) = (249.59°, -8.44°)$, $(\alpha, \delta) = (112.77°, -36.34°)$, $E(B-V) = 0.35$

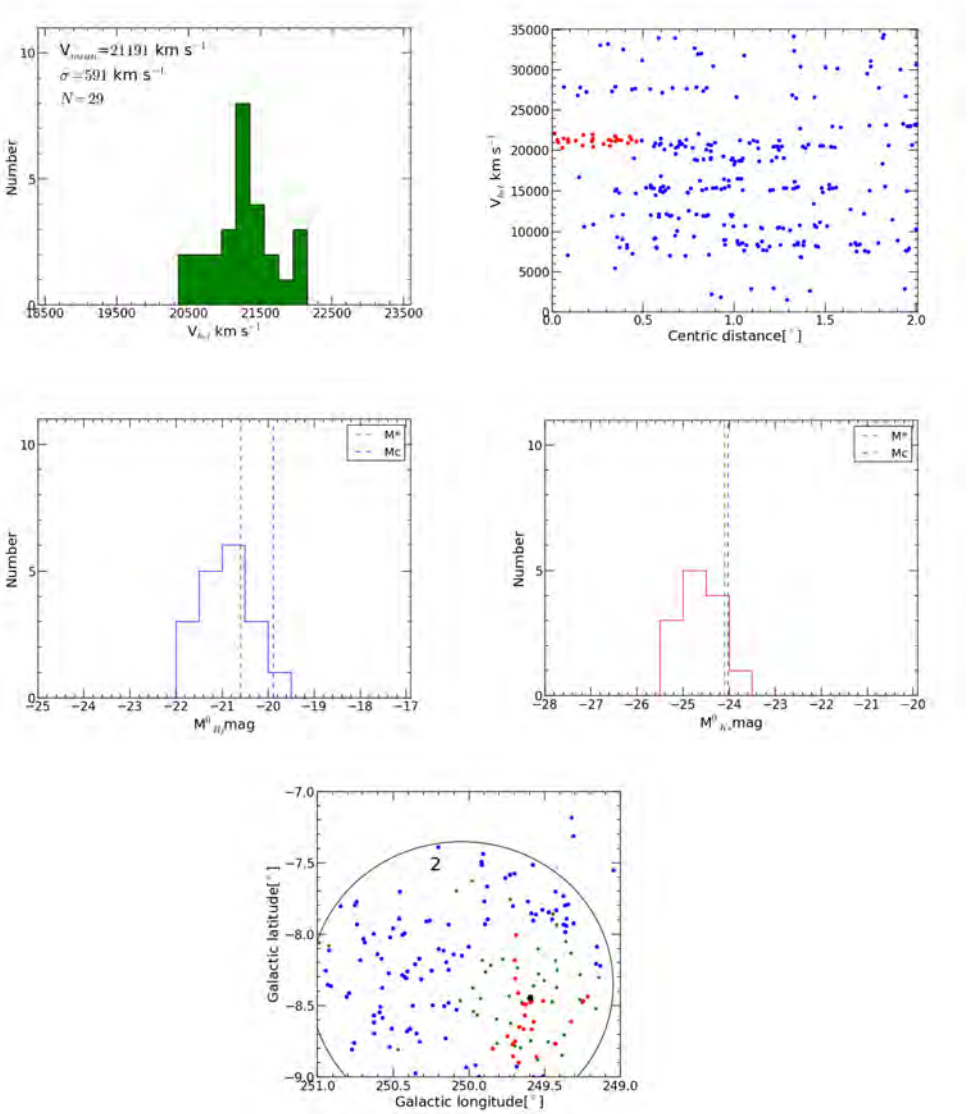

Figure C.1: From panel 1 this area has a gaussian velocity histogram that peaks around $\sim 21,500\,\mathrm{km\ s^{-1}}$. Panel 2 shows relatively high concentration near the centre. From this and the luminosity function, panel 3 and 4, this region is a potential cluster candidate. It has a mass of $8.11 * 10^{14}\,\mathrm{M}_{\odot}$.

VC02: $(l, b) = (264.67°, -8.60°)$, $(\alpha, \delta) = (122.69°, -49.39°)$, $E(B-V) = 0.29$

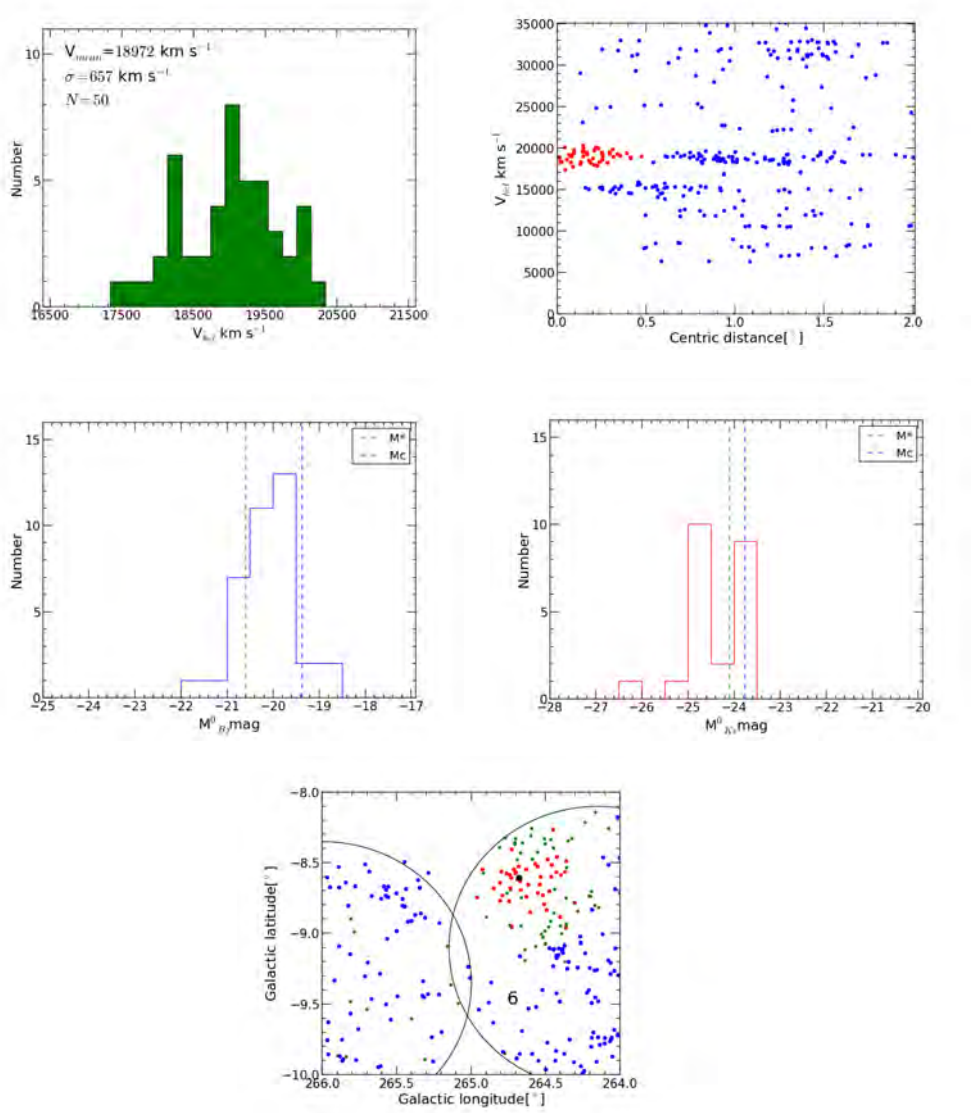

Figure C.2: From the conspicuous gaussian histogram shape appearing in panel 1 (peaks around $\sim 19,000\,\mathrm{km\ s^{-1}}$), the very dense centre appearing in panel 2 (almost 30 galaxies lie within 600 km $\mathrm{s^{-1}}$ from the centre), and from the luminosity function, panel 3 and 4, this region represents a potential cluster candidate with mass of $1.0 * 10^{15}\,\mathrm{M_\odot}$.

VC03: $(l, b) = (265.56°, -8.73°)$, $(\alpha, \delta) = (123.25°, -50.20°)$, $E(B-V) = 0.40$

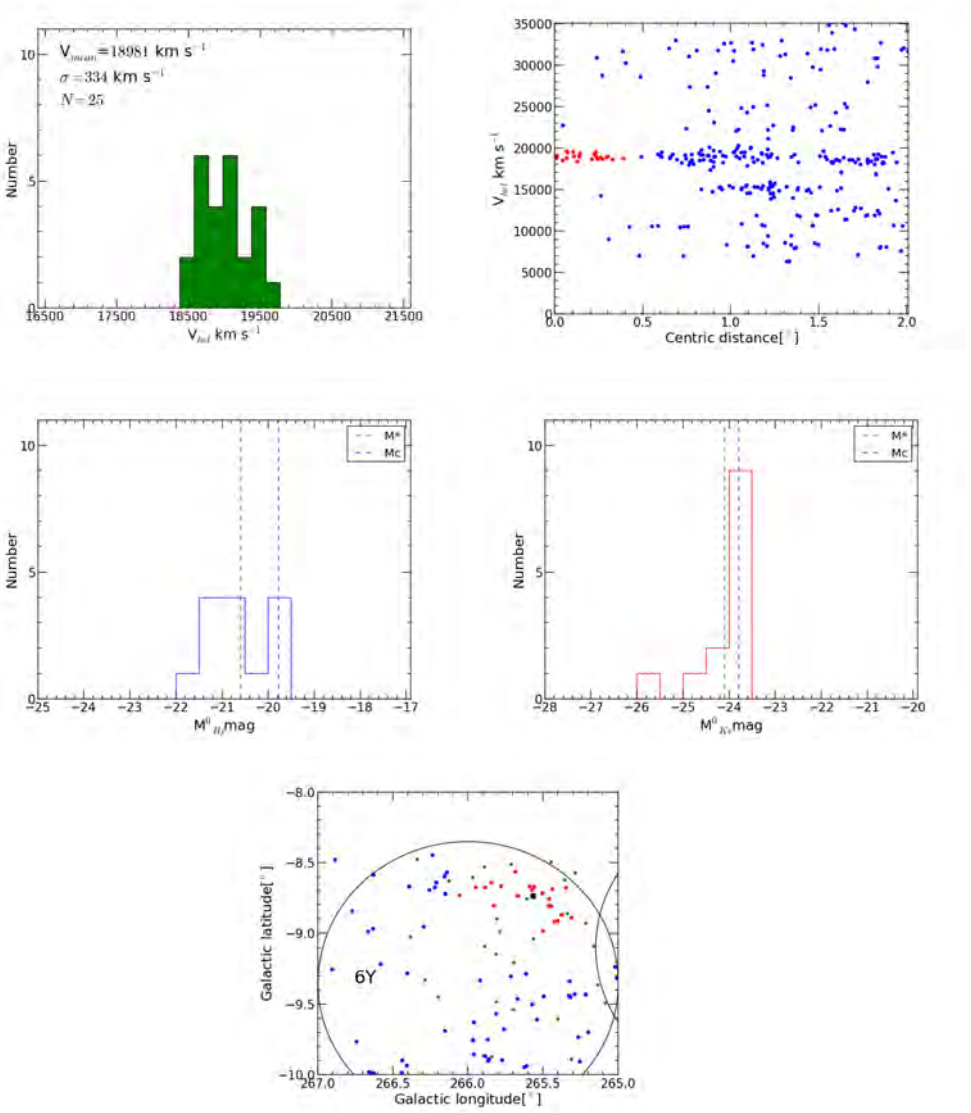

Figure C.3: From the gaussian histogram shape in panel 1 (peaks around $\sim 19,000\,\mathrm{km\ s^{-1}}$), the luminosity function in panel 3 and 4, and the high concentration around the centre (16 galaxies with $300\,\mathrm{km\ s^{-1}}$) in panel 2, this region is a weak cluster candidate. It has a mass of $2.59 * 10^{14}\,\mathrm{M_\odot}$. This cluster lies at the border of the AAOmega field and hence some galaxies that belong to this candidate were not observed (the green dots).

VC04: $(l, b) = (272.27°, -8.96°)$, $(\alpha, \delta) = (129.14°, -55.81°)$, $E(B-V) = 0.16$

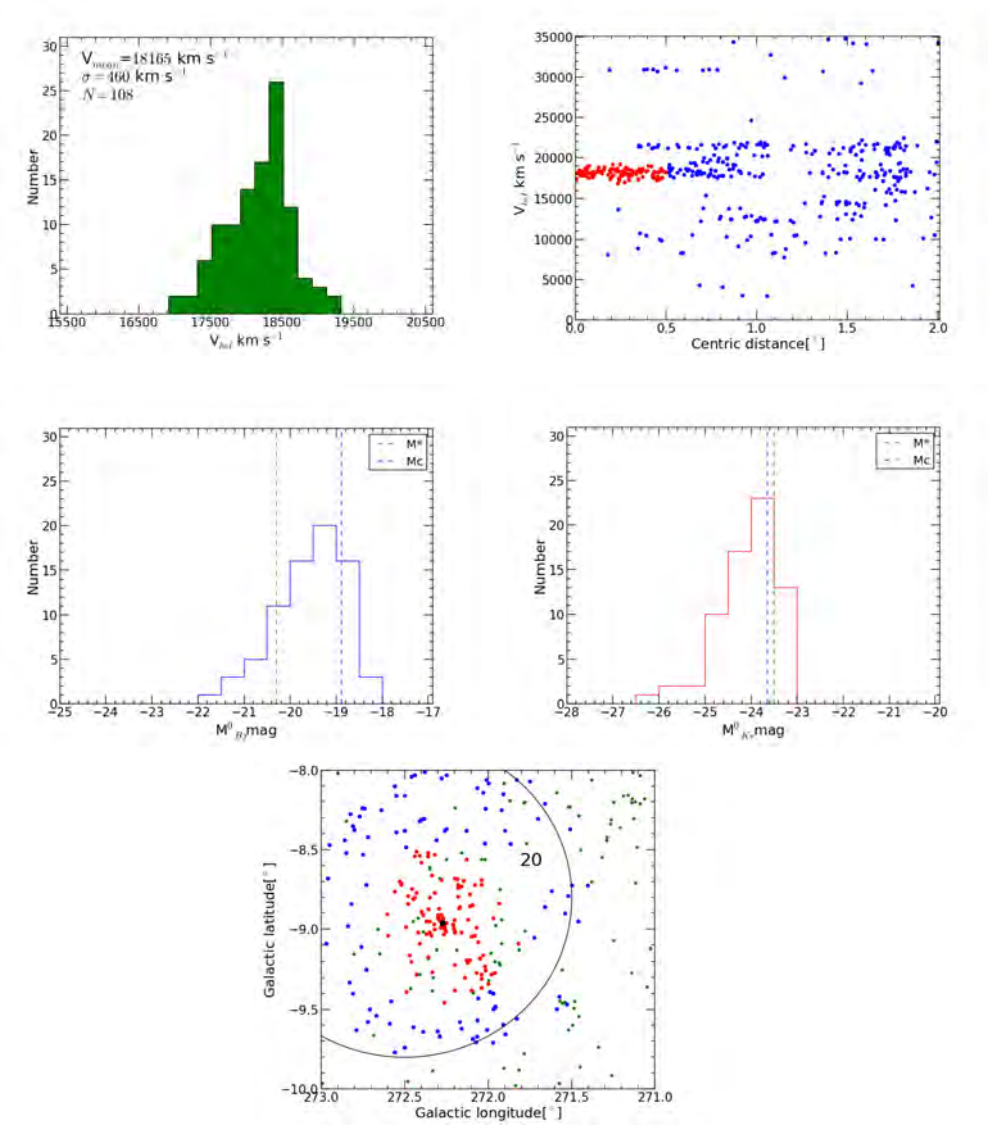

Figure C.4: This area is a potential cluster candidate with mass equals $4.91 * 10^{14}\,M_{\odot}$. This cluster is the densest cluster in the Vela and Hydra/Antlia region. Though it has a small mass compared to the other potential cluster candidates, this is due to the small velocity dispersion of its members since it is virialized and most likely in a state of equilibrium (very early cluster).

VC05: $(l, b) = (273.84°, -9.65°)$, $(\alpha, \delta) = (129.78°, -57.47°)$, $E(B-V) = 0.16$

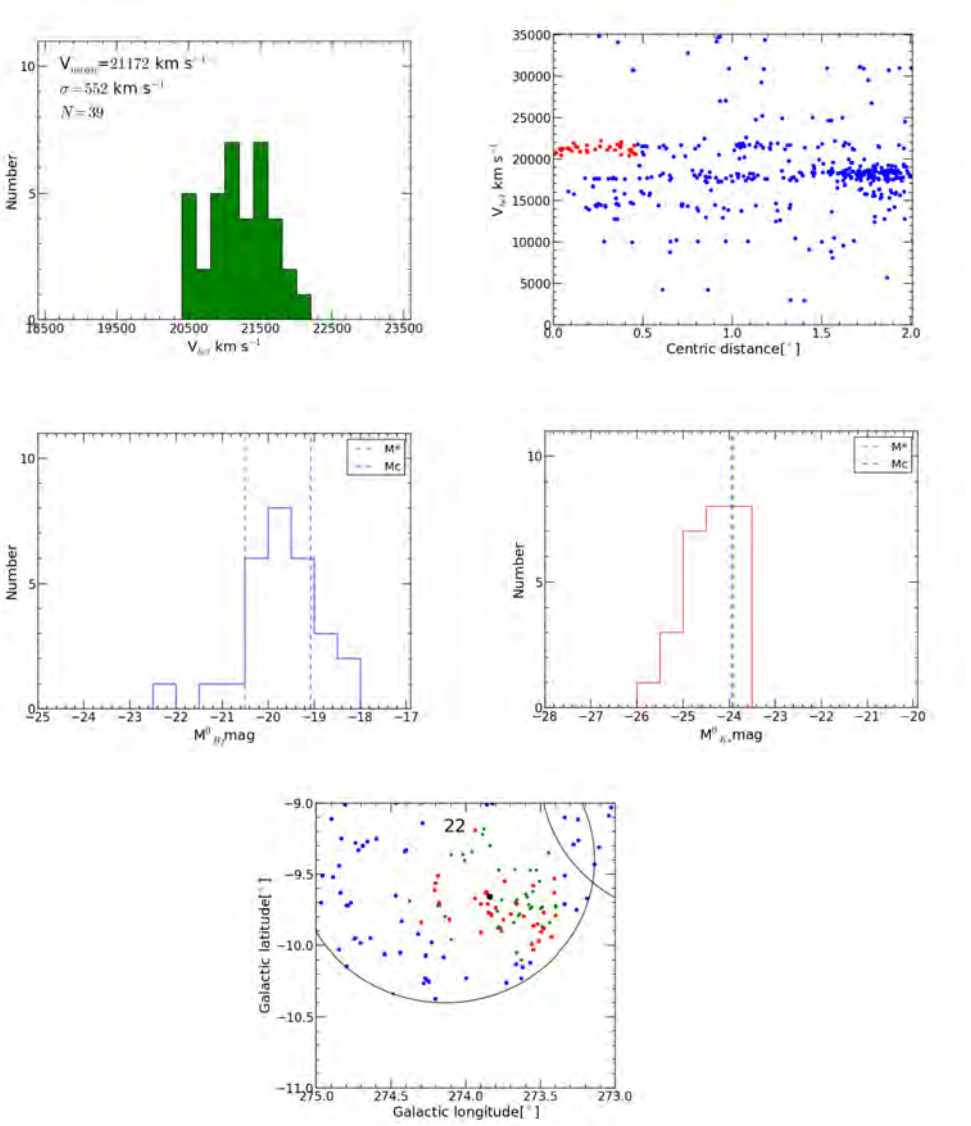

Figure C.5: From panel 1 this area has a gaussian velocity histogram with a high peak around $\sim 21,000\,\mathrm{km\ s^{-1}}$. Panel 2 shows relatively high concentration near the centre. From this and the luminosity function, panel 3 and 4, this region likely is a potential cluster candidate. It has a mass of $7.08 * 10^{14}\,\mathrm{M}_{\odot}$.

VC06: $(l, b) = (275.65°, -9.88°)$, $(\alpha, \delta) = (131.49°, -59.04°)$, $E(B-V) = 0.18$

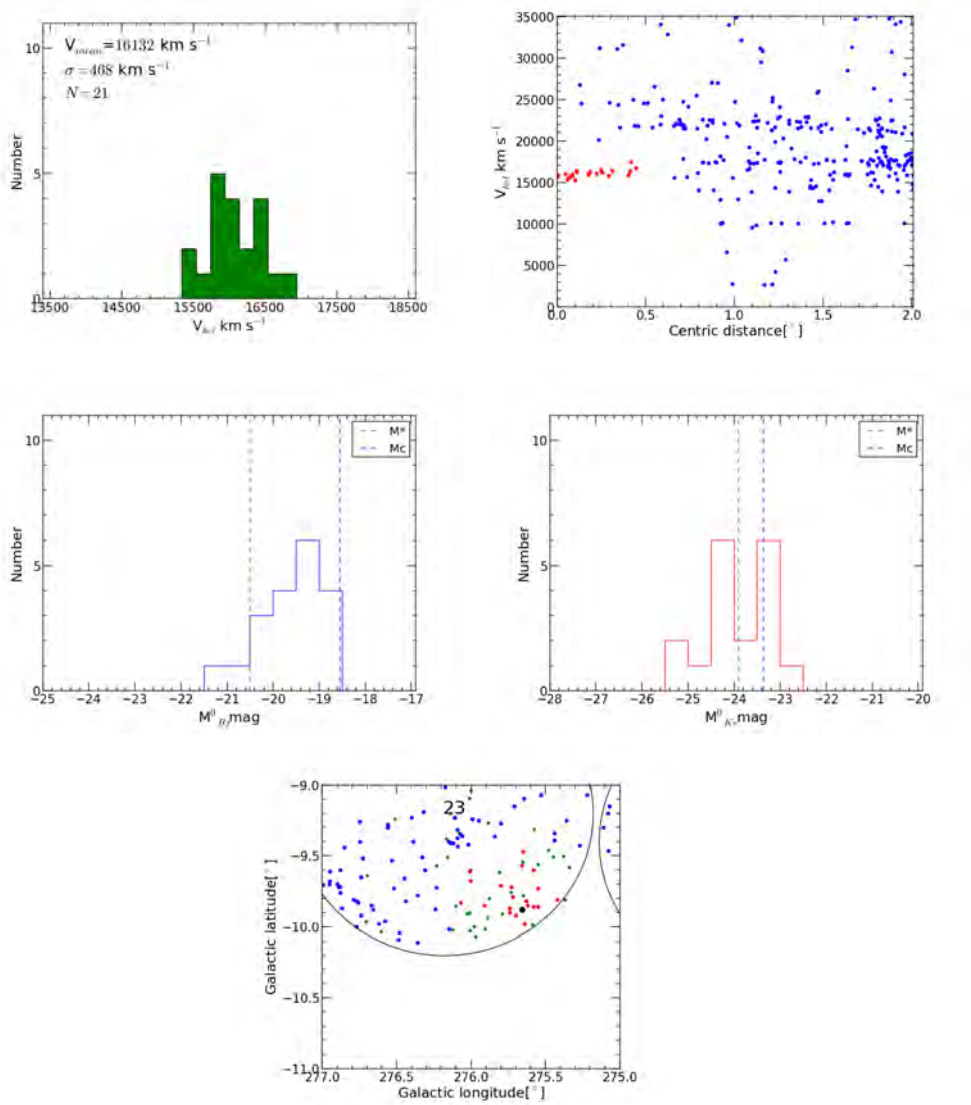

Figure C.6: From panel 1 this area has a relatively broad histogram shape with multi-peaks around $\sim 16,000\,\mathrm{km\ s^{-1}}$. Panel 2 shows relatively high concentration near the centre. From this and the luminosity function, panel 3 and 4, this region is a weak cluster candidate. It has a mass of $5.09 * 10^{14}\,\mathrm{M}_{\odot}$. This cluster candidate lies at the border of the AAOmega field, and many galaxies that lie within one Abell radius from the centre are not sampled (the green dots).

VC07: $(l, b) = (273.75°, -6.98°)$, $(\alpha, \delta) = (133.52°, -55.76°)$, $E(B-V) = 0.24$

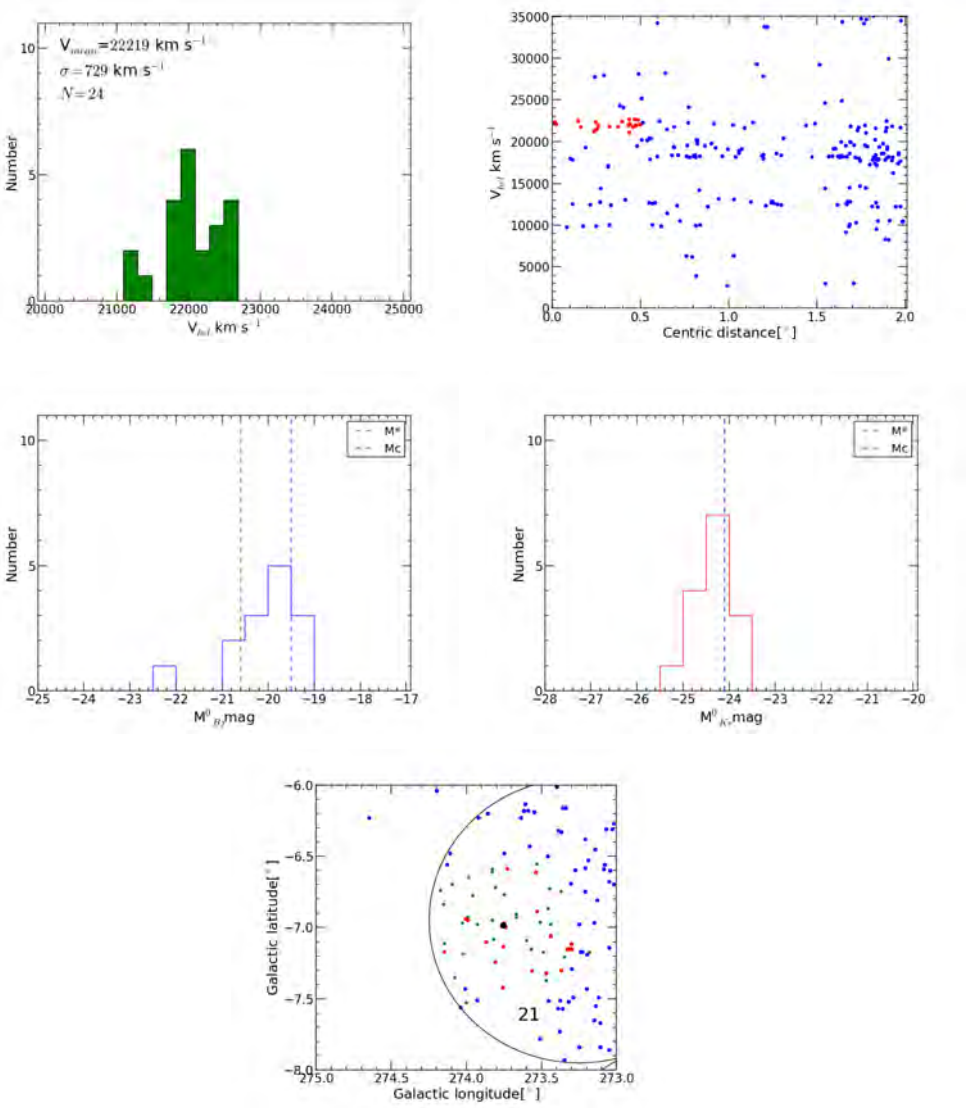

Figure C.7: From the gaussian velocity histogram in panel 1 (peaks around $\sim 22,000$ km s^{-1}), the very little number of galaxies around the centre in panel 2, and the luminosity function, panel 3 and 4, this region is a weak cluster candidate with mass of $1.23 * 10^{15}\,M_{\odot}$. This cluster is undersampled, as most of the galaxies that lie within one Abell radius from the centre of this candidate were not observed by our AAOmega observations.

VC08: $(l, b) = (275.65°, -7.83°)$, $(\alpha, \delta) = (134.54°, -57.75°)$, $E(B-V) = 0.24$

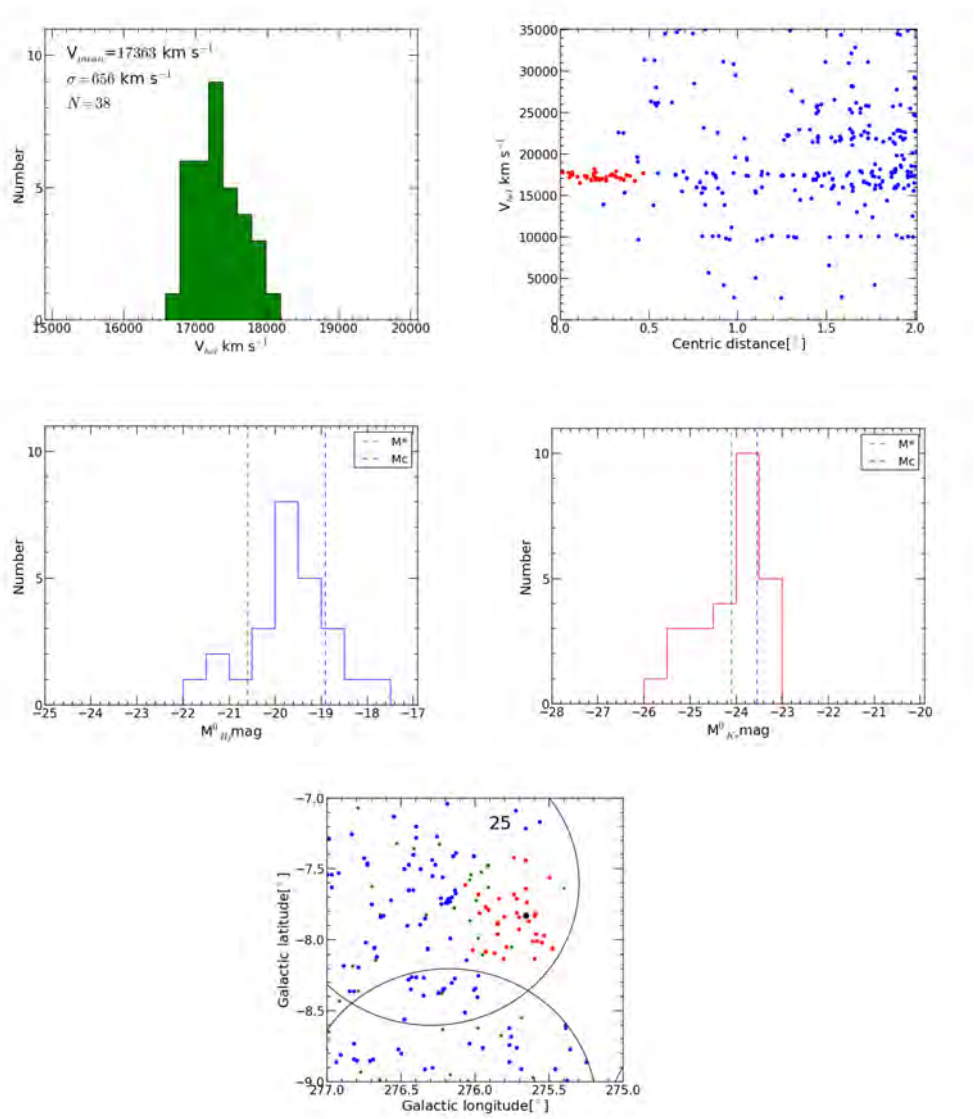

Figure C.8: From panel 1 this area has a gaussian velocity histogram that peaks around ($\sim 17,500\,\mathrm{km\ s^{-1}}$). Panel 2 shows a very high concentration near the centre. From this and the luminosity function, panel 3 and 4, this region likely is a strong cluster candidate. It has a mass of $1.0 * 10^{15}\,\mathrm{M}_{\odot}$.

VC09: $(l, b) = (267.22°, 9.80°)$, $(\alpha, \delta) = (144.77°, -39.37°)$, $E(B-V) = 0.29$

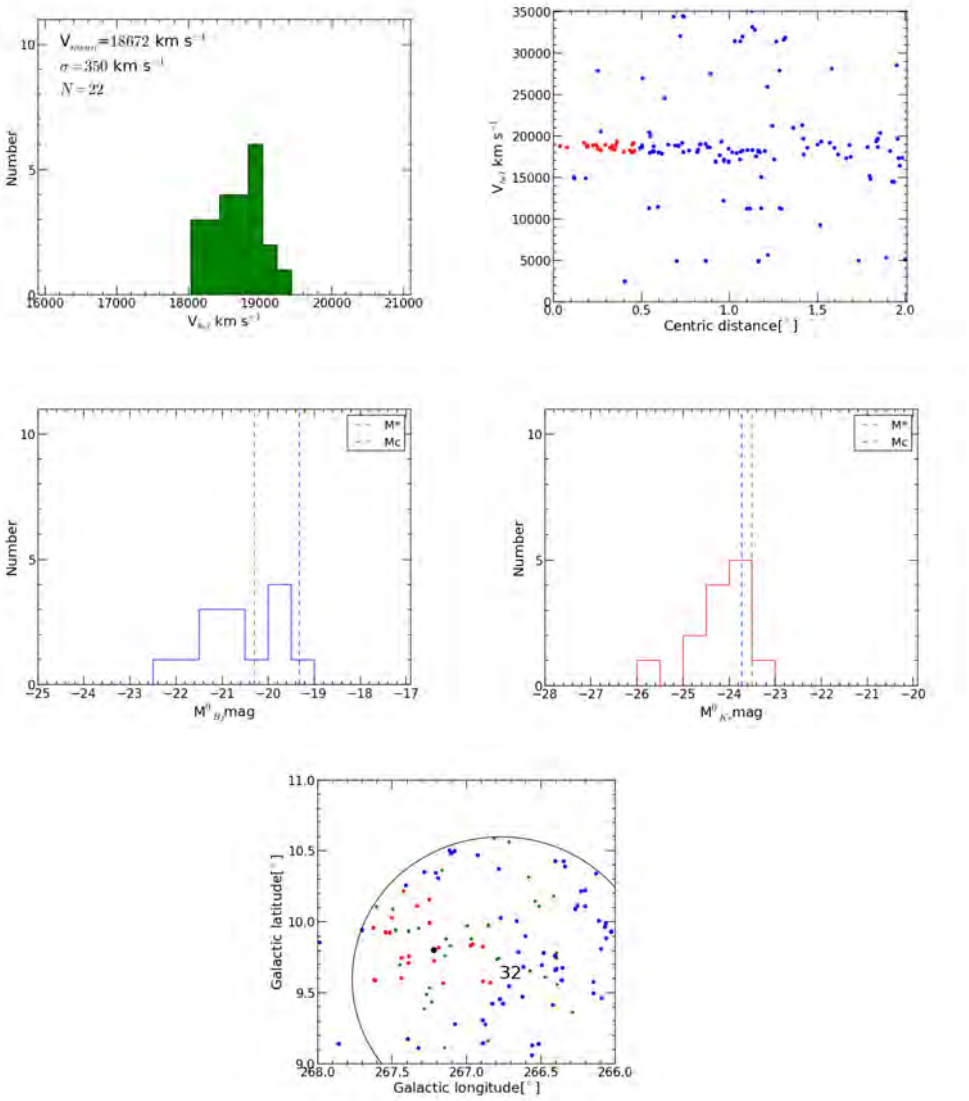

Figure C.9: From panel 1 this area has a velocity histogram that peaks around $\sim 19,000$ km s^{-1}. However, panel 2 shows a very little concentration near the centre. From this and the luminosity function, panel 3 and 4, this region is likely a weak cluster candidate with mass of $2.8 * 10^{14}$ M$_\odot$. This cluster is undersampled, as many galaxies that lie within one Abell radius from the centre of this candidate were not observed by our AAOmega observations.

VC10: $(l, b) = (271.67°, 7.71°)$, $(\alpha, \delta) = (147.38°, -43.84°)$, $E(B-V) = 0.21$

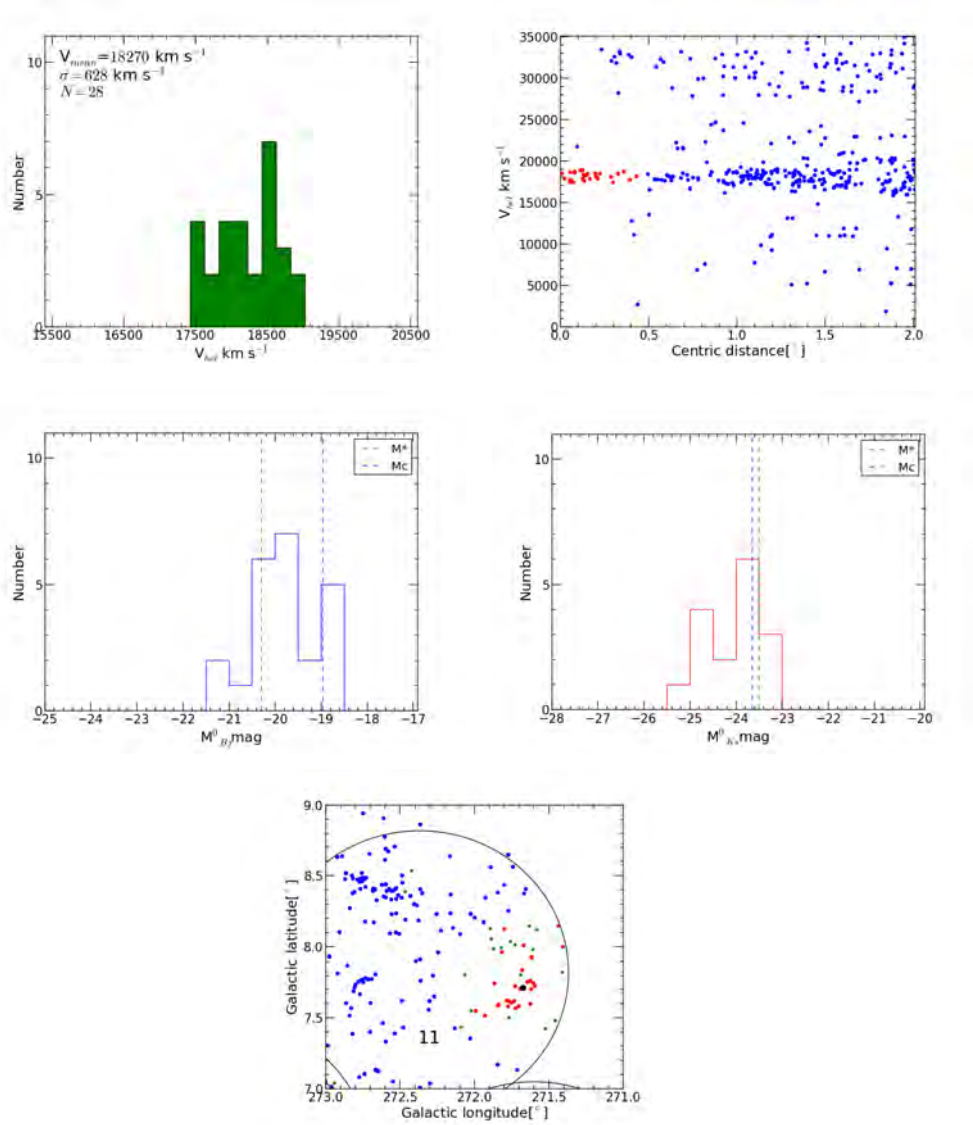

Figure C.10: From panel 1 this area has a velocity histogram that peaks around $\sim 18,500\,\mathrm{km\ s^{-1}}$. Panel 2 shows a very high concentration near the centre. From this and the luminosity function, panel 3 and 4, this region is a potential cluster candidate with mass of $8.87 * 10^{14}\,\mathrm{M_\odot}$.

VC11: $(l, b) = (272.62°, 8.41°)$, $(\alpha, \delta) = (149.0°, -43.89°)$, $E(B-V) = 0.20$

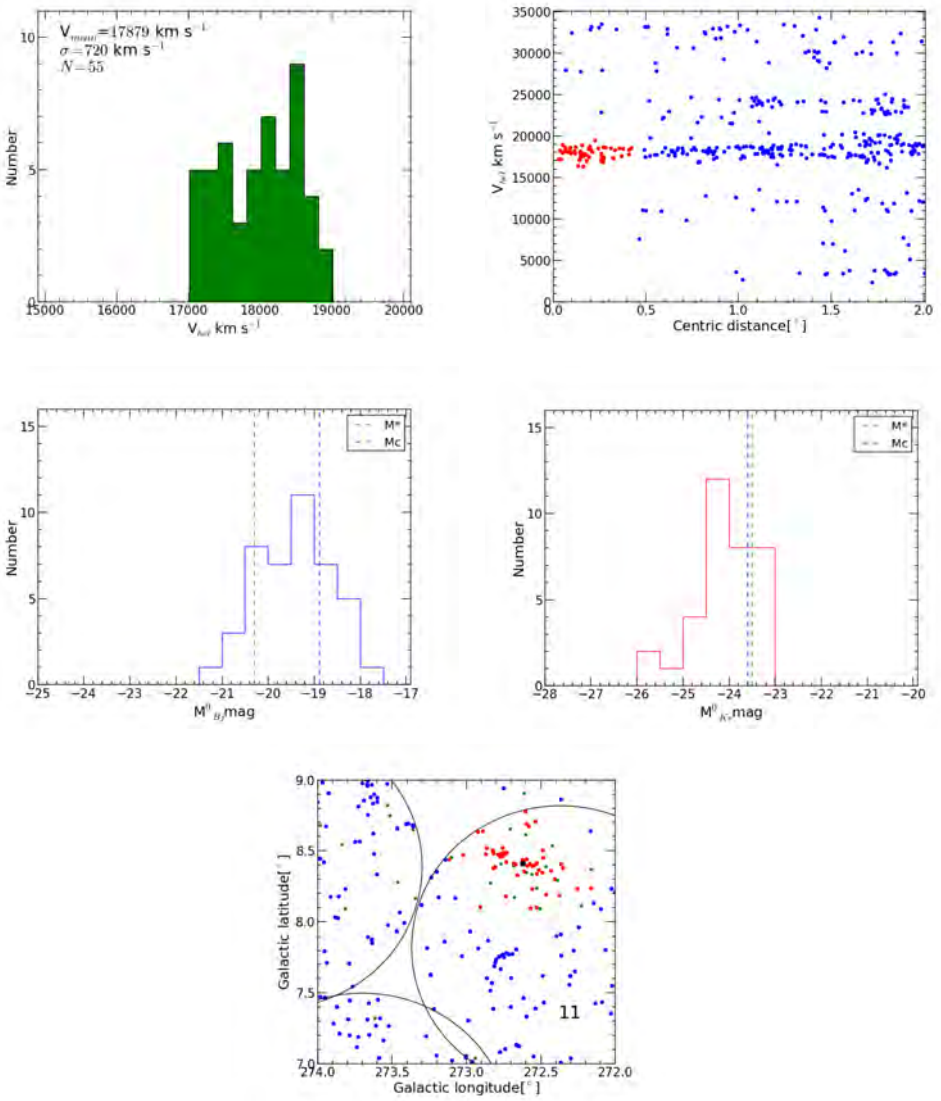

Figure C.11: From panel 1 this area has a gaussian velocity histogram with multi-peaks. Panel 2 shows a very high concentration near the centre. From this and the luminosity function, panel 3 and 4, it is clear that this region is a potential cluster candidate with mass of $1.178 * 10^{15}\,M_{\odot}$.

VC12: $(l, b) = (274.49°, 7.87°)$, $(\alpha, \delta) = (150.60°, -45.46°)$, $E(B-V) = 0.16$

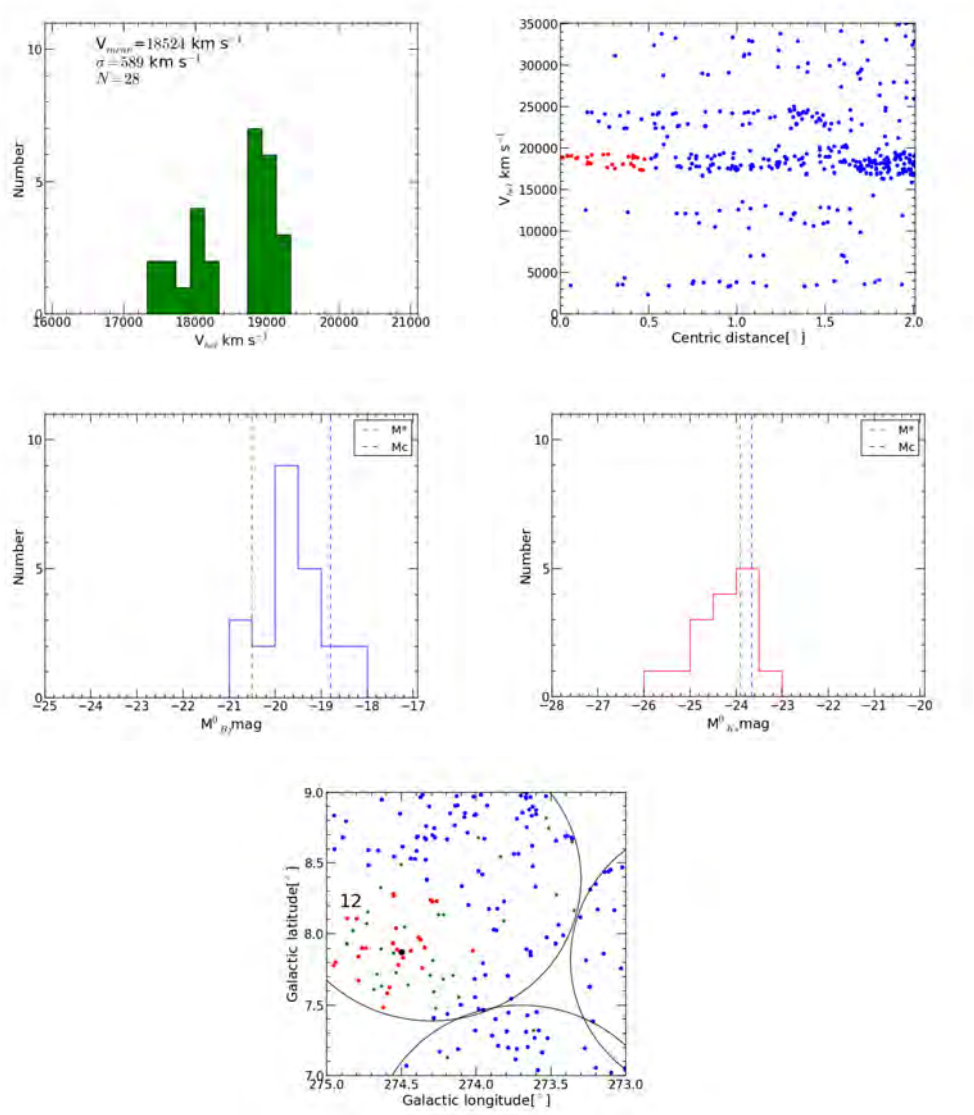

Figure C.12: From the velocity histogram peaks in panel 1, the relatively high number of galaxies around the centre in panel 2, 50% of the galaxies lie within 300 km s^{-1}, and the luminosity function, panel 3 and 4, this region is a potential cluster candidate with mass of $8.06 * 10^{14}$ $M_{\odot}$.

VC13: $(l, b) = (282.25°, 7.45°)$, $(\alpha, \delta) = (159.82°, -50.04°)$, $E(B-V) = 0.42$

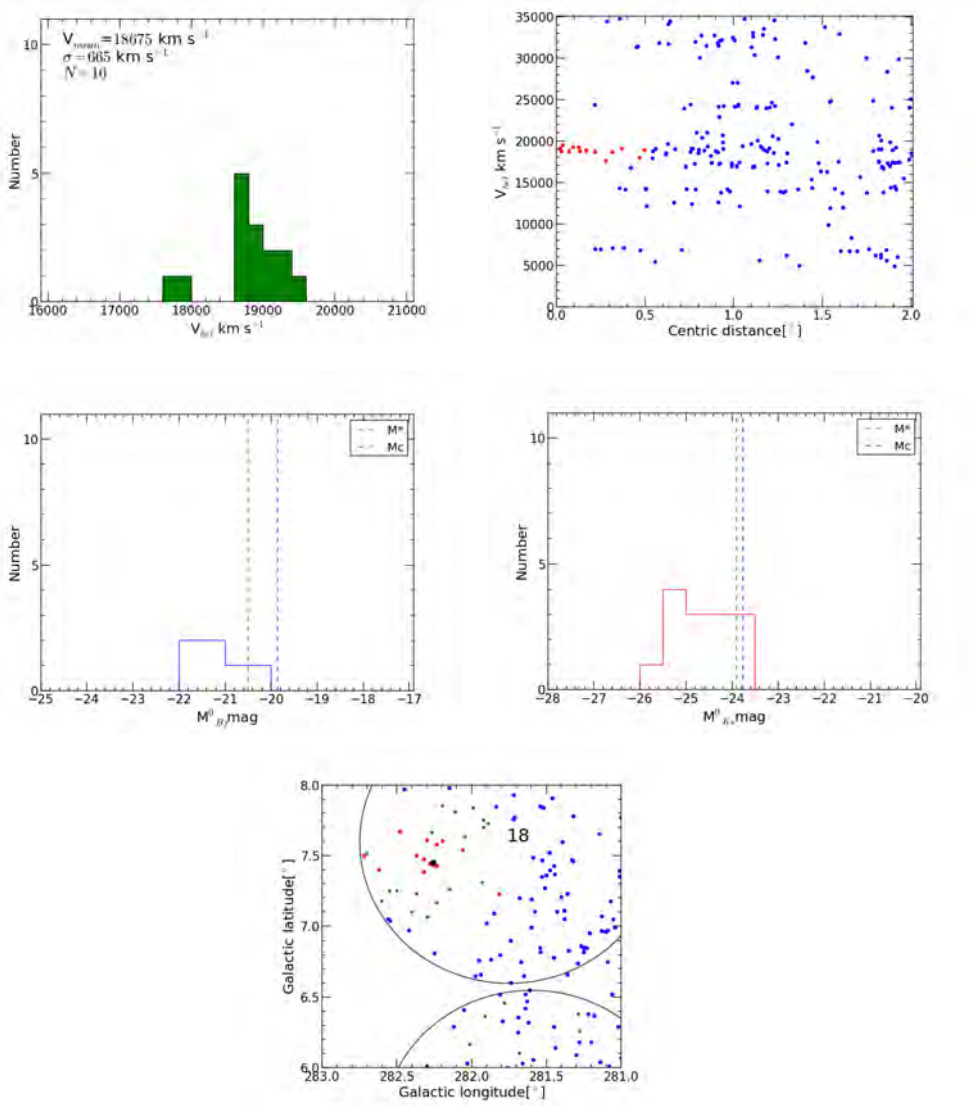

Figure C.13: From panel 1 this area has a velocity histogram that peaks around $\sim 19,000$ km s^{-1}. Panel 2 shows a very little concentration near the centre. From this and the luminosity function, panel 3 and 4, this region represents a weak cluster candidate with mass of $1.02 * 10^{15}$ M$_\odot$. This cluster candidate lies close to the border of the AAOmega field. Therefore, some galaxies that lie within one Abell radius from the centre of this candidate were not mapped.

Galaxy Groups Candidates:

VG01: $(l, b) = (248.68°, -8.26°)$, $(\alpha, \delta) = (112.44°, -35.46°)$, $E(B-V) = 0.28$

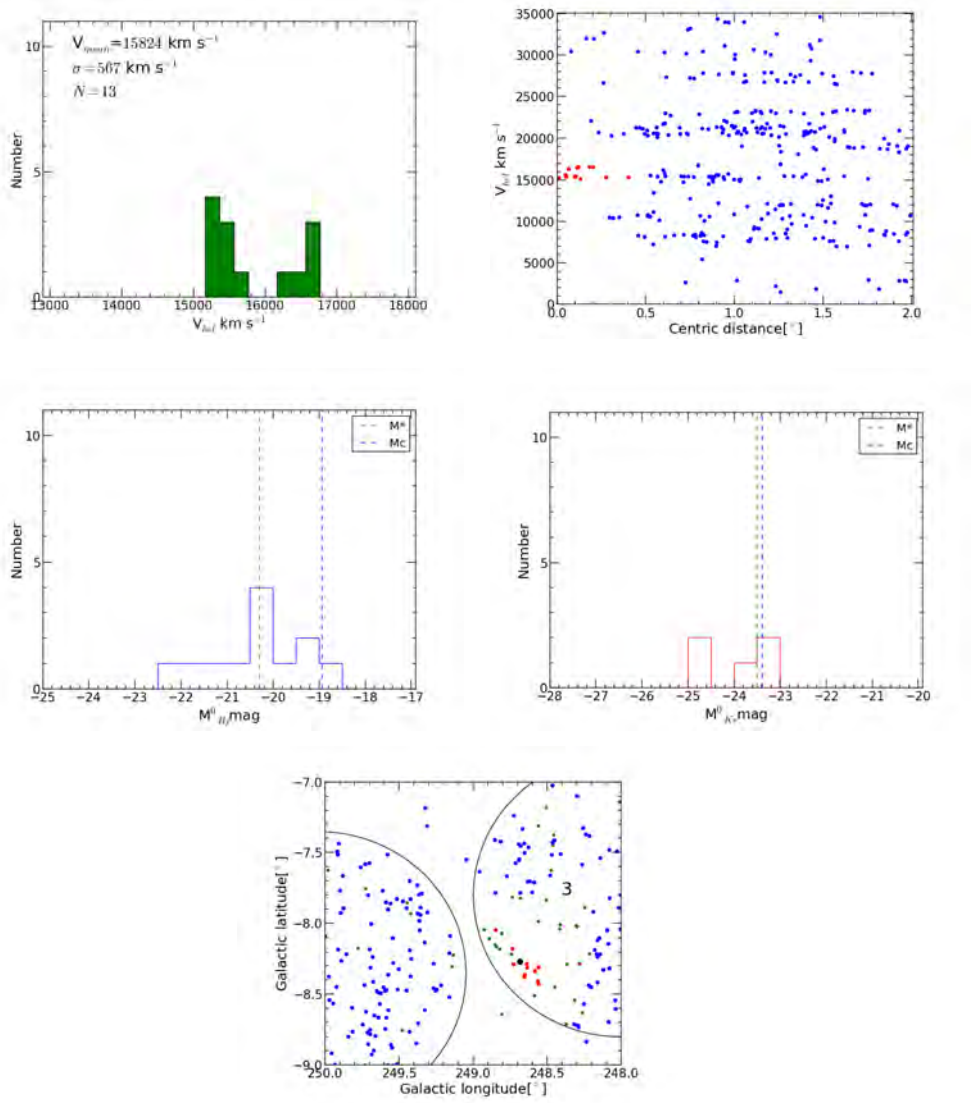

Figure C.14: Based on the relatively small multi-peaks around $\sim 15,500\,\mathrm{km\ s^{-1}}$ in panel 1, and the agglomeration of galaxies that appears from panel 2, this area is a weak group candidate. It has a mass of $7.473 * 10^{14}\,\mathrm{M}_{\odot}$.

VG02: $(l, b) = (247.93°, -7.40°)$, $(\alpha, \delta) = (112.96°, -34.40°)$, $E(B-V) = 0.30$

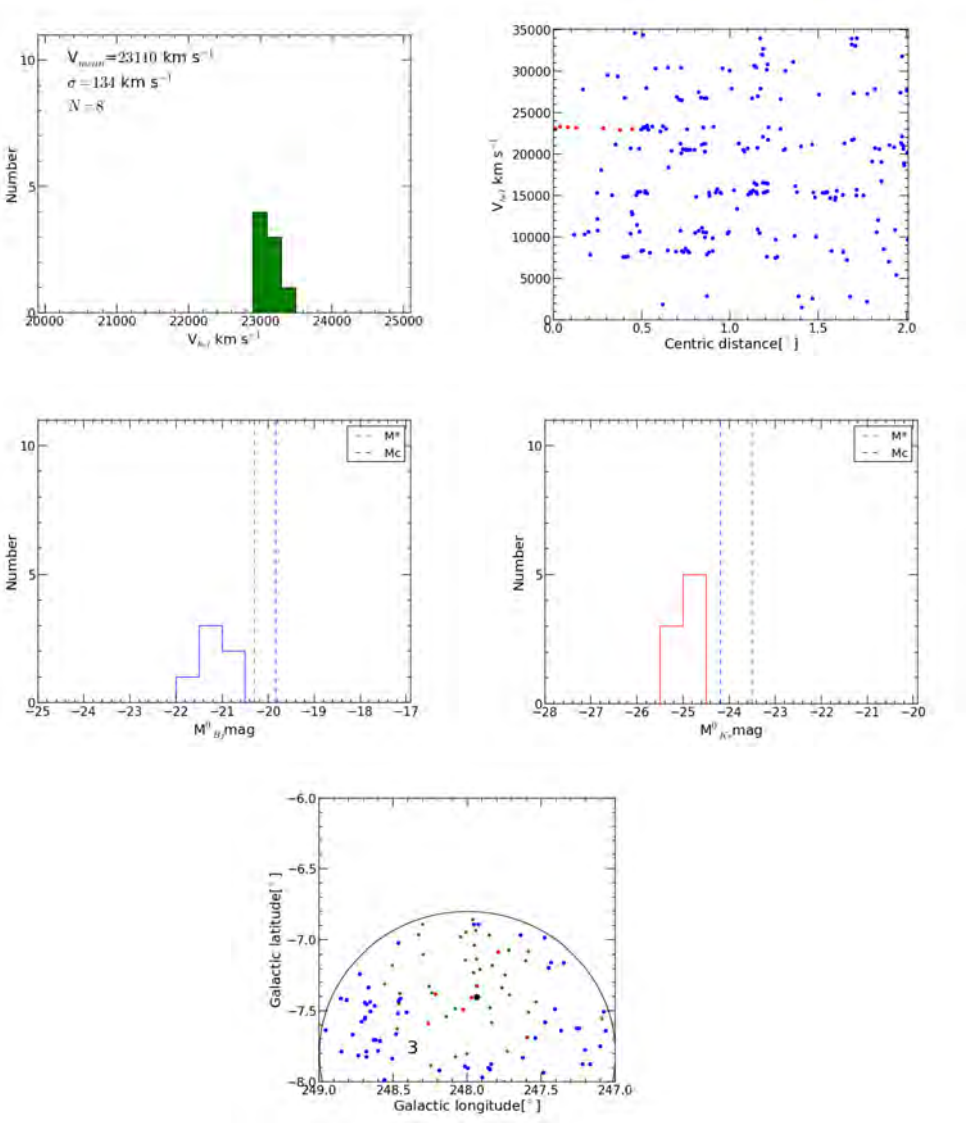

Figure C.15: Based on the small histogram shape that peaks around $\sim 23,000\,\mathrm{km\ s^{-1}}$ in panel 1, and the loose agglomeration of galaxies that appears from panel 2, this area is a weak galaxy group candidate. It has a mass of $0.41 * 10^{14}\,\mathrm{M}_{\odot}$. This group candidate is very undersampled, as most of the galaxies that lie within 1 Abell radius from the centre of this candidate were not observed by our AAOmega observations.

VG03: $(l, b) = (259.35°, -8.65°)$, $(\alpha, \delta) = (118.64°, -44.91°)$, $E(B-V) = 0.20$

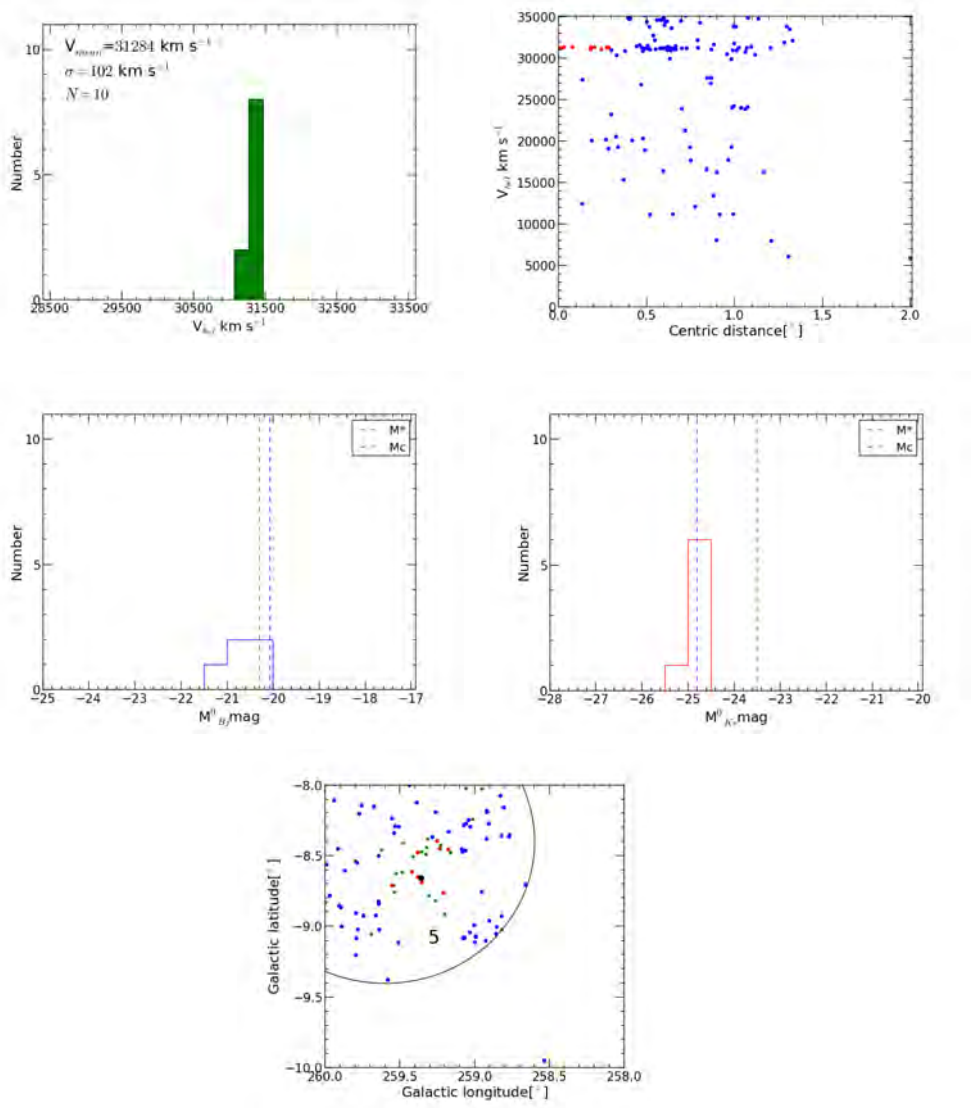

Figure C.16: Panel 1 shows very small histogram shape that peaks around $\sim 31,300\,\mathrm{km\ s^{-1}}$, connecting this shape to panel 2 it becomes clear that most of the galaxies are within relatively small distance from the chosen centre. This region is a weak group candidate, and it has a mass of $1.73 * 10^{14}\,\mathrm{M}_{\odot}$.

VG04: $(l, b) = (263.67°, -9.74°)$, $(\alpha, \delta) = (120.41°, -49.14°)$, $E(B-V) = 0.20$

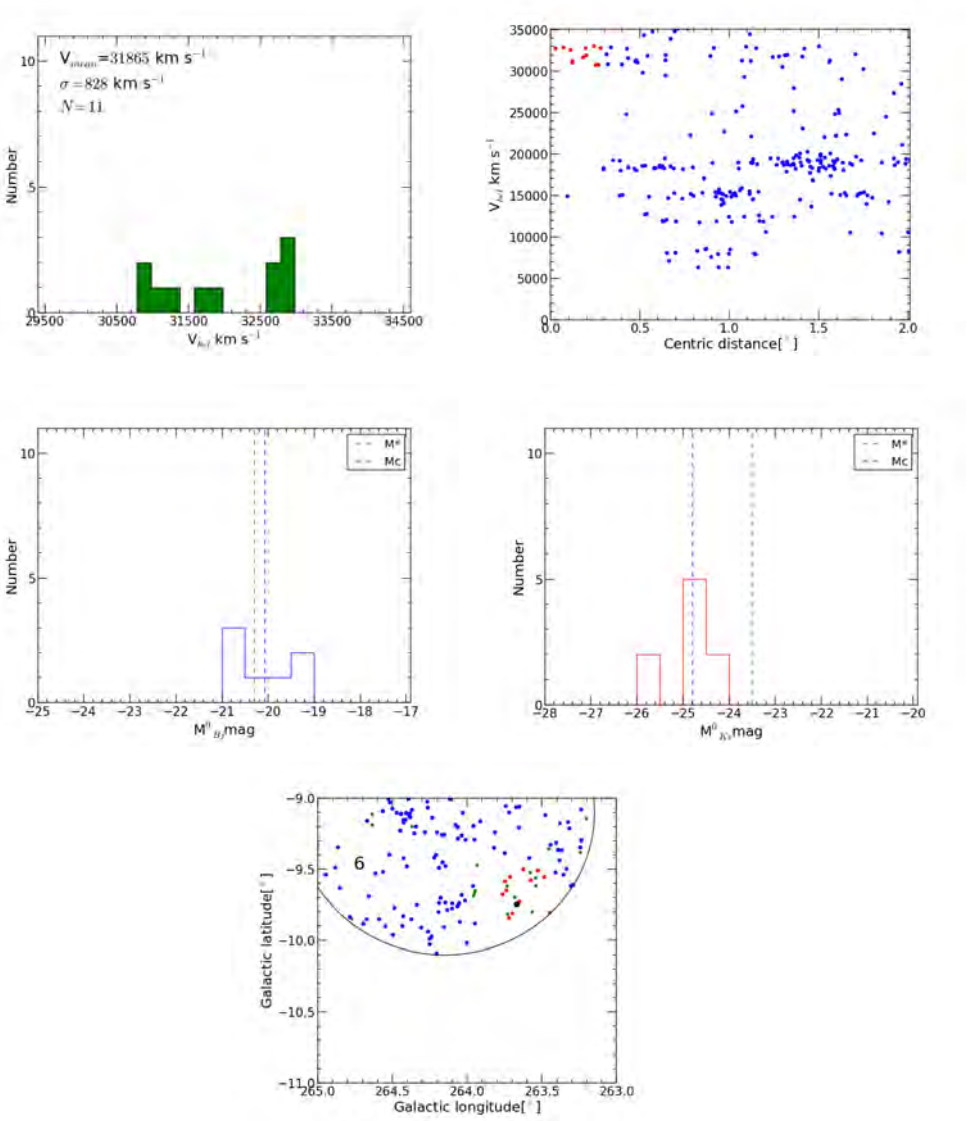

Figure C.17: Based on the velocity distribution, and the loose concentration around the centre (panel 2) this region is a potential group candidate. It has a mass of $1.58 * 10^{15}\,M_{\odot}$.

VG05: $(l, b) = (264.38°, -9.11°)$, $(\alpha, \delta) = (121.79°, -49.42°)$, $E(B-V) = 0.24$

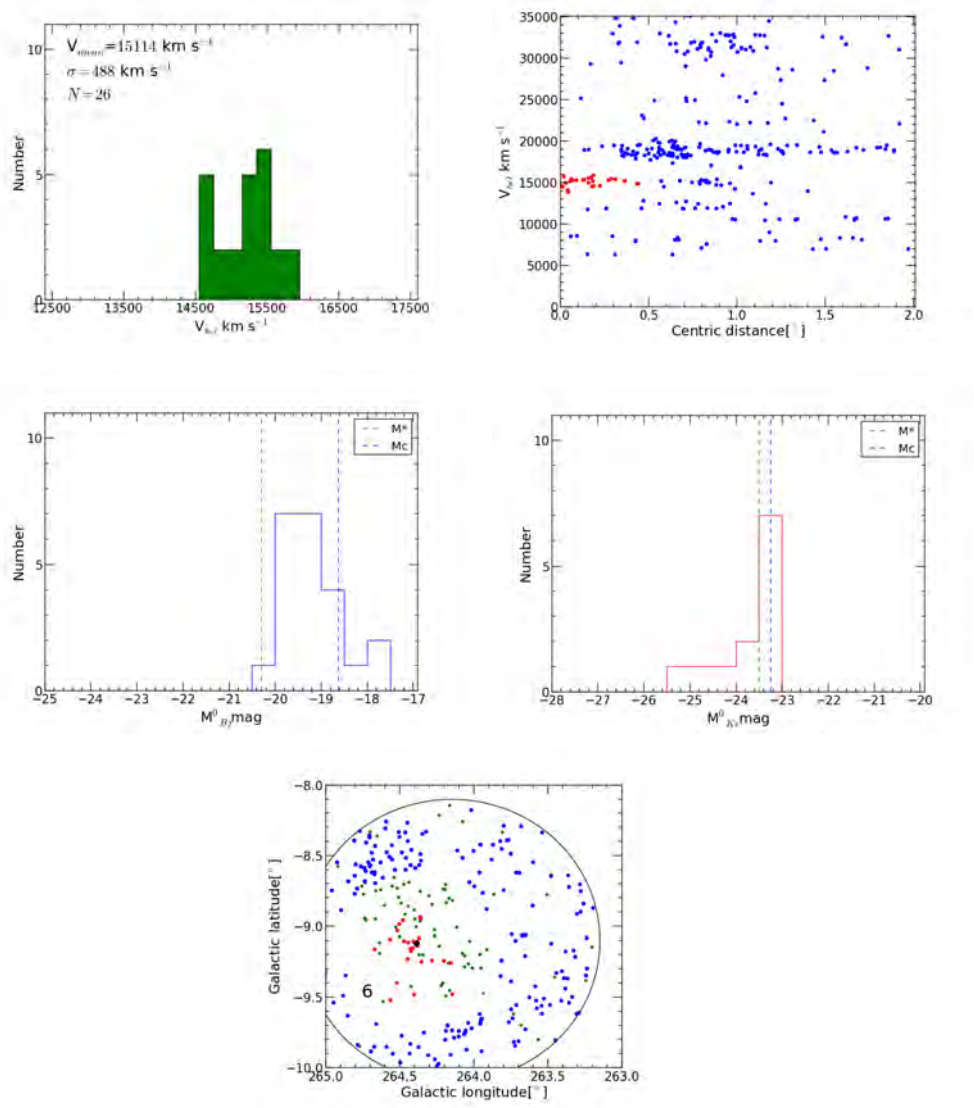

Figure C.18: Despite the high histogram peak around $15,000\,\mathrm{km\ s^{-1}}$, this region is a massive group with mass equals $5.53 * 10^{14}\,\mathrm{M}_{\odot}$. This is based upon the luminosity function, panel 3 and 4, where only one galaxy has $M^0_{BJ} \lesssim -20^m.0$.

VG06: $(l, b) = (276.92°, -9.70°)$, $(\alpha, \delta) = (133.29°, -59.91°)$, $E(B-V) = 0.15$

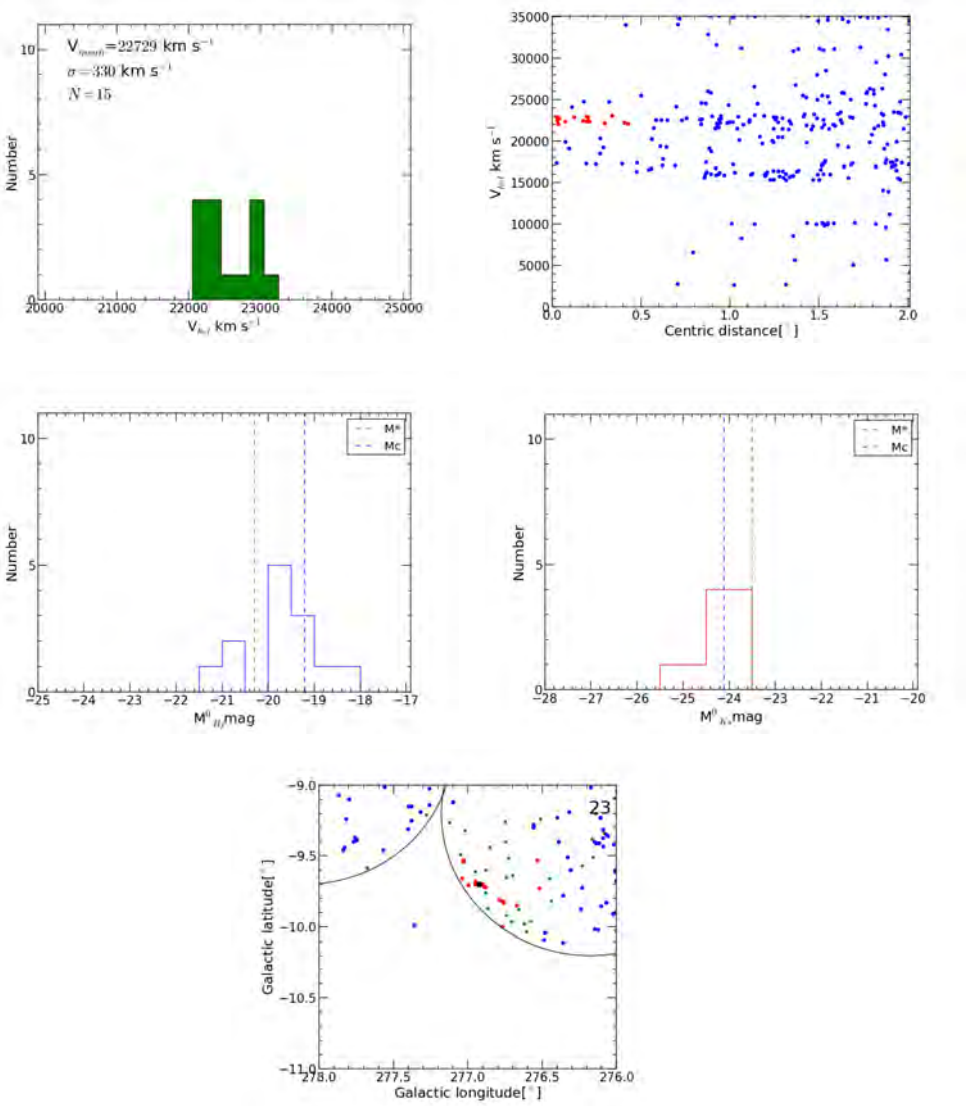

Figure C.19: Based on the velocity distribution in panel 1, and the agglomeration of galaxies that appears from panel 2, this region is likely galaxy group candidate. It has a mass of $2.25 * 10^{14}\,M_{\odot}$.

VG07: $(l, b) = (262.69°, 6.94°)$, $(\alpha, \delta) = (138.10°, -38.25°)$, $E(B-V) = 0.30$

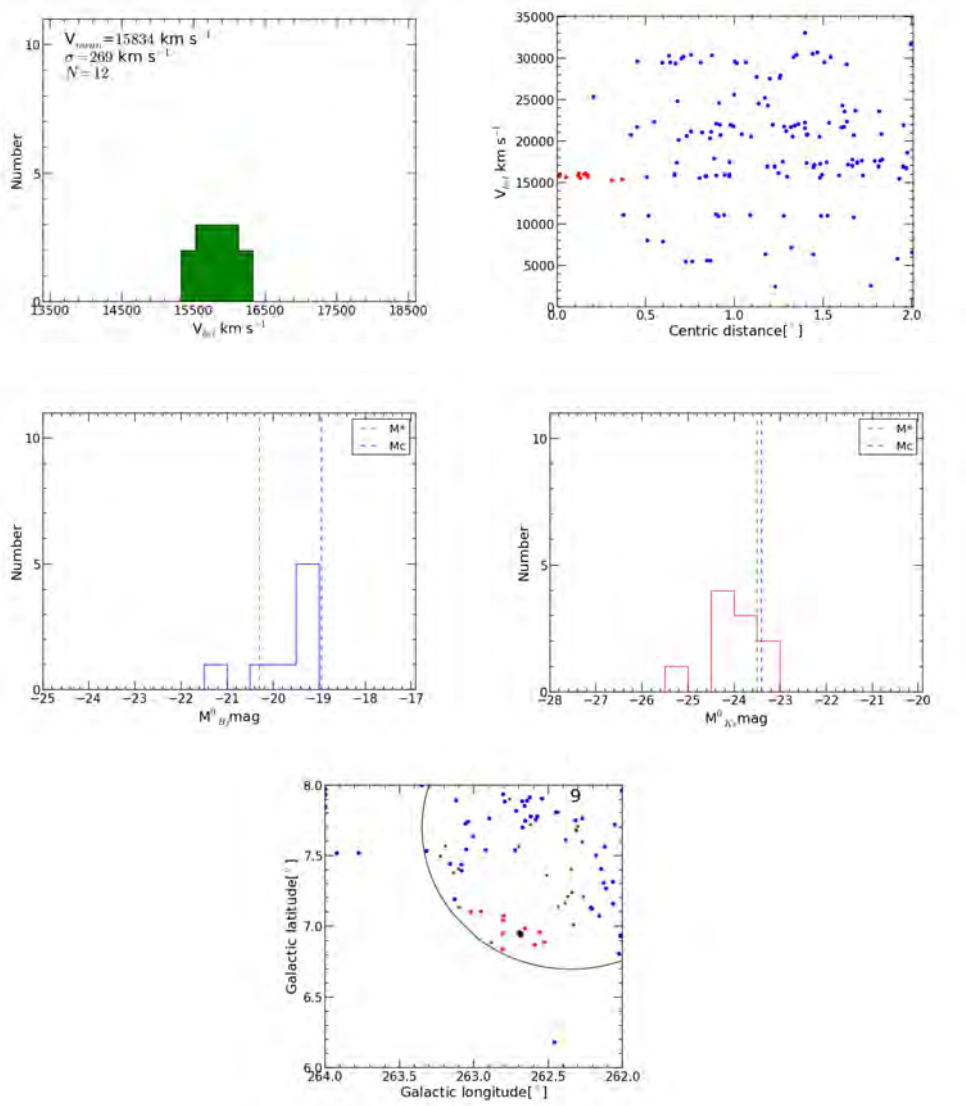

Figure C.20: This region is a group of galaxies with mass $1.68 * 10^{14}\,M_{\odot}$. Based upon the relatively broad velocity distribution shape in panel 1 around $\sim 16,000\,\mathrm{km\ s^{-1}}$, and the concentrated centre (panel 2).

VG08: $(l, b) = (265.55°, 7.43°)$, $(\alpha, \delta) = (141.12°, -39.97°)$, $E(B-V) = 0.30$

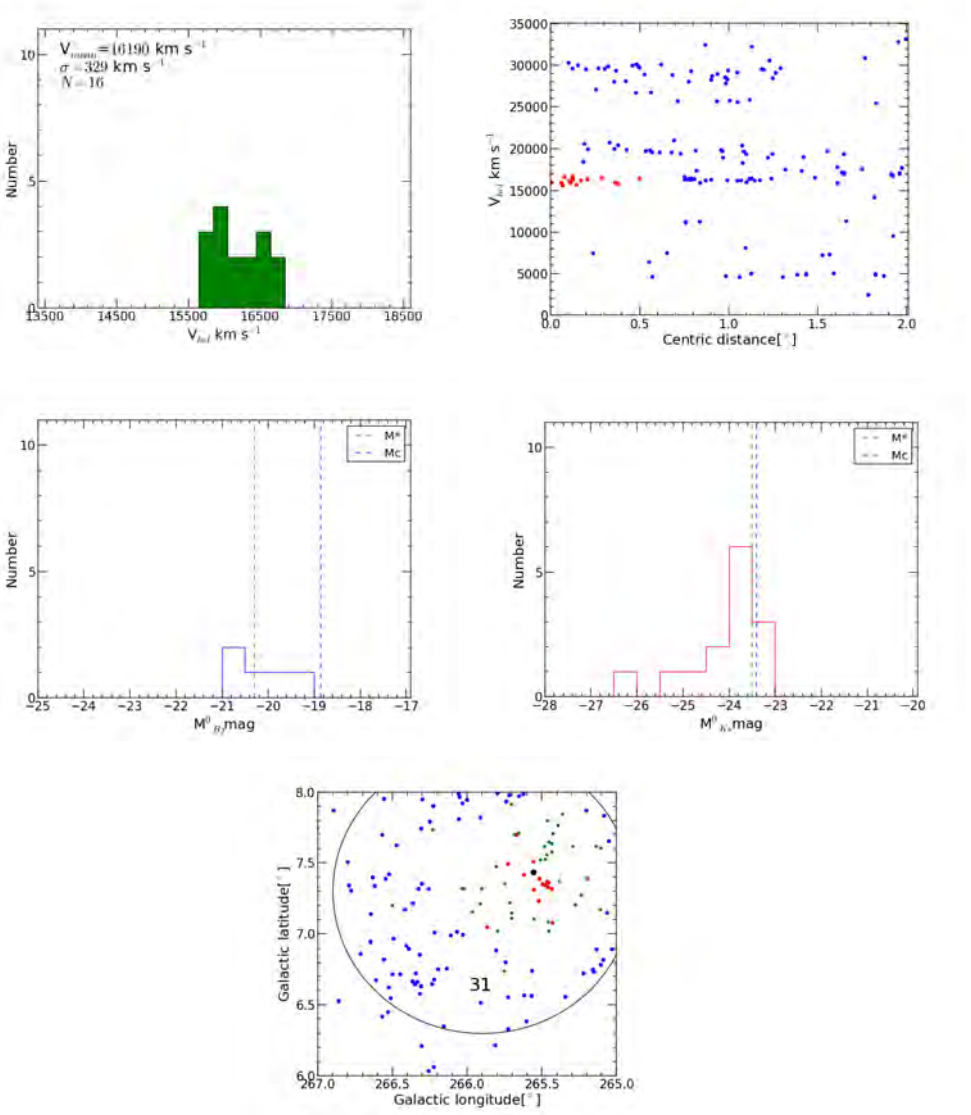

Figure C.21: From the broad velocity distribution shape in panel 1 $\sim 16,000\,\mathrm{km\ s^{-1}}$, and the concentration around the centre appearing in panel 2, there are 10 galaxies within $300\,\mathrm{km\ s^{-1}}$ from the centre, this region is likely a galaxy group candidate with mass equals $2.51 * 10^{14}\,\mathrm{M_\odot}$.

VG09: $(l, b) = (280.01°, -7.20°)$, $(\alpha, \delta) = (141.15°, -60.51°)$, $E(B-V) = 0.24$

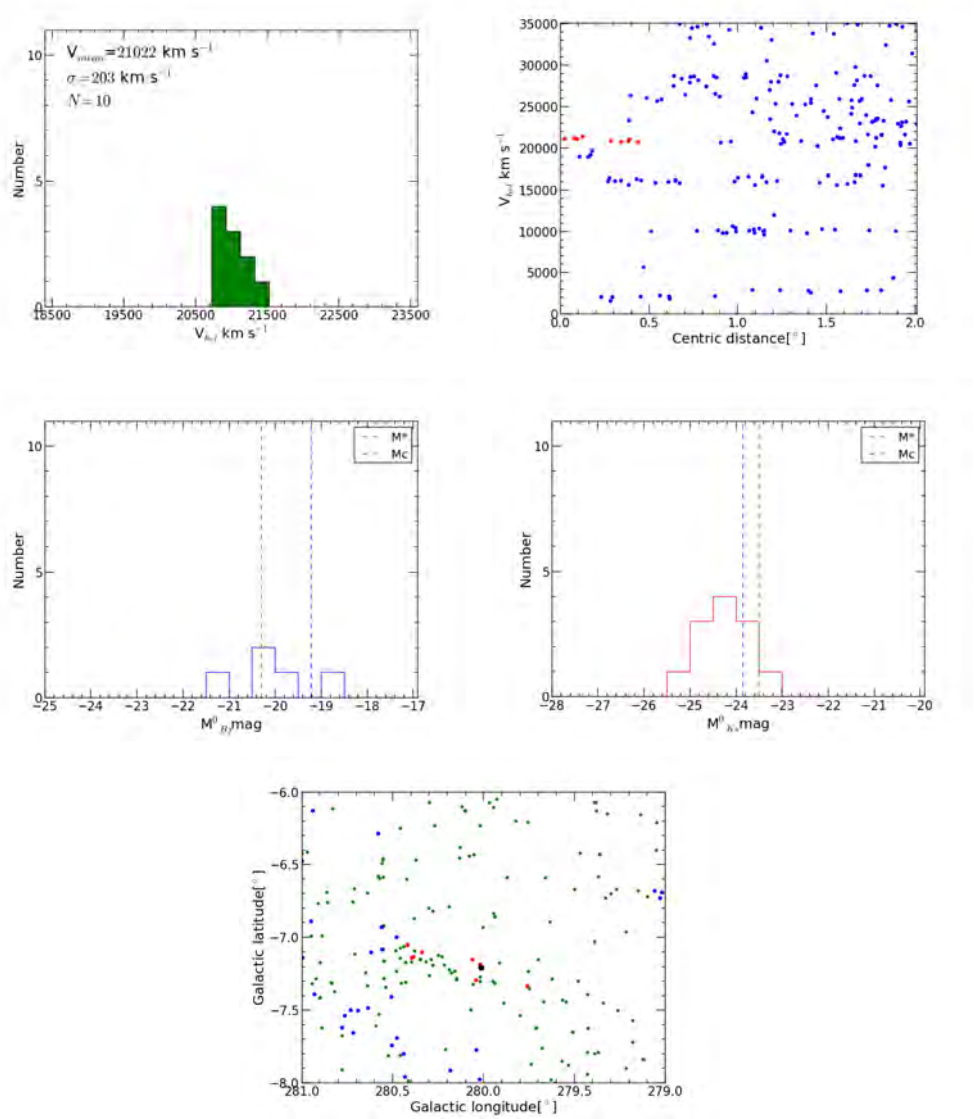

Figure C.22: This region is a weak group candidate with a mass of $0.94 * 10^{14}\,M_{\odot}$. This decision is based upon the velocity distribution in panel 1, the agglomeration of galaxies in the centric velocity distribution (panel 2), where there are 5 galaxies within a distance less than 300 km s^{-1}.

VG10: $(l, b) = (271.10°, 5.60°)$, $(\alpha, \delta) = (144.85°, -45.07°)$, $E(B-V) = 0.42$

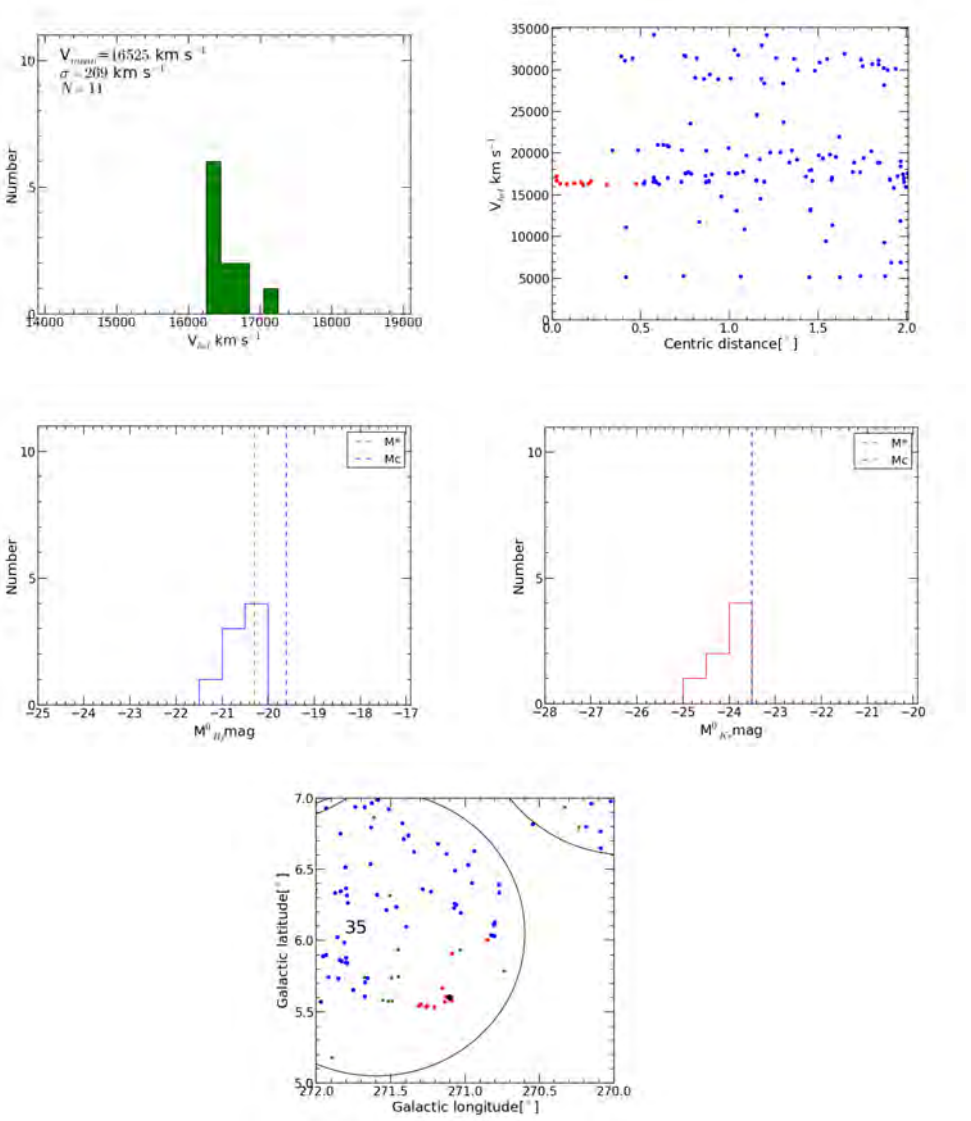

Figure C.23: This region is likely a weak group candidate with a mass of $1.69 * 10^{14}\,M_{\odot}$. I conclude this from the velocity histogram peak in panel 1, and the relative concentration around the chosen centre that appears in panel 2.

VG11: $(l, b) = (282.03°, -5.65°)$, $(\alpha, \delta) = (146.29°, -60.73°)$, $E(B-V) = 0.40$

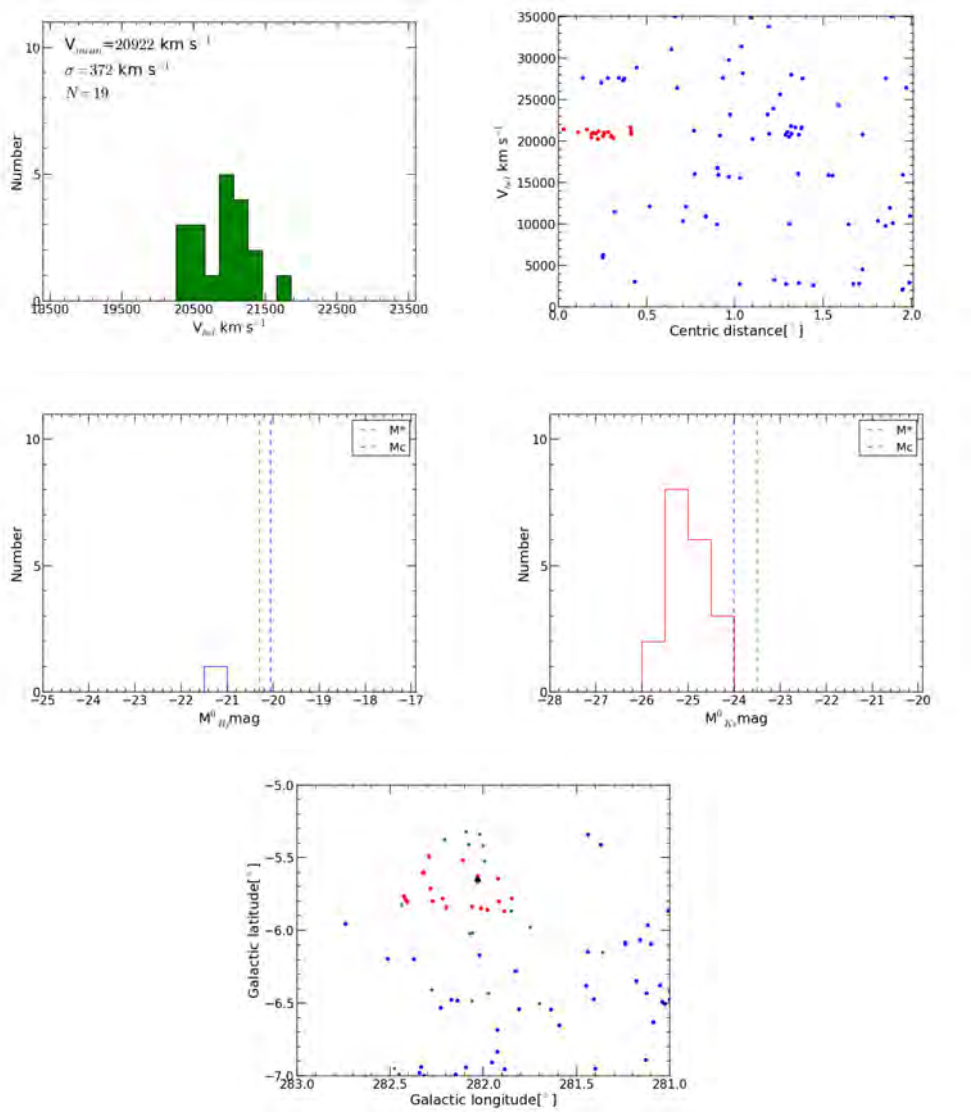

Figure C.24: From the peak in the velocity distribution of galaxies in panel 1 at $\sim 21,100$ km s^{-1}, and the relative concentration close to the centre (in panel 2), this region is thus a potential group candidate with mass equals $3.18 * 10^{14}\,M_{\odot}$.

VG12: $(l, b) = (270.30°, 8.43°)$, $(\alpha, \delta) = (146.59°, -42.41°)$, $E(B-V) = 0.42$

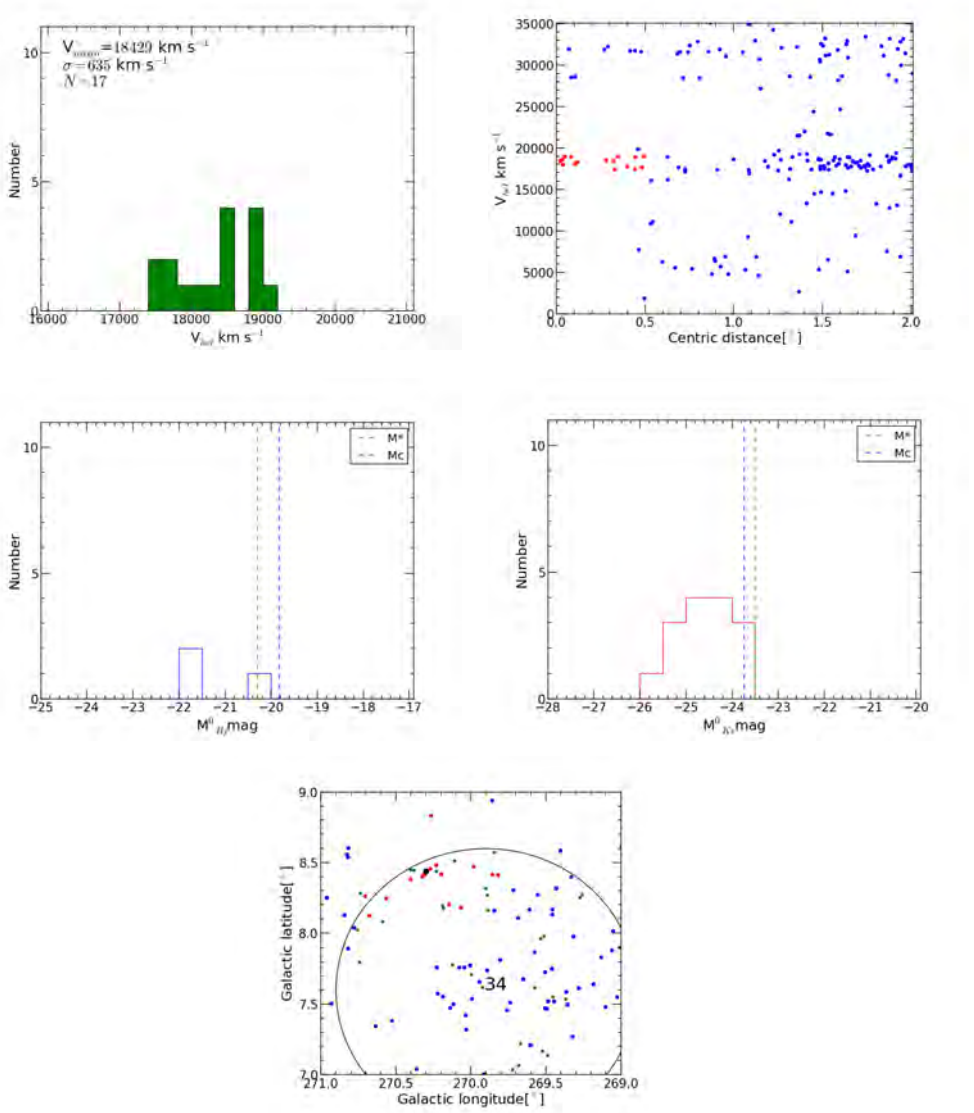

Figure C.25: This region is likely a potential galaxy group. It has a mass of $9.37 * 10^{14}\,M_{\odot}$. This decision is based upon the velocity distribution in panel 1, the agglomeration of galaxies in the group-centric velocity distribution (panel 2), where there are 5 galaxies within a distance less than 300 km s^{-1}.

VG13: $(l, b) = (272.85°, 6.70°)$, $(\alpha, \delta) = (147.74°, -45.36°)$, $E(B-V) = 0.16$

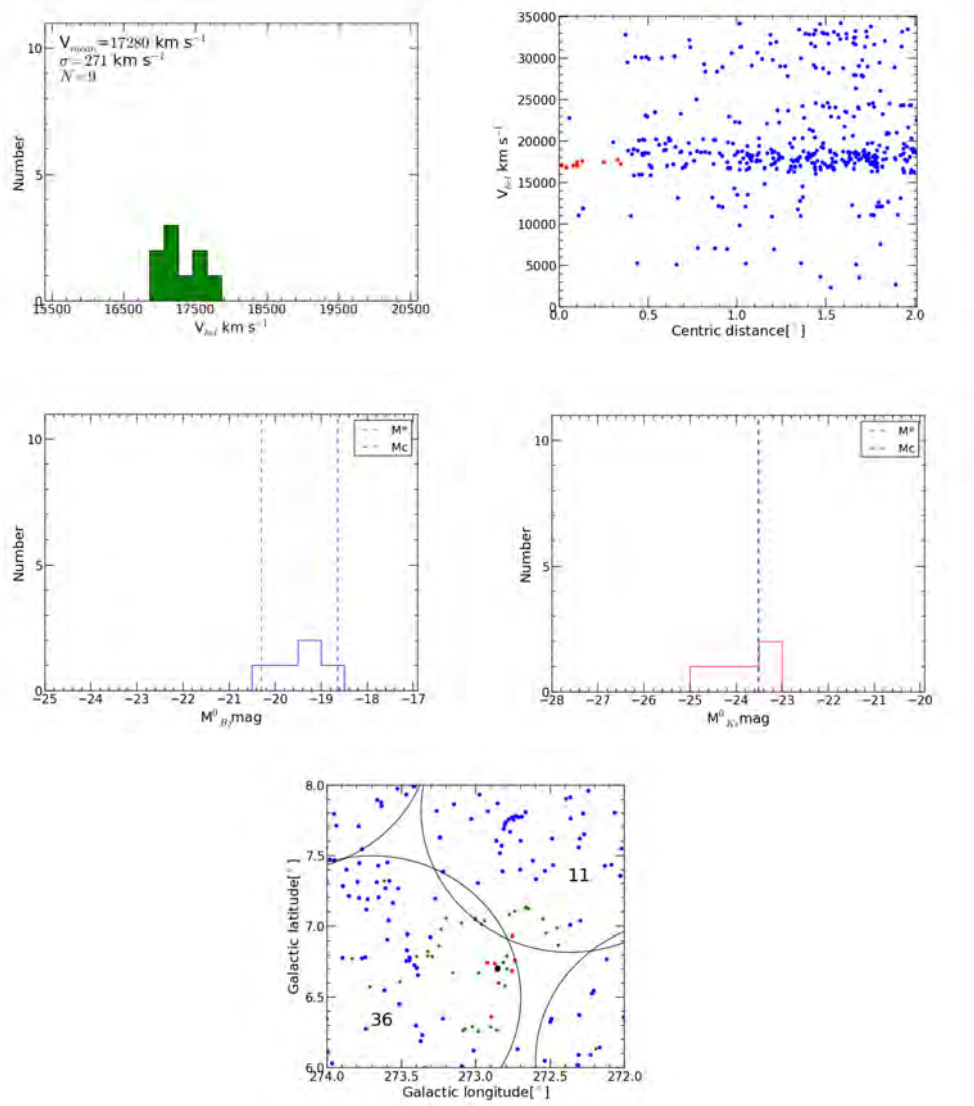

Figure C.26: From the velocity histogram (panel 1), the centric velocity distribution (panel 2), this region is a weak galaxy group candidate. It has a mass of $1.70 * 10^{14}\,M_{\odot}$.

VG14: $(l, b) = (273.42°, 6.73°)$, $(\alpha, \delta) = (148.40°, -45.70°)$, $E(B-V) = 0.18$

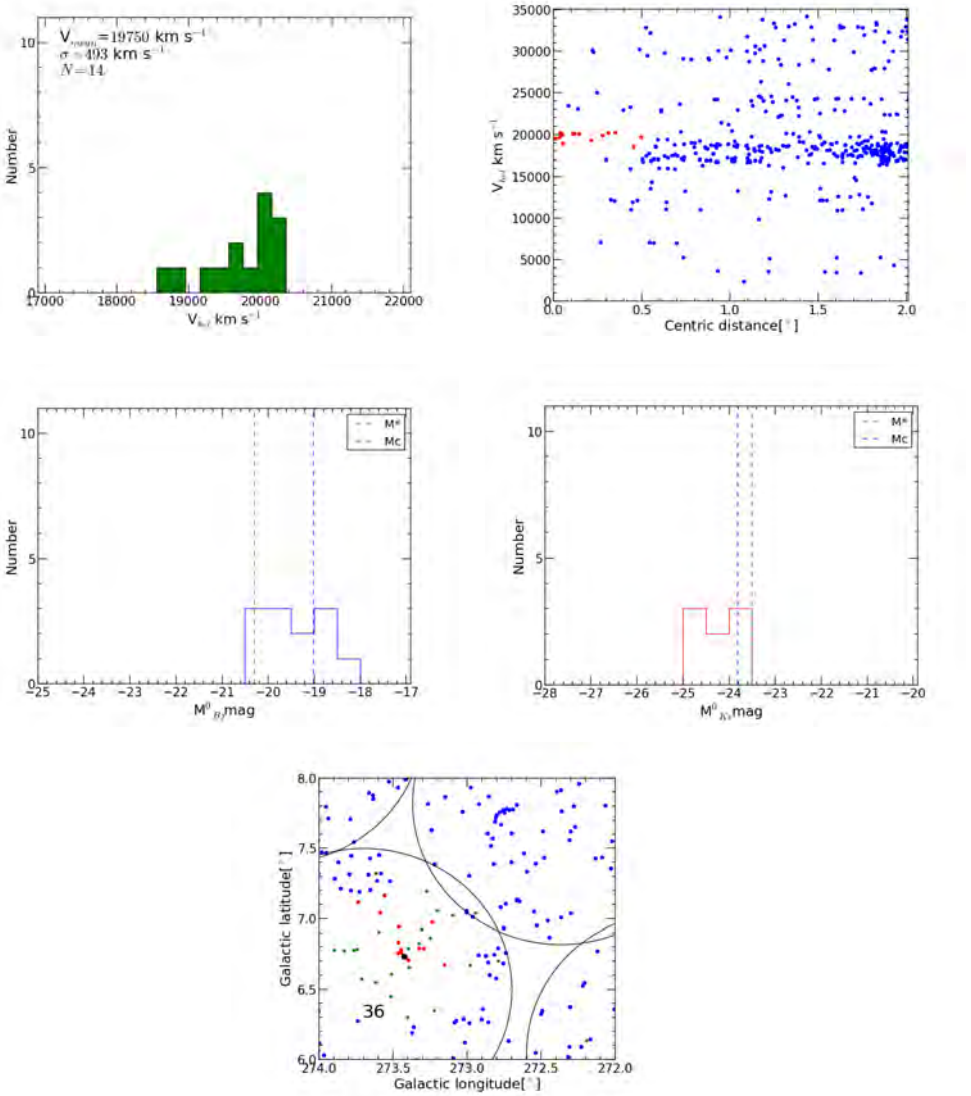

Figure C.27: Panel 1 shows small multi-peaks around $\sim 20,000\,\mathrm{km\ s^{-1}}$, connecting this shape to panel 2 it becomes clear that most of the galaxies are within relatively small distance from the chosen centre. Therefore, this region is a potential galaxy group. It has a mass of $5.64 * 10^{14}\,\mathrm{M}_{\odot}$.

VG15: $(l, b) = (276.53°, 4.61°)$, $(\alpha, \delta) = (150.07°, -49.27°)$, $E(B-V) = 0.43$

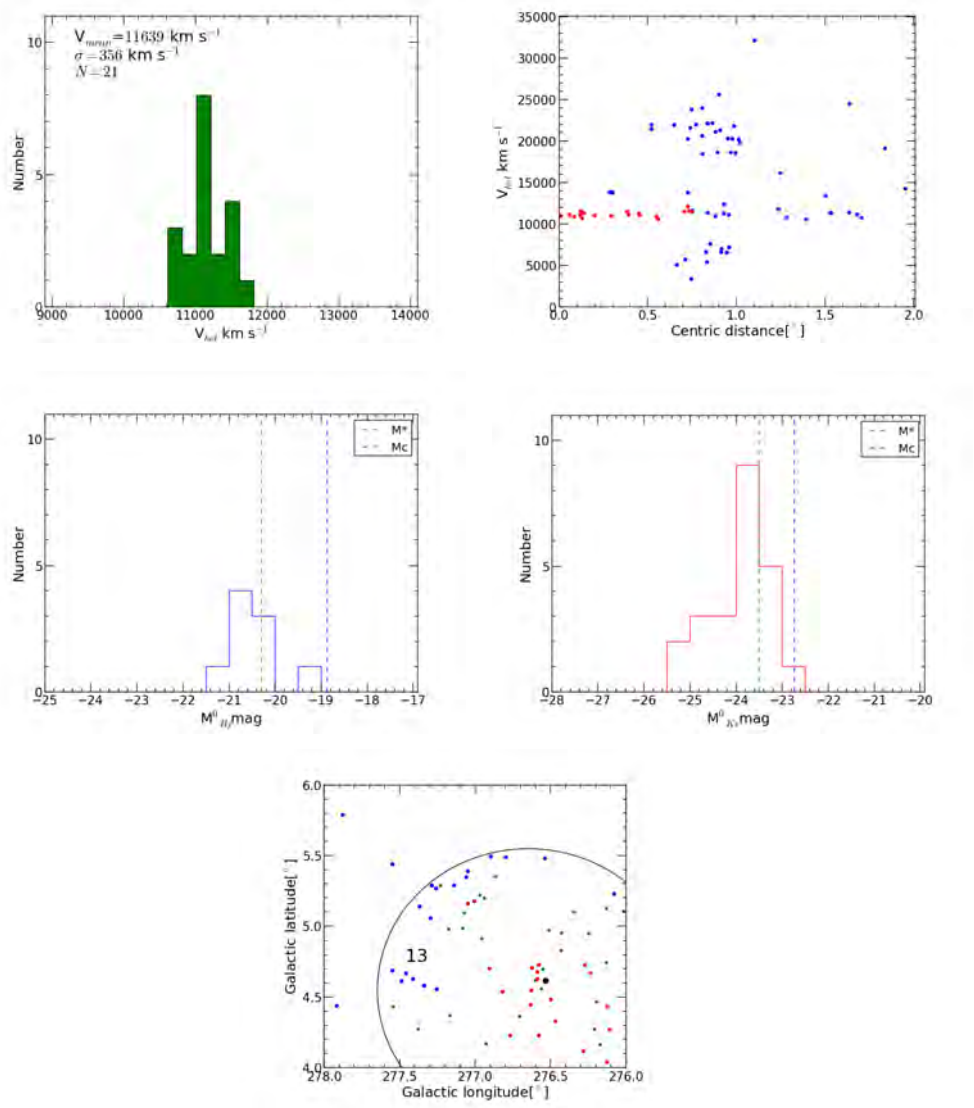

Figure C.28: This region is a group of galaxies with mass $2.94 * 10^{14}\,M_{\odot}$. Based upon the relatively broad shape in panel 1 around $\sim 11,000\,\mathrm{km\ s^{-1}}$, and the relatively high concentrated centre (panel 2).

VG16: $(l, b) = (273.71°, 8.85°)$, $(\alpha, \delta) = (150.56°, -44.20°)$, $E(B-V) = 0.14$

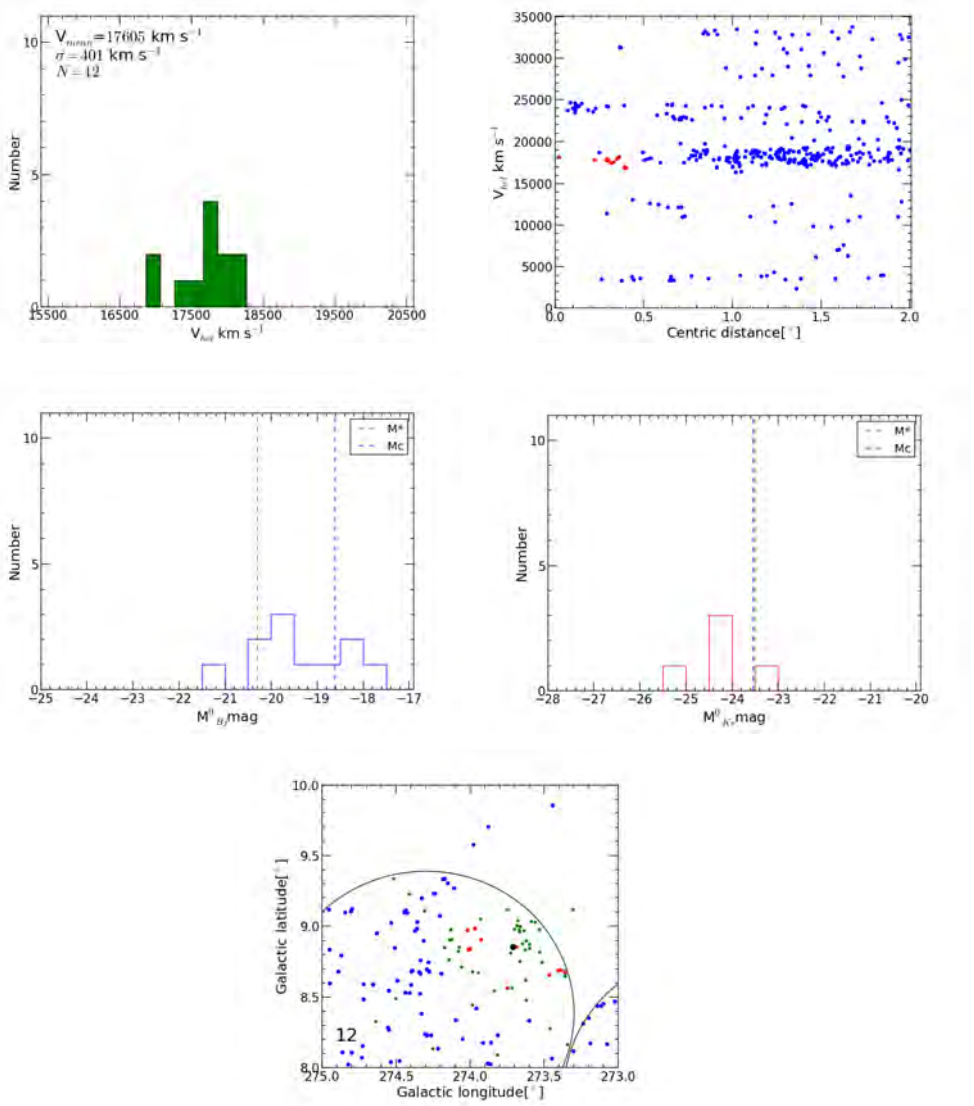

Figure C.29: From the velocity distribution of the galaxies in panel 1, and the luminosity function in panel 3 and 4, this region is a weak galaxy group candidate. It has a mass of $3.73 * 10^{14}\,M_{\odot}$. This group candidate lies at the border of our AAOmega observation field. Thus most of the galaxies that lie within 1 Abell radius from the centre of this candidate were not observed.

VG17: $(l, b) = (286.71°, -7.46°)$, $(\alpha, \delta) = (151.85°, -65.03°)$, $E(B-V) = 0.20$

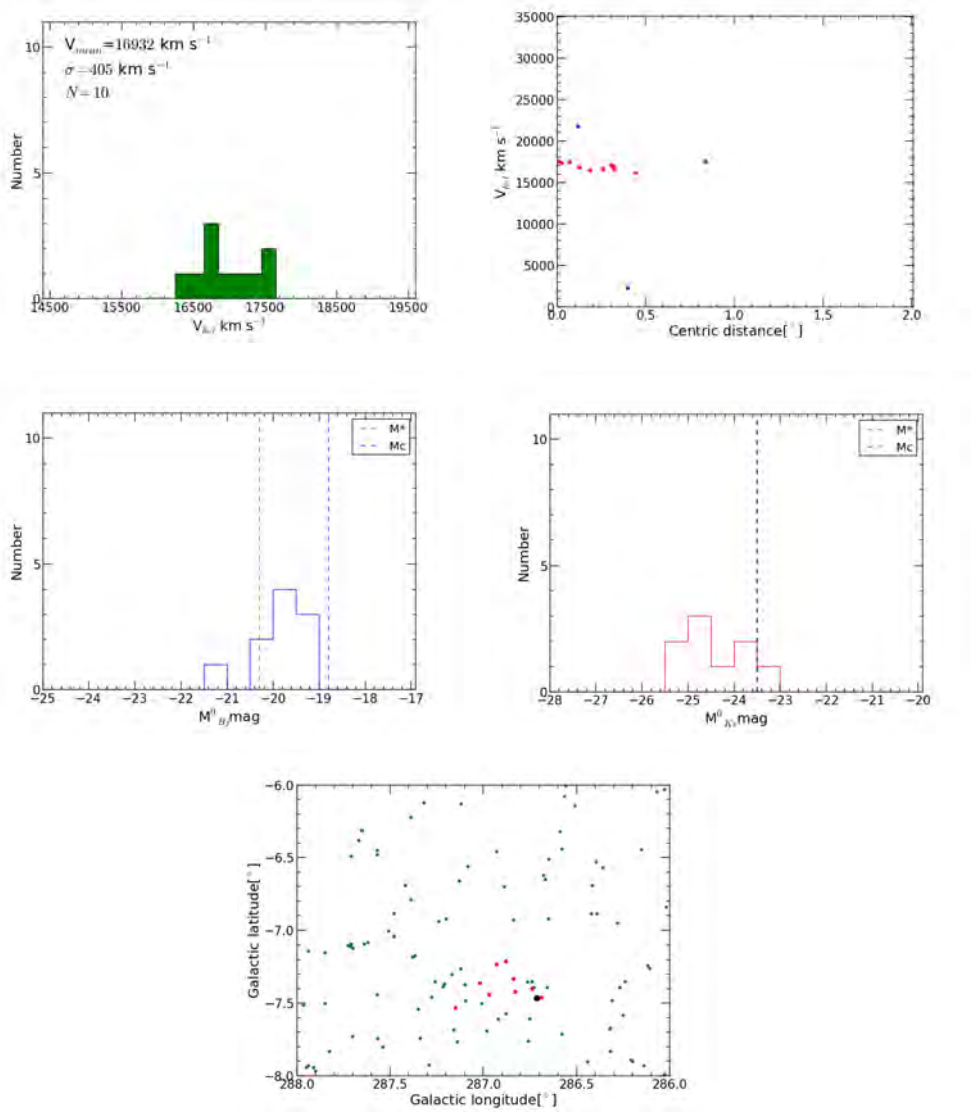

Figure C.30: Based on the velocity distribution of the galaxies in panel 1, and the luminosity function in panel 3 and 4, this region is a weak galaxy group candidate. It has a mass of $3.8 * 10^{14}\,\mathrm{M}_{\odot}$. This group candidate is very undersampled, as it was observed using SALT, which is known to have small FOV $8' \times 8'$ on the sky.

VG18: $(l, b) = (275.01°, 8.68°)$, $(\alpha, \delta) = (151.87°, -45.12°)$, $E(B-V) = 0.13$

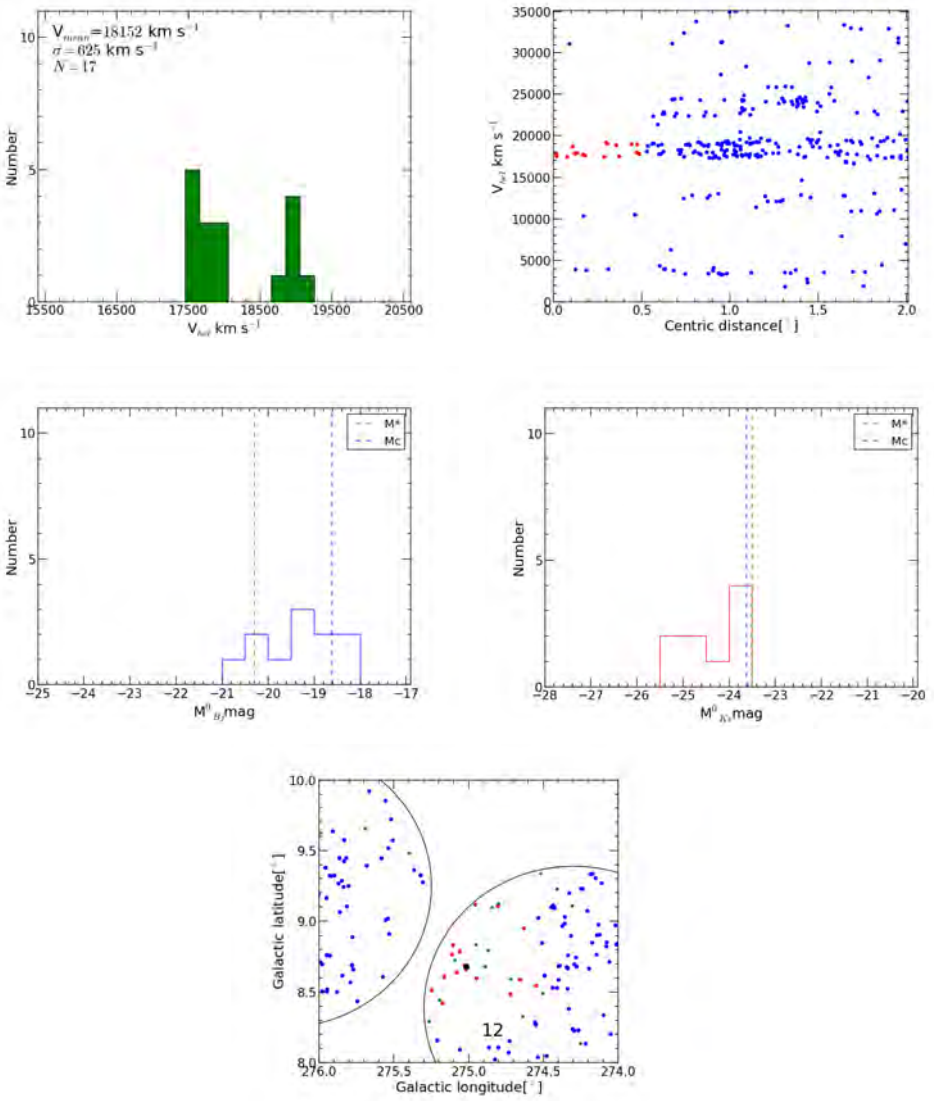

Figure C.31: From the two histogram peaks in panel 1, appearing at ($\sim 17,500\,\mathrm{km\ s^{-1}}$, $\sim 19,000\,\mathrm{km\ s^{-1}}$), and the luminosity function in panel 3 and 4, this region is a potential galaxy group. This group has a mass of $9.08 * 10^{14}\,\mathrm{M}_{\odot}$.

VG19: $(l, b) = (276.17°, 8.69°)$, $(\alpha, \delta) = (153.21°, -45.77°)$, $E(B-V) = 0.16$

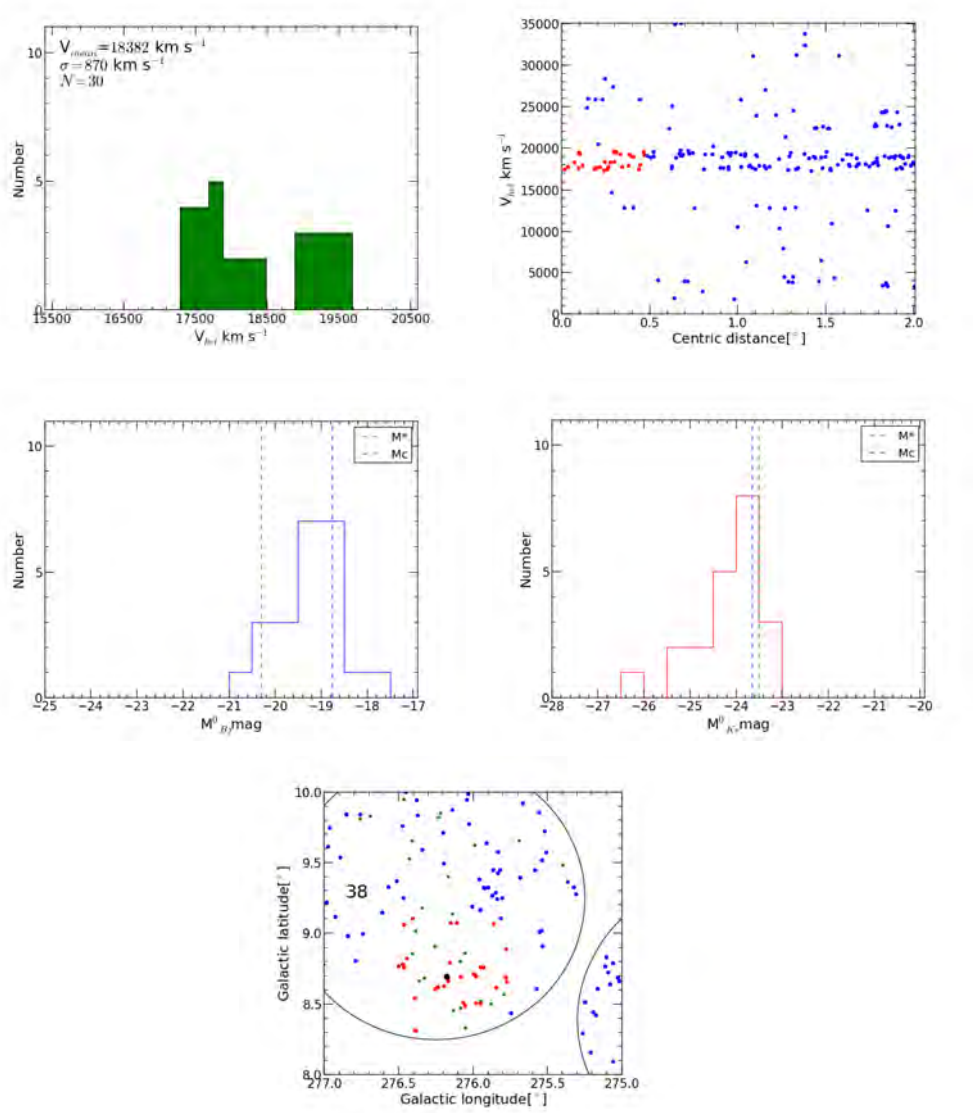

Figure C.32: Despite the high concentration of galaxies around the centre (panel 2), half of the members lie within $\sim 600\,\mathrm{km\ s^{-1}}$ from the centre, and the velocity histogram in panel 1, this region is a galaxy group candidate. This fact is drawn from the luminosity function of this region, where there are only one galaxies brighter than $M^0_{BJ} = -20^m.5$. The mass of this massive group is $1.54 * 10^{15}\,\mathrm{M}_\odot$.

VG20: $(l, b) = (275.91°, 9.33°)$, $(\alpha, \delta) = (153.43°, -45.09°)$, $E(B-V) = 0.17$

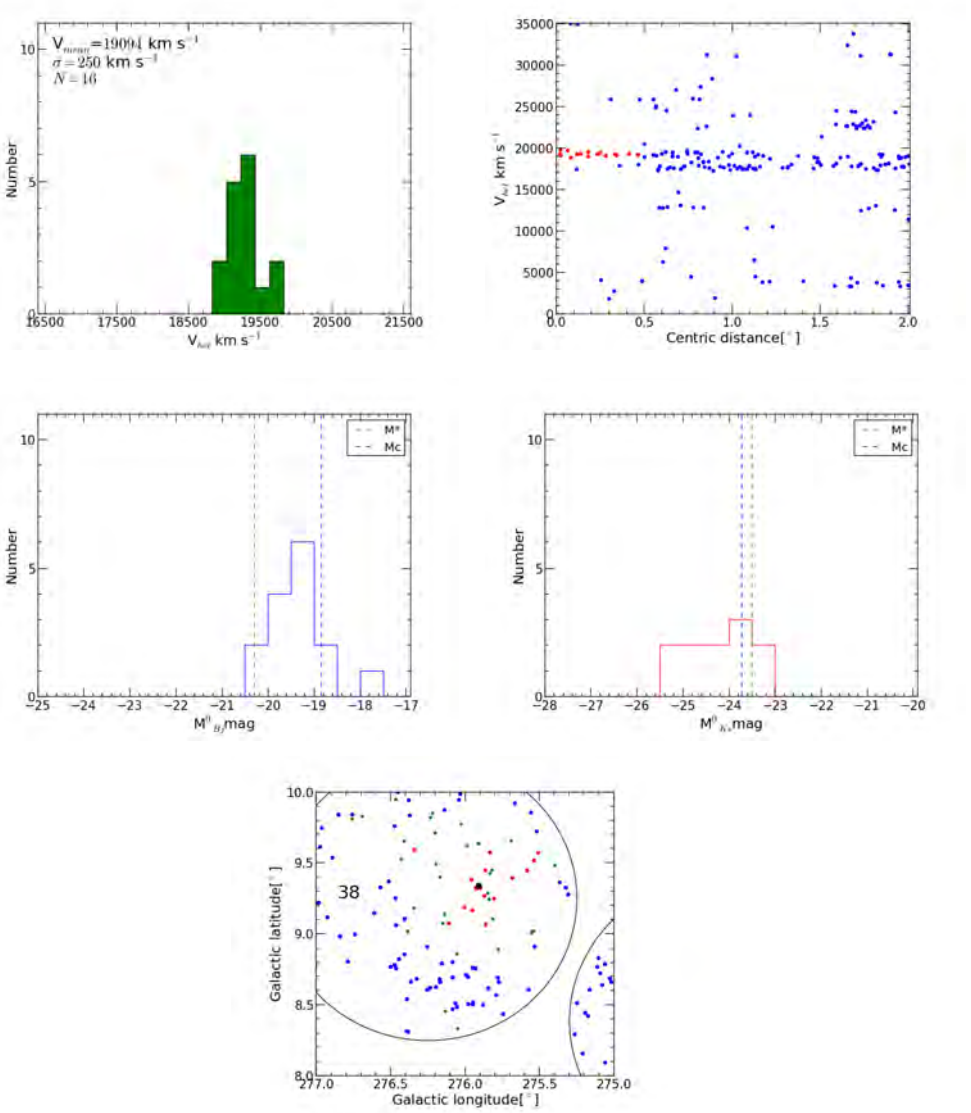

Figure C.33: From the luminosity function, panel 3 and 4, this region is a galaxy group candidate. Although it has high velocity histogram peak (panel 1), and a very dense centre, almost 90% of the objects lie within 600 km s^{-1} from the center (panel 2). This massive group has a mass of $1.45 * 10^{14}$ M$_\odot$.

VG21: $(l, b) = (281.27°, 6.86°)$, $(\alpha, \delta) = (158.05°, -50.06°)$, $E(B-V) = 0.42$

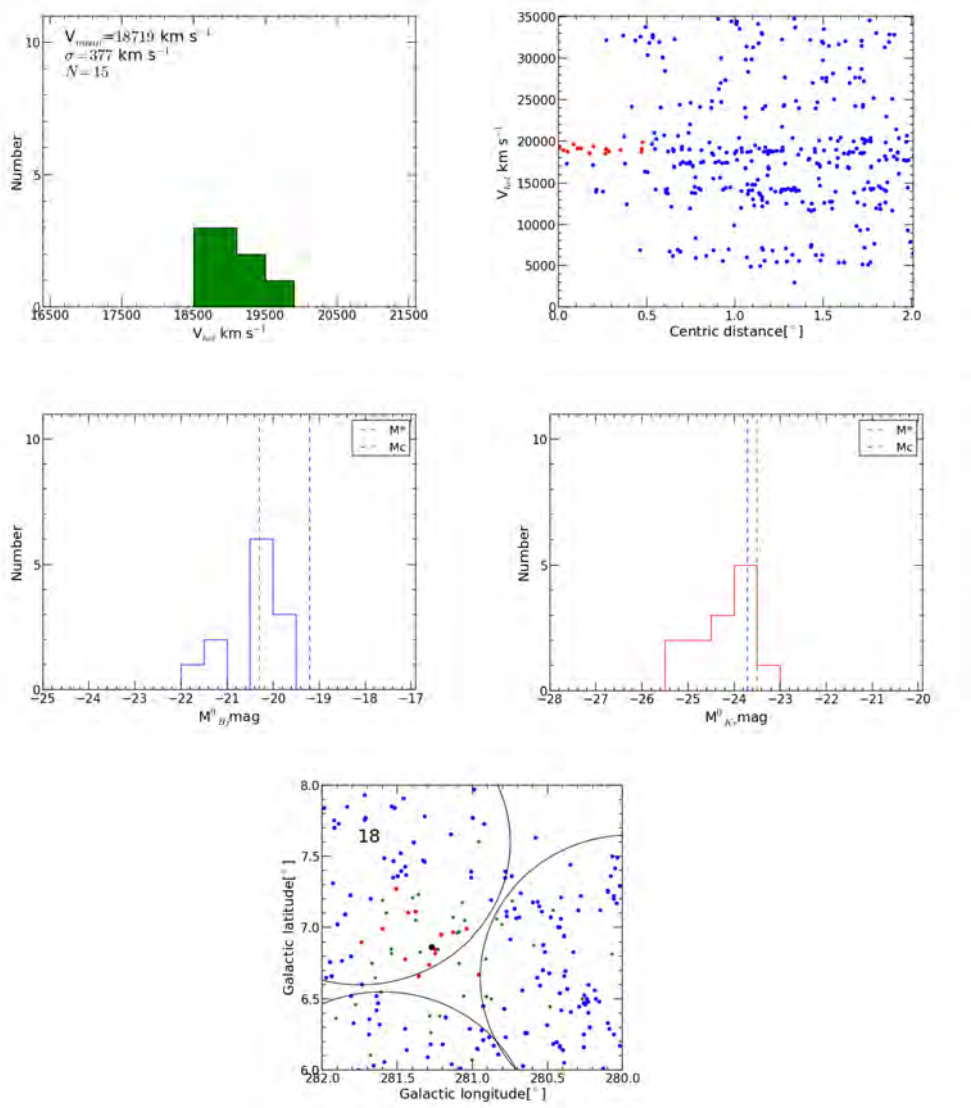

Figure C.34: From panel 1 this area has a velocity histogram that peaks around $\sim 19,000$ km s^{-1}. Panel 2 shows a very little concentration near the centre. From this and the luminosity function, panel 3 and 4, this region likely is a galaxy group. It has a mass of $3.3 * 10^{14}\,\mathrm{M}_{\odot}$.

VG22: $(l, b) = (291.65°, 8.36°)$, $(\alpha, \delta) = (174.16°, -52.86°)$, $E(B-V) = 0.21$

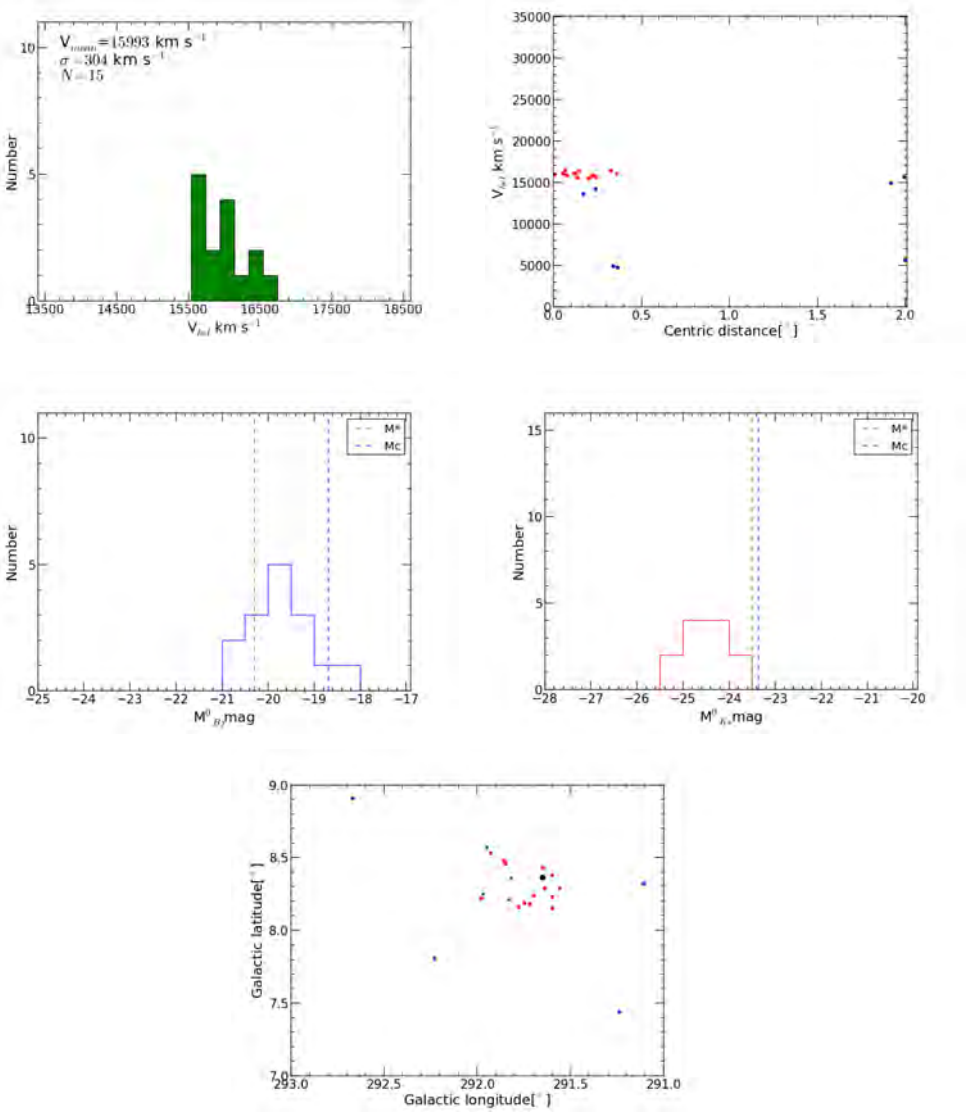

Figure C.35: Based on the multi-peaks around $\sim 16,000\,\mathrm{km\ s^{-1}}$ in panel 1, and the agglomeration of galaxies that appears from panel 2, this area likely is a group of galaxies with mass of $2.14 * 10^{14}\,\mathrm{M}_{\odot}$.

Appendix D

WISE Galaxy Search

In this appendix, I present the new targets prepared using WISE for follow-up spectroscopic observations in three galaxy clusters within the Vela Supercluster.
VC06: `http://www.ast.uct.ac.za/~ahmed/WiseVC06.tbl`
VC10: `http://www.ast.uct.ac.za/~ahmed/WiseVC10.tbl`
VC13: `http://www.ast.uct.ac.za/~ahmed/WiseVC13.tbl`

Bibliography

Aaronson, M., Bothun, G. D., Cornell, M. E., Dawe, J. A., Dickens, R. J., Hall, P. J., Sheng, H. M., Huchra, J. P., Lucey, J. R., Mould, J. R., Murray, J. D., Schommer, R. A., & Wright, A. E. 1989, Astrophysical Journal, 338, 654

Abell, G. O. 1958, Astrophysical Journal Supplement, 3, 211

Abell, G. O., Corwin, Jr., H. G., & Olowin, R. P. 1989, Astrophysical Journal Supplement Series, 70, 1

Araya-Melo, P. A., Reisenegger, A., Meza, A., van de Weygaert, R., Dünner, R., & Quintana, H. 2009, Monthly Notices of the Royal Astronomical Society, 399, 97

Baffa, C., Chincarini, G., Henry, R. B. C., & Manousoyanaki, J. 1993, Astronomy and Astrophysics, 280, 20

Bahcall, N. A. 1977a, Annual review of astronomy and astrophysics, 15, 505

—. 1977b, Annual review of astronomy and astrophysics, 15, 505

—. 1977c, Annual review of astronomy and astrophysics, 15, 505

Baldry, I. K., Alpaslan, M., Bauer, A. E., Bland-Hawthorn, J., Brough, S., Cluver, M. E., Croom, S. M., Davies, L. J. M., Driver, S. P., Gunawardhana, M. L. P., Holwerda, B. W., Hopkins, A. M., Kelvin, L. S., Liske, J., López-Sánchez, Á. R., Loveday, J., Norberg, P., Peacock, J., Robotham, A. S. G., & Taylor, E. N. 2014, Monthly Notices of the Royal Astronomical Society, 441, 2440

Batiste, M. & Batuski, D. J. 2013a, Monthly Notices of the Royal Astronomical Society, 436, 3331

—. 2013b, Monthly Notices of the Royal Astronomical Society, 436, 3331

Baum, W. A. 1962, in IAU Symposium, Vol. 15, Problems of Extra-Galactic Research, ed. G. C. McVittie, 390

Bilicki, M., Jarrett, T. H., Peacock, J. A., Cluver, M. E., & Steward, L. 2014, The Astrophysical Journal Supplement, 210, 9

Bondi, H. 1962, Cosmology

Branchini, E., Plionis, M., & Sciama, D. W. 1996, Astrophysical Journal Letters, 461, L17

Cameron, L. M. 1990, Astronomy and Astrophysics, 233, 16

Cardelli, J. A., Clayton, G. C., & Mathis, J. S. 1989, Astrophysical Journal, 345, 245

Cen, R. 1994, Astrophysical Journal, 424, 22

Charlier, C. V. L. 1922, Arkiv for Mat. Astron. Fys., 16, 1

Clutton-Brock, M. & Peebles, P. J. E. 1981, Astronomical Journal, 86, 1115

Colless, M., Dalton, G., Maddox, S., Sutherland, W., Norberg, P., Cole, S., Bland-Hawthorn, J., Bridges, T., Cannon, R., Collins, C., Couch, W., Cross, N., Deeley, K., De Propris, R., Driver, S. P., Efstathiou, G., Ellis, R. S., Frenk, C. S., Glazebrook, K., Jackson, C., Lahav, O., Lewis, I., Lumsden, S., Madgwick, D., Peacock, J. A., Peterson, B. A., Price, I., Seaborne, M., & Taylor, K. 2001a, Monthly Notices of the Royal Astronomical Society, 328, 1039

Colless, M. & Dunn, A. M. 1996, Astrophysical Journal, 458, 435

Colless, M., Saglia, R. P., Burstein, D., Davies, R. L., McMahan, R. K., & Wegner, G. 2001b, Monthly Notices of the Royal Astronomical Society, 321, 277

Collister, A. A. & Lahav, O. 2004, The Publications of the Astronomical Society of the Pacific, 116, 345

Courteau, S., Willick, J. A., Strauss, M. A., Schlegel, D., & Postman, M. 2000, Astrophysical Journal, 544, 636

da Costa, L. N., Bernardi, M., Alonso, M. V., Wegner, G., Willmer, C. N. A., Pellegrini, P. S., Rité, C., & Maia, M. A. G. 2000, The Astronomical Journal, 120, 95

Dale, D. A., Giovanelli, R., Haynes, M. P., Campusano, L. E., & Hardy, E. 1999, The Astronomical Journal, 118, 1489

de Filippis, E., Schindler, S., & Erben, T. 2005, Astronomy and Astrophysics, 444, 387

Doroshkevich, A., Tucker, D. L., Allam, S., & Way, M. J. 2004, Astronomy and Astrophysics, 418, 7

Dressler, A. 1984, Annual review of astronomy and astrophysics, 22, 185

Dreyer, J. L. E. 1888, Memoirs of the Royal Astronomical Society, 49, 1

Drinkwater, M. J., Proust, D., Parker, Q. A., Quintana, H., & Slezak, E. 1999, Publications of the Astronomical Society of Australia, 16, 113

Ebeling, H., Kocevski, D., Tully, R. B., & Mullis, C. R. 2005, in Astronomical Society of the Pacific Conference Series, Vol. 329, Nearby Large-Scale Structures and the Zone of Avoidance, ed. A. P. Fairall & P. A. Woudt, 83

Einasto, J., Joeveer, M., & Saar, E. 1980, Monthly Notices of the Royal Astronomical Society, 193, 353

Einasto, M., Einasto, J., Tago, E., Müller, V., & Andernach, H. 2001, The Astronomical Journal, 122, 2222

Einasto, M., Liivamägi, L. J., Tago, E., Saar, E., Tempel, E., Einasto, J., Martínez, V. J., & Heinämäki, P. 2011a, Astronomy Astrophysics, 532, A5

Einasto, M., Liivamägi, L. J., Tempel, E., Saar, E., Tago, E., Einasto, P., Enkvist, I., Einasto, J., Martínez, V. J., Heinämäki, P., & Nurmi, P. 2011b, The Astrophysical Journal, 736, 51

Faber, S. M., Burstein, D., Davies, R. L., Dressler, A., Lynden-Bell, D., Terlevich, R., & Wegner, G. 1988, in IAU Symposium, Vol. 130, Large Scale Structures of the Universe, ed. J. Audouze, M.-C. Pelletan, A. Szalay, Y. B. Zel'dovich, & P. J. E. Peebles, 169

Fairall, A. P. & Kraan-Korteweg, R. C. 2000, in Astronomical Society of the Pacific Conference Series, Vol. 218, Mapping the Hidden Universe: The Universe behind the Mily Way - The Universe in HI, ed. R. C. Kraan-Korteweg, P. A. Henning, & H. Andernach, 35

Feindt, U., Kerschhaggl, M., Kowalski, M., Aldering, G., Antilogus, P., Aragon, C., Bailey, S., Baltay, C., Bongard, S., Buton, C., Canto, A., Cellier-Holzem, F., Childress, M., Chotard, N., Copin, Y., Fakhouri, H. K., Gangler, E., Guy, J., Kim, A., Nugent, P., Nordin, J., Paech, K., Pain, R., Pecontal, E., Pereira, R., Perlmutter, S., Rabinowitz, D., Rigault, M., Runge, K., Saunders, C., Scalzo, R., Smadja, G., Tao, C., Thomas, R. C., Weaver, B. A., & Wu, C. 2013, Astronomy and Astrophysics, 560, A90

Feldman, H. A., Watkins, R., & Hudson, M. J. 2010, Monthly Notices of the Royal Astronomical Society, 407, 2328

Fernández-Soto, A., Lanzetta, K. M., Chen, H.-W., Pascarelle, S. M., & Yahata, N. 2001, The Astrophysical Journal Supplement Series, 135, 41

Firth, A. E., Lahav, O., & Somerville, R. S. 2003, Monthly Notice of the Royal Astronomical Society, 339, 1195

Fleenor, M. C., Rose, J. A., Christiansen, W. A., Hunstead, R. W., Johnston-Hollitt, M., Drinkwater, M. J., & Saunders, W. 2005, The Astronomical Journal, 130, 957

Fleenor, M. C., Rose, J. A., Christiansen, W. A., Johnston-Hollitt, M., Hunstead, R. W., Drinkwater, M. J., & Saunders, W. 2006, The Astronomical Journal, 131, 1280

Gardner, J. P., Sharples, R. M., Frenk, C. S., & Carrasco, B. E. 1997, The Astrophysical Journal, 480, L99

Giovanelli, R., Haynes, M. P., Salzer, J. J., Wegner, G., da Costa, L. N., & Freudling, W. 1998, The Astronomical Journal, 116, 2632

Giovanelli, R., Haynes, M. P., Wegner, G., da Costa, L. N., Freudling, W., & Salzer, J. J. 1996, Astrophysical Journal Letters, 464, L99

Haugbølle, T., Hannestad, S., Thomsen, B., Fynbo, J., Sollerman, J., & Jha, S. 2007, The Astrophysical Journal, 661, 650

Herschel, J. F. W. 1864, Royal Society of London Philosophical Transactions Series I, 154, 1

Hopkins, A. M., Driver, S. P., Brough, S., Owers, M. S., Bauer, A. E., Gunawardhana, M. L. P., Cluver, M. E., Colless, M., Foster, C., Lara-López, M. A., Roseboom, I., Sharp, R., Steele, O., Thomas, D., Baldry, I. K., Brown, M. J. I., Liske, J., Norberg, P., Robotham, A. S. G., Bamford, S., Bland-Hawthorn, J., Drinkwater, M. J., Loveday, J., Meyer, M., Peacock, J. A., Tuffs, R., Agius, N., Alpaslan, M., Andrae, E., Cameron, E., Cole, S., Ching, J. H. Y., Christodoulou, L., Conselice, C., Croom, S., Cross, N. J. G., De Propris, R., Delhaize, J., Dunne, L., Eales, S., Ellis, S., Frenk, C. S., Graham, A. W., Grootes, M. W., Häußler, B., Heymans, C., Hill, D., Hoyle, B., Hudson, M., Jarvis, M., Johansson, J., Jones, D. H., van Kampen, E., Kelvin, L., Kuijken, K., López-Sánchez, Á., Maddox, S., Madore, B., Maraston, C., McNaught-Roberts, T., Nichol, R. C., Oliver, S., Parkinson, H., Penny, S., Phillipps, S., Pimbblet, K. A., Ponman, T., Popescu, C. C., Prescott, M., Proctor, R., Sadler, E. M., Sansom, A. E., Seibert, M., Staveley-Smith, L., Sutherland, W., Taylor, E., Van Waerbeke, L., Vázquez-Mata, J. A., Warren, S., Wijesinghe, D. B., Wild, V., & Wilkins, S. 2013, Monthly Notices of the Royal Astronomical Society, 430, 2047

Hubble, E. 1929, Proceedings of the National Academy of Science, 15, 168

Huchra, J. P., Macri, L. M., Masters, K. L., Jarrett, T. H., Berlind, P., Calkins, M., Crook, A. C., Cutri, R., Erdoğdu, P., Falco, E., George, T., Hutcheson, C. M., Lahav, O., Mader, J., Mink, J. D., Martimbeau, N., Schneider, S., Skrutskie, M., Tokarz, S., & Westover, M. 2012, The Astrophysical Journal Supplement, 199, 26

Hudson, M. J. 1999, The Publications of the Astronomical Society of the Pacific, 111, 57

Hudson, M. J., Lucey, J. R., Smith, R. J., & Steel, J. 1997, Monthly Notices of the Royal Astronomical Societ, 291, 488

Hudson, M. J. & Lynden-Bell, D. 1991, Monthly Notices of the Royal Astronomical Society, 252, 219

Hudson, M. J., Smith, R. J., Lucey, J. R., & Branchini, E. 2004, Monthly Notices of the Royal Astronomical Society, 352, 61

Hudson, M. J., Smith, R. J., Lucey, J. R., Schlegel, D. J., & Davies, R. L. 1999, The Astrophysical Journal, 512, L79

Jarrett, T. H., Chester, T., Cutri, R., Schneider, S., Skrutskie, M., & Huchra, J. P. 2000a, The Astronomical Journal, 119, 2498

—. 2000b, The Astronomical Journal, 119, 2498

Jones, D. H., Read, M. A., Saunders, W., Colless, M., Jarrett, T., Parker, Q. A., Fairall, A. P., Mauch, T., Sadler, E. M., Watson, F. G., Burton, D., Campbell, L. A., Cass, P., Croom, S. M., Dawe, J., Fiegert, K., Frankcombe, L., Hartley, M., Huchra, J., James, D., Kirby, E., Lahav, O., Lucey, J., Mamon, G. A., Moore, L., Peterson, B. A., Prior, S., Proust, D., Russell, K., Safouris, V., Wakamatsu, K.-I., Westra, E., & Williams, M. 2009, Monthly Notices of the Royal Astronomical Society, 399, 683

Kocevski, D. D. & Ebeling, H. 2006, Astrophysical Journal, 645, 1043

Kocevski, D. D., Ebeling, H., Mullis, C. R., & Tully, R. B. 2007, The Astrophysical Journal, 662, 224

Kogut, A., Lineweaver, C., Smoot, G. F., Bennett, C. L., Banday, A., Boggess, N. W., Cheng, E. S., de Amici, G., Fixsen, D. J., Hinshaw, G., Jackson, P. D., Janssen, M., Keegstra, P., Loewenstein, K., Lubin, P., Mather, J. C., Tenorio, L., Weiss, R., Wilkinson, D. T., & Wright, E. L. 1993, Astrophysical Journal, 419, 1

Kraan-Korteweg, R. C. 2000a, Astronomy and Astrophysics Supplement, 141, 123

Kraan-Korteweg, R. C. 2000b, in Astronomical Society of the Pacific Conference Series, Vol. 218, Mapping the Hidden Universe: The Universe behind the Mily Way - The Universe in HI, ed. R. C. Kraan-Korteweg, P. A. Henning, & H. Andernach, 19

Kraan-Korteweg, R. C. 2005, in Reviews in Modern Astronomy, Vol. 18, Reviews in Modern Astronomy, ed. S. Röser, 48–75

Kraan-Korteweg, R. C. & Jarrett, T. 2005, in Astronomical Society of the Pacific Conference Series, Vol. 329, Nearby Large-Scale Structures and the Zone of Avoidance, ed. A. P. Fairall & P. A. Woudt, 119

Kraan-Korteweg, R. C. & Lahav, O. 2000, The Astronomy and Astrophysics Review, 10, 211

Kraan-Korteweg, R. C., Woudt, P. A., Cayatte, V., Fairall, A. P., Balkowski, C., & Henning, P. A. 1996, Nature, 379, 519

Lauberts, A. 1982, ESO/Uppsala survey of the ESO(B) atlas

Lauer, T. R. & Postman, M. 1994a, Astrophysical Journal, 425, 418

—. 1994b, Astrophysical Journal, 425, 418

Lavaux, G., Afshordi, N., & Hudson, M. J. 2013, Monthly Notices of the Royal Astronomical Society, 430, 1617

Lewis, I. J., Cannon, R. D., Taylor, K., Glazebrook, K., Bailey, J. A., Baldry, I. K., Barton, J. R., Bridges, T. J., Dalton, G. B., Farrell, T. J., Gray, P. M., Lankshear, A., McCowage, C., Parry, I. R., Sharples, R. M., Shortridge, K., Smith, G. A., Stevenson, J., Straede, J. O., Waller, L. G., Whittard, J. D., Wilcox, J. K., & Willis, K. C. 2002, Monthly Notices of the Royal Astronomical Society, 333, 279

Lin, H., Kirshner, R. P., Shectman, S. A., Landy, S. D., Oemler, A., Tucker, D. L., & Schechter, P. L. 1996, Astrophysical Journal, 471, 617

Lin, Y.-T., Mohr, J. J., & Stanford, S. A. 2004, The Astrophysical Journal, 610, 745

Lucey, J. R., Dickens, R. J., Mitchell, R. J., & Dawe, J. A. 1983, Monthly Notices of the Royal Astronomical Society, 203, 545

Lynden-Bell, D., Faber, S. M., Burstein, D., Davies, R. L., Dressler, A., Terlevich, R. J., & Wegner, G. 1988, Astrophysical Journal, 326, 19

Ma, Y.-Z. & Scott, D. 2013, Monthly Notices of the Royal Astronomical Society, 428, 2017

Macaulay, E., Feldman, H. A., Ferreira, P. G., Jaffe, A. H., Agarwal, S., Hudson, M. J., & Watkins, R. 2012, Monthly Notices of the Royal Astronomical Society, 425, 1709

Massarotti, M., Iovino, A., Buzzoni, A., & Valls-Gabaud, D. 2001, Astronomy and Astrophysics, 380, 425

Mathewson, D. S., Ford, V. L., & Buchhorn, M. 1992, Astrophysical Journal Supplement Series, 81, 413

Melnick, J. & Moles, M. 1987, Revista Mexicana de Astronomia y Astrofisica, 14, 72

Merluzzi, P., Busarello, G., Haines, C. P., Mercurio, A., Okabe, N., Pimbblet, K. J., Dopita, M. A., Grado, A., Limatola, L., Bourdin, H., Mazzotta, P., Capaccioli, M., Napolitano, N. R., & Schipani, P. 2015, Monthly Notices of the Royal Astronomical Society, 446, 803

Miles, T. A., Raychaudhury, S., & Russell, P. A. 2006, Monthly Notices of the Royal Astronomical Society, 373, 1461

Mitsuishi, I., Gupta, A., Yamasaki, N. Y., Takei, Y., Ohashi, T., Sato, K., Galeazzi, M., Henry, J. P., & Kelley, R. L. 2012, in American Institute of Physics Conference Series, Vol. 1427, American Institute of Physics Conference Series, ed. R. Petre, K. Mitsuda, & L. Angelini, 344–345

Mould, J. R., Staveley-Smith, L., Schommer, R. A., Bothun, G. D., Hall, P. J., Han, M. S., Huchra, J. P., Roth, J., Walsh, W., & Wright, A. E. 1991, Astrophysical Journal, 383, 467

Muñoz, J. A. & Loeb, A. 2008, Monthly Notices of the Royal Astronomical Society, 391, 1341

Müller, K. R., Freudling, W., Watkins, R., & Wegner, G. 1998, The Astrophysical Journal, 507, L105

Nagashima, C., Nagayama, T., Nakajima, Y., Tamura, M., Sugitani, K., Nagata, T., Hirao, T., Nakaya, H., Yanagisawa, K., & Sato, S. 1999, in Star Formation 1999, ed. T. Nakamoto, 397–398

Nagayama, T., Woudt, P. A., Wakamatsu, K., Nishiyama, S., Nagashima, C., Kato, D., Nagata, T., Nakaya, H., Sugitani, K., Tamura, M., & Sato, S. 2006, Monthly Notices of the Royal Astronomical Society, 368, 534

Nilson, P. 1973, Uppsala general catalogue of galaxies

Nusser, A., Branchini, E., & Davis, M. 2011, Astrophysical Journal, 735, 77

Pearson, D. W., Batiste, M., & Batuski, D. J. 2014, Monthly Notices of the Royal Astronomical Society, 441, 1601

Peebles, P. J. E. 1993, Principles of Physical Cosmology

Pellegrini, P. S. & da Costa, L. N. 1990, Astrophysical Journal, 357, 408

Pimbblet, K. A., Edge, A. C., & Couch, W. J. 2005, Monthly Notices of the Royal Astronomical Society, 357, L45

Postman, M. & Lauer, T. R. 1995, Astrophysical Journal, 440, 28

Proctor, R. 1887, The Universe of Stars, Cambridge Astrophysics (London: Longman, Green and Co.)

Proust, D., Quintana, H., Carrasco, E. R., Reisenegger, A., Slezak, E., Muriel, H., Dünner, R., Sodré, Jr., L., Drinkwater, M. J., Parker, Q. A., & Ragone, C. J. 2006, Astronomy and Astrophysics, 447, 133

Quintana, H., Carrasco, E. R., & Reisenegger, A. 2000, The Astronomical Journal, 120, 511

Quintana, H., Melnick, J., Proust, D., & Infante, L. 1997, A A Supplement series, 125, 247

Quintana, H., Ramirez, A., Melnick, J., Raychaudhury, S., & Slezak, E. 1995, Astronomical Journal, 110, 463

Rathaus, B., Kovetz, E. D., & Itzhaki, N. 2013, Monthly Notices of the Royal Astronomical Society, 431, 3678

Riad, I. F. 2010, PhD thesis, Cape Town University

Riad, I. F., Kraan-Korteweg, R. C., & Woudt, P. A. 2010, Monthly Notices of the Royal Astronomical Society, 401, 924

Rubin, V. C., Thonnard, N., Ford, Jr., W. K., & Roberts, M. S. 1976, Astronomical Journal, 81, 719

Saunders, W., Bridges, T., Gillingham, P., Haynes, R., Smith, G. A., Whittard, J. D., Churilov, V., Lankshear, A., Croom, S., Jones, D., & Boshuizen, C. 2004, in Society of Photo-Optical Instrumentation Engineers (SPIE) Conference Series, Vol. 5492, Ground-based Instrumentation for Astronomy, ed. A. F. M. Moorwood & M. Iye, 389–400

Scaramella, R., Baiesi-Pillastrini, G., Chincarini, G., Vettolani, G., & Zamorani, G. 1989, Nature, 338, 562

Schechter, P. 1976, Astrophysical Journal, 203, 297

Schlafly, E. F. & Finkbeiner, D. P. 2011, The Astrophysical Journal, 737, 103

Schlegel, D. J., Finkbeiner, D. P., & Davis, M. 1998, The Astrophysical Journal, 500, 525

Scoccimarro, R., Feldman, H. A., Fry, J. N., & Frieman, J. A. 2001, Astrophysical Journal, 546, 652

Shane, C. & Wirtanen, C. 1967, Publ. Lick Obs. XXII, Pt. 1

Shapley, H. 1930, Harvard College Observatory Bulletin, 874, 9

—. 1961, Galaxies.

Sharp, R., Saunders, W., Smith, G., Churilov, V., Correll, D., Dawson, J., Farrel, T., Frost, G., Haynes, R., Heald, R., Lankshear, A., Mayfield, D., Waller, L., & Whittard, D. 2006, in Society of Photo-Optical Instrumentation Engineers (SPIE) Conference Series, Vol. 6269, Society of Photo-Optical Instrumentation Engineers (SPIE) Conference Series

Sheth, R. K. & Diaferio, A. 2011, Monthly Notices of the Royal Astronomical Society, 417, 2938

Skrutskie, M. F., Cutri, R. M., Stiening, R., Weinberg, M. D., Schneider, S., Carpenter, J. M., Beichman, C., Capps, R., Chester, T., Elias, J., Huchra, J., Liebert, J., Lonsdale, C., Monet, D. G., Price, S., Seitzer, P., Jarrett, T., Kirkpatrick, J. D., Gizis, J. E., Howard, E., Evans, T., Fowler, J., Fullmer, L., Hurt, R., Light, R., Kopan, E. L., Marsh, K. A., McCallon, H. L., Tam, R., Van Dyk, S., & Wheelock, S. 2006, The Astronomical Journal, 131, 1163

Smith, G. A., Saunders, W., Bridges, T., Churilov, V., Lankshear, A., Dawson, J., Correll, D., Waller, L., Haynes, R., & Frost, G. 2004, in Society of Photo-Optical Instrumentation Engineers (SPIE) Conference Series, Vol. 5492, Ground-based Instrumentation for Astronomy, ed. A. F. M. Moorwood & M. Iye, 410–420

Smith, S. 1936, Astrophysical Journal, 83, 23

Springob, C. M., Magoulas, C., Colless, M., Mould, J., Erdoğdu, P., Jones, D. H., Lucey, J. R., Campbell, L., & Fluke, C. J. 2014, Monthly Notices of the Royal Astronomical Society, 445, 2677

Springob, C. M., Masters, K. L., Haynes, M. P., Giovanelli, R., & Marinoni, C. 2007, The Astrophysical Journal Supplement Series, 172, 599

Strauss, M. A., Cen, R., Ostriker, J. P., Lauer, T. R., & Postman, M. 1995, Astrophysical Journal, 444, 507

Tonry, J. L., Dressler, A., Blakeslee, J. P., Ajhar, E. A., Fletcher, A. B., Luppino, G. A., Metzger, M. R., & Moore, C. B. 2001, The Astrophysical Journal, 546, 681

Tonry, J. L., Schmidt, B. P., Barris, B., Candia, P., Challis, P., Clocchiatti, A., Coil, A. L., Filippenko, A. V., Garnavich, P., Hogan, C., Holland, S. T., Jha, S., Kirshner, R. P., Krisciunas, K., Leibundgut, B., Li, W., Matheson, T., Phillips, M. M., Riess, A. G., Schommer, R., Smith, R. C., Sollerman, J., Spyromilio, J., Stubbs, C. W., & Suntzeff, N. B. 2003, The Astrophysical Journal, 594, 1

Trumpler, R. J. 1930, Publications of the Astronomical Society of the Pacific, 42, 214

Tully, R. B. 2015, The Astronomical Journal, 149, 171

Tully, R. B., Courtois, H., Hoffman, Y., & Pomarède, D. 2014, Nature, 513, 71

Turnbull, S. J., Hudson, M. J., Feldman, H. A., Hicken, M., Kirshner, R. P., & Watkins, R. 2012, Monthly Notices of the Royal Astronomical Society, 420, 447

Verde, L., Heavens, A. F., Percival, W. J., Matarrese, S., Baugh, C. M., Bland-Hawthorn, J., Bridges, T., Cannon, R., Cole, S., Colless, M., Collins, C., Couch, W., Dalton, G., De Propris, R., Driver, S. P., Efstathiou, G., Ellis, R. S., Frenk, C. S., Glazebrook, K., Jackson, C., Lahav, O., Lewis, I., Lumsden, S., Maddox, S., Madgwick, D., Norberg, P., Peacock, J. A., Peterson, B. A., Sutherland, W., & Taylor, K. 2002, Monthly Notices of the Royal Astronomical Society, 335, 432

Vittorio, N., Juszkiewicz, R., & Davis, M. 1986, Nature, 323, 132

von Maltitz, K. 2012, Master's thesis, Cape Town University

Vorontsov-Vel'Yaminov, B. A. & Arkhipova, V. P. 1963, in Morphological catalogue of galaxies., 3 (1963), 0

Wakamatsu, K., Colless, M., Jarrett, T., Parker, Q., Saunders, W., & Watson, F. 2003, in Astronomical Society of the Pacific Conference Series, Vol. 289, The Proceedings of the IAU 8th Asian-Pacific Regional Meeting, Volume 1, ed. S. Ikeuchi, J. Hearnshaw, & T. Hanawa, 97–104

Watkins, R. & Feldman, H. A. 2015, Monthly Notices of the Royal Astronomical Society, 447, 132

Watkins, R., Feldman, H. A., & Hudson, M. J. 2009, Monthly Notices of the Royal Astronomical Society, 392, 743

Watson, F. G., Bogatu, G., Saunders, W., Farrell, T. J., Russell, K. S., Hungley, B. E., Miziarski, S., Gillingham, P. R., Parker, Q. A., & Colless, M. M. 2001, in Astronomical Society of the Pacific Conference Series, Vol. 232, The New Era of Wide Field Astronomy, ed. R. Clowes, A. Adamson, & G. Bromage, 421

Willick, J. A. 1999, The Astrophysical Journal, 522, 647

Willmer, C. N. A., da Costa, L. N., Pellegrini, P. S., Fairall, A. P., Latham, D. W., & Freudling, W. 1995, The Astronomical Journal, 109, 61

Woudt, P. A., Fairall, A., Kraan-Korteweg, R. C., Lucey, J., Schröder, A., Burstein, D., & McCall, M. L. 2005, in Astronomical Society of the Pacific Conference Series, Vol. 329, Nearby Large-Scale Structures and the Zone of Avoidance, ed. A. P. Fairall & P. A. Woudt, 147

Woudt, P. A. & Kraan-Korteweg, R. C. 2000, in Astronomical Society of the Pacific Conference Series, Vol. 218, Mapping the Hidden Universe: The Universe behind the Mily Way - The Universe in HI, ed. R. C. Kraan-Korteweg, P. A. Henning, & H. Andernach, 193

Woudt, P. A., Kraan-Korteweg, R. C., & Fairall, A. P. 2000, in Astronomical Society of the Pacific Conference Series, Vol. 201, Cosmic Flows Workshop, ed. S. Courteau & J. Willick, 88

Woudt, P. A., Kraan-Korteweg, R. C., Lucey, J., Fairall, A. P., & Moore, S. A. W. 2008, Monthly Notices of the Royal Astronomical Society, 383, 445

Wright, E. L., Eisenhardt, P. R. M., Mainzer, A. K., Ressler, M. E., Cutri, R. M., Jarrett, T., Kirkpatrick, J. D., Padgett, D., McMillan, R. S., Skrutskie, M., Stanford, S. A., Cohen, M., Walker, R. G., Mather, J. C., Leisawitz, D., Gautier, III, T. N., McLean, I., Benford, D., Lonsdale, C. J., Blain, A., Mendez, B., Irace, W. R., Duval, V., Liu, F., Royer, D., Heinrichsen, I., Howard, J., Shannon, M., Kendall, M., Walsh, A. L., Larsen, M., Cardon, J. G., Schick, S., Schwalm, M., Abid, M., Fabinsky, B., Naes, L., & Tsai, C.-W. 2010, The Astronomical Journal, 140, 1868

Zepf, S. E., de Carvalho, R. R., & Ribeiro, A. L. B. 1997, The Astrophysical Journal, 488, L11

Zucca, E., Zamorani, G., Scaramella, R., & Vettolani, G. 1993, Astrophysical Journal, 407, 470

Zwicky, F. 1957, Morphological astronomy